The Unquantified Mass Loss and Changes of Northern Hemisphere Marine-terminating Glaciers

William Kochtitzky

A thesis submitted in partial fulfillment of the requirements for the
Doctorate in Philosophy degree in Geography

Department of Geography, Environment, and Geomatics
Faculty of Arts
University of Ottawa

© William Kochtitzky, Ottawa, Canada, 2022

Abstract

Most of the glacier-caused sea level rise to date has been sourced from melt and icebergs from marine-terminating glaciers. Marine-terminating glaciers drain nearly all the Greenland and Antarctic ice sheets and many polar ice caps, ice fields, and mountain glaciers. However, we previously did not know how much solid mass, or frontal ablation, was lost by these glaciers, a key component of glacier mass balance. This thesis quantifies the area change and mass loss of marine-terminating glaciers in the Northern Hemisphere from 2000 to 2020 by quantifying glacier retreat, advance, and frontal ablation.

In total, the 1704 marine-terminating glaciers in the Northern Hemisphere lost an average of 389.7 ± 1.6 km^2 a^{-1} of their terminus from 2000 to 2020, for a total of 7527 ± 31 km^2, with 123 glaciers ceasing to be marine-terminating over this period. Overall, 85.3% of glaciers retreated, 2.5% advanced, and the remaining 12.3% did not change outside of uncertainty limits.

Frontal ablation of marine-terminating glaciers, not including the Greenland Ice Sheet, contributed an average of 44.47 ± 6.23 Gt a^{-1} of ice to the ocean from 2000 to 2010, and 51.98 ± 4.62 Gt a^{-1} from 2010 to 2020. Ice discharge from 2000 to 2020 was equivalent to 2.10 ± 0.22 mm of sea-level rise and comprised approximately 79% of frontal ablation, with the remainder from terminus retreat.

In Greenland, frontal ablation totaled 522.00 ± 17.38 Gt a^{-1} for 2000-2010 and 559.05 ± 12.59 Gt a^{-1} for 2010-2020. Ice discharge comprised ~90% of frontal ablation during both periods, while volume loss due to terminus retreat comprised the remainder. In total, Greenland accounted for 90% of northern hemisphere frontal ablation from 2000 to 2020. When combined with climatic-basal mass balance estimates this allows for the first estimate of complete Northern Hemisphere glacier mass budgets, which shows that Arctic Russia, Greenland, and Svalbard

have positive climatic-basal balances. For the first time, this thesis provides complete frontal ablation estimates for the entire Northern Hemisphere of 522.0 ± 17.4 Gt a^{-1} for 2000-2010 and 559.1 ± 12.6 Gt a^{-1} for 2010-2020.

Acknowledgements

This thesis would not have been possible without the support of many people and organizations. I am immensely grateful to Dr. Luke Copland for being the best supervisor one can imagine. When I think of all the best attributes of an advisor and mentor, Luke checks every single box. I am extremely grateful for his unwavering support in all my course work, research, and travels since I met him in 2017. Because of Luke I have received many amazing opportunities, got to travel to some of the most amazing places on this planet, and developed as a scientist. Luke continues to push me to be the best scientist possible, and I look forward to all our future collaborations.

I appreciate all the support I have received from various institutions and government agencies during my time in graduate school. The graduate research fellowship from the National Science Foundation allowed me to attend the University of Maine, without which I never would have met Luke Copland and all my now colleagues. The Vanier Graduate Scholarship from the Natural Sciences and Engineering Research Council of Canada (NSERC) funded my time in Ottawa and gave me the freedom to pursue my PhD research topic. Additional support came from research grants to Dr. Copland from ArcticNet Network of Centres of Excellence Canada, NSERC, Canada Foundation for Innovation, Ontario Research Fund, University of Ottawa and others. I thank the University of Ottawa for providing me with Excellence and International Doctoral Scholarships, which paid for tuition and fees over the last three years. I appreciate additional support from the International Arctic Science Committee, Phi Kappa Phi, and the Canadian Geophysical Union.

My research would not have been possible without a long list of collaborators on the projects that comprise this thesis: Dr. Wesley Van Wychen, Dr. Romain Hugonnet, Dr. Regine

Hock, Dr. Julian A. Dowdeswell, Toby Benham, Dr. Tazio Strozzi, Dr. Andrey Glazovsky, Dr. Ivan Lavrentiev, Dr. David Rounce, Dr. Romain Millan, Dr. Alison Cook, Abigail Dalton, Dr. Hester Jiskoot, Jade Cooley, Dr. Jacek Jania, Dr. Francisco Navarro, Dr. Michalea King, Dr. Mathieu Morlighem, Dr. Shfaqat Abbas Khan, and Dr. Brice Noël. I deeply appreciate all the conversations I had with each co-author that informed the work and my development as a glaciologist, especially Dr. Wesley Van Wychen, Dr. Romain Hugonnet, Dr. Regine Hock, and Dr. Hester Jiskoot. Finally, I thank the advice and participation of my committee members Dr. Anders Knudby, Dr. Michael Sawada, and Dr. Laurence Gray and external examiner Dr. Leigh Stearns.

While we ended up spending more time on Zoom than we would have ever thought, I am deeply appreciative to all the members of the Laboratory for Cryospheric Research who shaped my time in Ottawa both physically and virtually. To Brittany Main, Abigail Dalton, Claire Bernard-Grand'Maison, Dorota Medrzycka, Moya Painter, Braden Smeda, Adam Garbo, Benoit Lauzon, Gabriel Partington, Elodie Bracquart, Alison Cook, and Andrew Hamilton, thank you for being excellent lab mates, listening to me, bouncing ideas around, and collaborating. I learned a ton from you all and I look forward to our future work together.

I could not have done any of this without the amazing support of friends and family, especially given that I worked on this thesis during pandemic restrictions. Thank you to Dan and Betty Churchill who have supported me in research endeavors over the last decade at Dickinson and UMaine and have since become amazing friends. I am so appreciative of the McGinn family: Pete, Jeannette, Morris, Daniel, and Lydia and all the support they have given me over the years, especially our ski and hiking trips that motivated me. To my own parents, Rod Kochtitzky and Jane Hardy, thank you for your never ending supporting and amazing education that you gave

me. After lower school, I doubt many of my teachers would have thought I would be where I am today, thank you for supporting me on this journey. I also owe an immense amount of my mental health to dogs that have comforted and encourage me during my PhD and told me to stop working to go for a hike, ski, or walk. Thank you to Milo for paving the way and introducing us to the lagotto and accepting Sparrow even when you did not want to. Thank you to my dog, Sparrow, who always makes me smile and is the best office mate I could image. Without Sparrow, and the ideas generated on all those walks, this thesis would not be complete. Thank you, Leo, for your energy and desire to play. Finally, none of this would have been possible without the support of my partner Anna. Anna, thank you for your love, encouragement, and ideas. There is no better support system than you and Sparrow, thank you.

Preface

This thesis is written as a series of articles in collaboration with numerous co-authors under the supervision of Dr. Luke Copland. The three modified manuscripts, of which I am the primary author, are presented in chapters 2, 3, and 4 with an Introduction (chapter 1) and Conclusion (chapter 5). All references are presented together at the end (chapter 6), and tables and figures are presented at the end of each respective chapter.

In chapter 2 (Retreat of Northern Hemisphere marine-terminating glaciers, 2000-2020), I was responsible for the data processing, methodology, and manuscript development with support and suggestions provided by Luke Copland. This chapter benefited from one anonymous reviewer, reviewer James Lea, and editor Mathieu Morlighem.

In chapter 3 (Frontal ablation: the unquantified mass loss of marine-terminating glaciers, 2000-2020) I worked with a large team to complete the study. I did most of the data collection, performed the analyses and calculations, developed the methodology, and wrote the initial manuscript draft. Luke Copland aided in data collection and helped write the initial manuscript. Wesley van Wychen, Julian Dowdeswell, Alison Cook, Abigail Dalton, Hester Jiskoot, Jacek Jania, and Francisco Navarro helped with initial project planning and contributed to the final manuscript. Regine Hock contributed substantially to writing the final manuscript draft. Julian Dowdeswell, Toby Benham, Andrey Glazovsky, and Ivan Lavrentiev provided ice thickness data for the Russian Arctic. Hester Jiskoot and Jade Cooley provided frontal ablation estimates for Jan Mayen. David Rounce provided melt model results. Romain Millan provided glacier thickness data. Myself, Regine Hock, and Romain Hugonnet developed the error analysis and Romain Hugonnet completed it. This chapter benefited from anonymous reviewer comments.

In chapter 4 (Closing Greenland's mass balance: frontal ablation for every Greenlandic glacier from 2000 to 2020) I collaborated with numerous people to complete the study. I was primarily responsible for the data collection, methodology development, and initial manuscript writing with support and help from Luke Copland. Michalea King helped with comparisons to previous discharge estimates. Romain Hugonnet completed most of the error analysis. Hester Jiskoot helped with the initial idea for the manuscript and contributed to the final writing. Mathieu Morlighem and Romain Millan provided model thickness data for all glaciers. Shfaqat Abbas Khan provided geodetic mass balance observations necessary for adjusting the fluxgate height and Brice Noël provided surface mass balance model estimates. All authors helped with the final version of the manuscript.

Chapters 2, 3, and 4 are written in different styles, to meet requirements for specific journals. Chapter 2 is written in a more traditional style, consistent with the Geophysical Research Letters guidelines. Chapter 3 is written for publication in Nature Communications, with the methods at the end. Chapter 4 is written for Science Advances with a limited word count, methods at the end, and few figures and tables. At the time of writing (August 2022), chapter 2 has been published, chapter 3 is accepted, and chapter 4 is submitted for publication.

Citations for the articles, modified for this thesis, are as follows:

Chapter 2: Kochtitzky, W., Copland, L. 2022. Retreat of Northern Hemisphere marine-terminating glaciers, 2000-2020. Geophysical Research Letters, 48(3). doi.org/10.1029/2021GL096501

Chapter 3: Kochtitzky, W., Copland, L., Van Wychen, W., Hugonnet, R., Hock, R., Dowdeswell, J., Benham, T., Strozzi, T., Glazovsky, A., Lavrentiev, I., Rounce, D., Millan, R., Cook, A., Dalton, A., Jiskoot, H., Cooley, J., Jania, J., Navarro, F. Frontal ablation: the

unquantified mass loss of marine-terminating glaciers, 2000-2020. Nature Communications [Accepted].

Chapter 4: Kochtitzky, W., Copland, L., King, M., Hugonnet, R., Jiskoot, H., Morlighem, M., Millan, R., Khan, S., Noël, B. Closing Greenland's mass balance: frontal ablation for every Greenlandic glacier from 2000 to 2020. [Submitted to Nature Communications Earth and Environment]

Data availability

Datasets for this thesis are available with each publication and at the Polar Data Catalogue, University of Waterloo. The data associated with chapter 2 (Retreat of Northern Hemisphere marine-terminating glaciers, 2000-2020) is available for download from the Polar Data Catalogue at: https://polardata.ca/pdcsearch/PDCSearch.jsp?doi_id=13257. Datasets for chapters 3 and 4 will be available with the associated publication and/or the Polar Data Catalogue.

Table of contents

Abstract ii
Acknowledgements iv
Preface vii
Data availability ix
Table of contents x
List of Figures xiv
Chapter 1: Introduction 1
1.1 Introduction and Background 1
1.1.1 Sea level rise and Arctic climate change 1
1.1.2 Marine-terminating glaciers 2
1.1.3 Unique types of marine-terminating glaciers 4
1.1.4 Mass balance of marine-terminating glaciers 5
1.2 Purpose and objectives 8
Chapter 2: Retreat of Northern Hemisphere marine-terminating glaciers, 2000-2020 9
2.1 Introduction 9
2.2 Methods 10
2.2.1 Glaciers included in this study 10
2.2.2 Glacier terminus area change 11
2.2.3 Climate and ocean data 13
2.3 Results 13
2.3.1. Hemispheric patterns of marine-terminating glacier change 13
2.3.2 Greenland Ice Sheet change 14
2.3.3 GIC change 15
2.4 Discussion 16
2.4.1 Ice shelf and ice tongue collapse 18
2.4.2 Surging 19
2.4.3 Unstable basal geometry 20
2.4.4 Unusually wide calving margins 21
2.5 Conclusions 22
Chapter 3: Frontal ablation: the unquantified mass loss of Northern Hemisphere marine-terminating glaciers, 2000-2020 33
3.1 Introduction 33
3.2 Complete hemispheric estimates of discharge and terminus change 35

3.3 Uneven distribution of frontal ablation across all regions 36
3.4 Role of ice discharge versus terminus retreat 38
3.5 Conclusions and comparisons with regional mass balance 39
3.6 Methods 41
3.6.1 Marine-terminating glacier inventory 41
3.6.2 Flux gates 41
3.6.3 Frontal ablation estimation 42
3.6.4 Ice surface velocity 43
3.6.5 Ice thickness 44
3.6.6 Glacier terminus front positions 46
3.6.7 Climatic mass balance below the flux gate 47
3.6.8 Surge-type glaciers and instabilities 48
3.6.9 Sea-level rise calculations 49
3.6.10 Uncertainty in frontal ablation estimates 49
3.6.11 Uncertainty sources at flux gate point or glacier-scale 50
3.6.12 Spatial correlations in ice thickness and velocity uncertainties 51
3.6.13 Uncertainty propagation from pixel to glacier and regional scales 52
Chapter 4: Closing Greenland's mass balance: frontal ablation for every Greenlandic glacier from 2000 to 2020 65
4.1 Introduction 65
4.2 Results 67
4.3 Discussion 69
4.3.1 Comparison with previous estimates of Greenland ice discharge 69
4.3.2 Correction due to subaerial melting 69
4.3.3 Closing Greenland's mass budget 70
4.3.4 Northern Hemisphere frontal ablation 71
4.4 Conclusion 71
4.5 Materials and Methods 72
4.5.1 Estimating frontal ablation 72
4.5.2 Identification of marine-terminating glaciers. 73
4.5.3 Ice discharge 73
4.5.4 Terminus volume change 74
4.5.5 Surface mass balance and other adjustments 75
4.5.6 Error analysis 76
Chapter 5: Conclusion 80
5.1 Summary 80
5.2 Key contributions 83
5.3 Future work 84

Chapter 6: References 88

List of Tables

Table 2.1. Number and change in area of marine-terminating glaciers across the Northern Hemisphere between 2000, 2010 and 2020, by region. See figure 2.1 for location of regions……..……..24
Table 2.2 Number of marine-terminating glaciers in the Northern Hemisphere to retreat, advance, and cease to be marine-terminating by time period…….25
Table 2.3. The fastest retreating marine terminating glaciers in the Northern Hemisphere (sum is >50% of total area lost). The category column indicates which group the glacier belongs in: the Greenland Ice Sheet (GrIS) or glaciers and ice caps (GIC)……..26
Table 3.1. Frontal ablation and components. Decadal mean mass losses (± uncertainties) by region (from west to east) for all Northern Hemisphere marine-terminating glaciers, due to advance or retreat of terminus position (terminus mass change), ice flow through a terminus flux gate (ice discharge), and the sum of these (frontal ablation) ……..……. 54
Table 4.1. Frontal ablation for different regions in the northern hemisphere, and their components due to ice discharge and terminus mass change. Values for Greenland from this study; values for glaciers outside Greenland from Kochtitzky et al (In Review). All values show net mass loss……..……77

List of Figures

Figure 2.1 Distribution and change of marine-terminating glacier terminus area for 2000 to 2020. Circles are scaled (non-linearly) to the area loss of each major region in the Randolph Glacier Inventory. 30

Figure 2.2 Change in the terminus area of Northern Hemisphere marine-terminating glaciers from 2000 to 2020. Subregions are shown from west to east across the hemisphere. Retreats of > 6 km^2 a^{-1} are saturated as dark blue. Abbreviations: Arctic Canada North (ACN), Arctic Canada South (ACS), GR (Greenland), Svalbard (SV), Franz Josef Land (FJL), Novaya Zemlya (NZ), Severnaya Zemlya (SZ); all other abbreviations are cardinal directions. 31

Figure 2.3 Examples of glaciers with major changes from 2000 to 2020: a) Zachariae Isstrøm, loss after ice shelf collapse (base image: Landsat 8, 24 August 2019); b) Humboldt, loss due to unstable basal geometry (Landsat 8, 17 August 2020); c) Petermann, loss after ice tongue collapse (Landsat 8, 8 July 2020); d) Matusevich, loss after ice shelf collapse (Landsat 8, 26 August 2019); e) Location of glaciers shown in other subplots; f) Stonebreen, loss after surging (Landsat 8, 2 August 2019); g) Columbia, loss due to unstable basal geometry (Landsat 8, 8 August 2019); h) Kvitøyjøkulen, loss due to wide calving margin (Landsat 8, 5 August 2019); i) Vavilov Ice Cap, gain due to surging (Landsat 8, 26 August 2019). 32

Figure 3.1 Regional frontal ablation of marine-terminating glaciers. Bar charts show the decadal-mean frontal ablation rates by Northern Hemisphere region from 2000-2020 and are divided into ice discharge and terminus mass change (uncertainties are black lines). Pie charts show the proportion of marine vs. land terminating glaciers for each region. The Northern Hemisphere glacier proportions are shown in the legend……..55

Figure 3.2 Mean frontal ablation rate by glacier for 2010-2020. Dark gray triangles indicate glaciers that have a frontal ablation less than 0.02 Gt a^{-1} (not shown in color bar) and squares indicate glaciers where the uncertainty is more than 50% of total frontal ablation. Glacierized area is marked in white. Latitude and longitude in top left of each panel indicate the center point of that panel and the grid is 1° by 1° for all panels, with 1 degree of latitude equal to 111 km. The only glacier off the color bar scale is Basin-3 of Austfonna (6.18 Gt a^{-1}; Nordaustlandet). For uncertainties see Figure 3.5. Frontal ablation for 2000-2010 is shown in Figure 3.3. Abbreviations: ACN is Arctic Canada North, ACS is Arctic Canada South, GR is Greenland Periphery, SV is Svalbard, FJL is Franz Josef Land, NZ is Novaya Zemlya, SZ is Severnaya Zemlya; other abbreviations are cardinal directions. 56

Figure 3.3 Frontal ablation uncertainties by glacier for 2010-2020. Colored dots correspond to the uncertainty of the frontal ablation calculation from 0% (cool colors) to 100% (warm colors) of the total shown in Figure 3.2. Grey triangles indicate glaciers that have a frontal ablation of less than 0.02 Gt a^{-1}. Grid is 1° by 1° for all subplots and the coordinates in the top left of each subplot shows the center latitude and longitude of that subplot. Abbreviations: ACN is Arctic

Canada North, ACS is Arctic Canada South, GR is Greenland Periphery, SV is Svalbard, FJL is Franz Josef Land, NZ is Novaya Zemlya, SZ is Severnaya Zemlya; other abbreviations are cardinal directions. 57

Figure 3.4 Frontal ablation by glacier for 2000-2010. Dark gray triangles indicate glaciers that have a frontal ablation less than 0.02 Gt a^{-1} (not shown in color bar) and squares indicate glaciers where the uncertainty is more than 50% of total frontal ablation. Glacierized area is marked in white. Latitude and longitude in top left of each panel indicate the center point of that panel and the grid is 1° by 1° for all panels, with 1 degree of latitude equal to 111 km. The only glacier off the color bar scale is Hubbard Glacier (4.05 Gt a^{-1}; E Alaska). For uncertainties see Figure 3.5. Abbreviations: ACN is Arctic Canada North, ACS is Arctic Canada South, GR is Greenland Periphery, SV is Svalbard, FJL is Franz Josef Land, NZ is Novaya Zemlya, SZ is Severnaya Zemlya; other abbreviations are cardinal directions. 58

Figure 3.5 Frontal ablation uncertainties by glacier for 2000-2010. Colored dots correspond to the uncertainty of the frontal ablation calculation from 0% (cool colors) to 100% (warm colors) of the total shown in Figure 3.4. Grey triangles indicate glaciers that have a frontal ablation of less than 0.02 Gt a^{-1}. Grid is 1° by 1° for all subplots and the coordinates in the top left of each subplot shows the center latitude and longitude of that subplot. Abbreviations: ACN is Arctic Canada North, ACS is Arctic Canada South, GR is Greenland Periphery, SV is Svalbard, FJL is Franz Josef Land, NZ is Novaya Zemlya, SZ is Severnaya Zemlya; other abbreviations are cardinal directions. 59

Figure 3.6 Intensity index of frontal ablation in near-coastal ocean environments 2010-2020. The index is defined as the sum of the frontal ablation rates of all glaciers within 50 km of their terminus, based on a 10 km ocean grid. Text in white indicates values above 4.5 Gt a^{-1}. The pie charts show the proportion of ice discharge (blue) and terminus change (red) to total frontal ablation for each region, and are scaled to frontal ablation for that region. Glacier-covered area is shown in white, ocean in light blue, and other land surfaces in grey. Individual glaciers or ice caps mentioned in the text are named. The grid shows lines of latitude every 10° and longitude every 5°, or 1106 km between lines of latitude for all panels. The coordinates in the bottom left of each box show the center latitude and longitude. 60

Figure 3.7 Data sets used to compute frontal ablation exemplified for a glacier on Novaya Zemlya, Russia (75.2°N, 57.1°E). A) Glacier termini positions and glacier area lost by retreat or gained by advance (red hatching, ΔS_{term} in Equation 3.3) and area not involved in retreat/advance below the fluxgate (blue hatching, Sf in Equation 3.2) for 2000-2010. B) Same as Figure 3.7A except for 2010-2020. C) Glacier thickness distribution derived from model data generated by Millan et al. (2022). D) Surface velocity data for 2018 from ITS_LIVE (Gardner et al., 2019). Thickness (Hn) and velocity (Vn) data along the flux gate are used in Equation 3.2. Thickness data averaged over the most extended glacier terminus position during the considered period (H) is used in Equation 3.3. 61

Figure 3.8 Debiasing of modelled ice thickness estimates. Bias between modelled and measured ice thicknesses after adjustment of surface elevations to 2005 (for 2000-2010 period) or 2015 (for 2000-2020 period) to account for geodetic mass balance. The bias is empirically estimated by binning the difference of measurement and model estimates within 20 intervals (every 40 m) of modelled ice thickness. The sample count of each bin represents the number of flux gate points where measured and modelled ice thickness were compared. The bias dependency to modelled ice thickness is constrained by a linear function optimized by least-squares. The bias is later removed by subtracting the value of this function at each location..... 62

Figure 3.9 Spatial correlation of velocity estimates. Empirical and modelled variogram of velocity estimates, expressed as a percentage of the global velocity variance. The empirical variogram is estimated from the differences between ITS_LIVE and MEaSUREs velocities in Greenland compared at the same locations and for the same yearly periods. The sample count describes the number of pairwise flux gate comparisons used to estimate the variogram at each spatial lag (i.e. distance between observations). The modelled variogram is a sum of three spherical models optimized by least-squares. The first spherical model with range (correlation length) of 0.7 km has a partial sill (correlated variance) of 63% of the global velocity variance, the second model with range 18 km of 26% of the variance, and the third model with range 1,040 km of 11% of the variance. The spatial correlation of velocity is deduced by subtracting the modelled variogram to the global variance and used to propagate uncertainties from pixel to larger scales in ice discharge estimates..... 63

Figure 3.10 Spatial correlation of ice thickness estimates. Empirical and modelled variogram of ice thickness estimates, expressed as a percentage of the global ice thickness variance. The empirical variogram is estimated from the differences between measured and de-biased modelled ice thicknesses compared at the same locations and adjusted to the same year with elevation changes. The sample count describes the number of pairwise flux gate comparisons used to estimate the variogram at each spatial lag (i.e. distance between observations). The modelled variogram is a sum of three spherical models optimized by least-squares. The first spherical model with range (correlation length) of 2 km has a partial sill (correlated variance) of 27% of the global ice thickness variance, the second model with range 47 km of 50% of the variance, and the third model with range 1,404 km of 23% of the variance. The spatial correlation of ice thickness is deduced by subtracting the modelled variogram to the global variance, and used to propagate uncertainties from pixel to larger scales in both ice discharge and terminus mass change estimates. 64

Figure 4.1 Mean annual frontal ablation of Greenland for: a) 2000-2010, b) 2010-2020. Jakobshavn Isbrae is the only glacier with frontal ablation exceeding the blue/red color scale at 34.9 Gt a^{-1} for 2000-2010 and 41.1 Gt a^{-1} for 2010-2020. The graduated circles show the portions of frontal ablation due to terminus volume loss (blue) and ice discharge (red) in each region. Squares indicate glaciers with >50% uncertainty in their frontal ablation estimates and triangles indicate glaciers with <0.02 Gt a^{-1} of frontal ablation. The yellow/green/blue color scale shows

the frontal ablation intensity in the ocean for each period, defined as the sum of frontal ablation occurring within 80 km of a glacier terminus. Regions are delineated based on glacier basins from Mouginot and Rignot (2019). Labeled glaciers during each time period are the 10 largest frontal ablation rates in Greenland..... 78

Figure 4.2 Discharge as total percent of frontal ablation for: a) 2000-2010, b) 2010-2020. The remaining portion of frontal ablation is due to terminus volume loss (retreat). Larger dots represent more frontal ablation, and the map only shows glaciers with > 0.1 Gt a^{-1} of frontal ablation. The absolute values of frontal ablation are shown in Figure 4.1 for the same periods.. 79

Chapter 1: Introduction

1.1 Introduction and Background

1.1.1 Sea level rise and Arctic climate change

Sea level has already risen by ~22 cm since 1900 (IPCC, 2021), with devastating consequences for low lying communities around the world. Ocean levels have risen an average of 3.6 mm a^{-1} between 2006 and 2015 (IPCC SROCC, 2019), and are rising faster every year (Nerem et al., 2018). Sea level is predicted to further increase between 0.57-1.10 m by 2100 and 1.84-5.5 m by 2500, causing even more costly and deadly storm surges, flooding, and coastal erosion (Jevrejeva et al., 2012). The large uncertainty in this projection primarily rests in how glaciers respond to climate change, particularly the ice sheets. Marine-terminating glaciers, or those that end in the ocean, play a critical role in future sea level rise because they are the primary contributors to such changes. In Greenland, 87% of the glacierized area ends in the ocean. Outside of Greenland, 28% of glacier area ends in the ocean in the Northern Hemisphere. The future evolution of marine-terminating glaciers is one of the most critical variables in predicting future sea level rise.

The Arctic has experienced rapid change in recent years and is currently warming at an average of twice the rate of low latitude areas, with some regions warming by >4°C over the past ~30 years and contributing substantially to raising the global average temperature (Huang et al., 2017). These changes are having a dramatic impact on ice masses, with increasingly negative mass balance of glaciers and ice caps towards the present day (Zemp et al., 2019). In the past two decades, the rate of mass loss has increased by 48 ± 16 Gt a^{-1} outside the ice sheets, which is a 6-19% increase in contributions to sea level rise (Hugonnet et al., 2021). Arctic sea ice is also experiencing large declines due to this rapid warming (12.8 ± 2.3% per decade since 1979; IPCC

SROCC, 2019), particularly among multi-year sea ice (Maksym, 2019). This change is impacting the type and amount of precipitation that falls, with recent and projected increases in air moisture due to the increasingly ice-free areas of the Arctic Ocean (Bintanja & Andry, 2017), and increased poleward moisture transport (Zhang et al., 2013). This increase in humidity will drive more precipitation on land, but models suggest that this will increasingly come as rain, not snow (Bintanja, 2018; Bintanja & Andry, 2017). This has already been observed in the Arctic as Eureka weather station at 80°N on Ellesmere Island experienced a ~10% increase in precipitation between 1961 and 2007 (Lesins et al., 2010). Monitoring how glaciers are reacting to this change is crucial for predicting how they will evolve in the future.

1.1.2 Marine-terminating glaciers

Marine-terminating glaciers differ from land-terminating glaciers in that the terminus of the glacier is in contact with the ocean, which leads to several consequences. Land terminating glaciers slow towards their terminus and, within the same region, are typically smaller and have lower surface velocities than nearby glaciers (Van Wychen et al., 2016). In contrast, the surface velocity of marine-terminating glaciers is typically greatest at the terminus, where a calving face forms and icebergs are produced as the ocean provides little resistance to glacier flow (Meier & Post, 1987). Changes at the ice-ocean interface can propagate upglacier and alter upstream glacier dynamics (Meier & Post, 1987; Nick et al., 2009; Schoof, 2007). These changes can include retreat (O'Neel et al., 2005), loss of an ice shelf (Willis et al., 2015), or changes in ocean conditions (Wood et al., 2018). Because marine-terminating glaciers have an interface with the ocean, they are sensitive to changes in both atmospheric and oceanographic conditions (Cook et al., 2019). Warming surface and benthic ocean waters can enhance melt at the ice-ocean

interface and decrease stability, speeding up the glacier and increasing mass loss. For example, intrusion of warm Atlantic water into Greenland fjords has lead to retreat of 74 glaciers making up 49% of Greenland mass loss since the mid-1990s (Wood et al., 2021).

Marine-terminating glaciers can also play a critical role in supporting marine ecosystems and biogeochemical cycling (Hopwood et al., 2020). Subglacial drainage systems typically end at the ice-ocean interface where more buoyant, fresh water rises to the surface creating a plume (Meire et al., 2017). These plumes bring inorganic nutrients to the ocean surface that are otherwise limited in fjord environments and lead to phytoplankton blooms (Gerringa et al., 2012). Results from Greenland suggest that fjords with marine-terminating glaciers can sustain more productive fisheries due to the upwelling of nutrient rich bottom water compared to fjords with land terminating glaciers (Meire et al., 2017). Even iceberg meltwater can play a critical role in fjord freshwater budgets, circulation, and ecosystems (Moon et al., 2018). The presence of marine-terminating glaciers is thus important to coastal ecosystems and can help support a variety of organisms across the food web.

Marine-terminating glaciers (and associated ice shelves) are the only source of icebergs in the world, which can pose a significant navigational hazard (Bigg & Billings, 2014). Even small icebergs can pose navigational hazards by congesting waters and generating waves as they roll and break apart. Icebergs can extend to hundreds of meters depth and be tens of kilometers wide (Cuffey & Paterson, 2010), and can reach the ocean bottom where they can leave marks and disturb the sea bed (Scheick et al., 2019). Icebergs can drift thousands of kilometers and survive for several years, with some drifting from northern Greenland to Newfoundland (Crawford et al., 2018). While some datasets exist that currently approximate iceberg source areas in Greenland (King et al., 2018; Mankoff et al., 2020) and Arctic Canada (Van Wychen et

al., 2014) they are spatially incomplete. The only region in the Arctic today with complete iceberg volume estimates is Alaska (McNabb et al., 2015).

1.1.3 Unique types of marine-terminating glaciers

Some polar glaciers have ice shelves, which float in front of, but attached to, upstream glaciers and can provide additional stability at a glacier front. When an ice shelf collapses, glacier velocities frequently speed up behind the former ice shelf as resistive forces from the ice shelf are gone (Scambos et al., 2014). In the Arctic many ice shelves have been lost, including 90% of ice shelf area across northern Ellesmere Island during the twentieth century (Vincent et al., 2001). For example, in 2005, the Ayles Ice Shelf broke apart in under an hour, creating a 66.4 km^2 ice island (Copland et al., 2007). In 2012, Matusevich Ice Shelf, Russia, broke apart in less than one month, and within two years glaciers that used to feed the ice shelf tripled in velocity (Willis et al., 2015). The loss of ice shelves can thus be rapid, leading to large area losses in as little as hours, and altering upstream glacier dynamics

Ice caps are typically made up of multiple outlet glaciers that flow radially from the accumulation area (Cogley et al., 2011). Ice caps are common in polar environments and many ice cap outlets reach the ocean in the Arctic. For some very far northern ice caps in Arctic Russia, the entire ice cap is surrounded by ocean, such as in Franz Josef Land (Dowdeswell, 2017). The ice caps play an important role in draining large areas of ice to the ocean and can frequently have wide ice-ocean interfaces, increasing the sensitivity of those glaciers to oceanographic changes (Dowdeswell, 2017).

Surge-type glaciers alternate between short-lived active phases and long-lived quiescent phases (Meier & Post, 1969). These surge cycles can last decades to centuries, depending on the

surge mechanisms (Dowdeswell et al., 1991). Surges are typically characterized by velocity increases of an order of magnitude or more and can cause large advances of the glacier termini, while quiescent phases are marked by low velocities and terminus retreat (Meier & Post, 1969). Switching between these two phases can result in dramatic changes in glacier dynamics, terminus position, and iceberg production (Dunse et al., 2015). Large swaths of the Arctic are located in a band of climatic conditions favourable for surge-type glaciers, particularly in Arctic Canada, Russia, and Svalbard (Sevestre & Benn, 2015). One of the most significant Arctic surge events in recent decades occurred at Vavilov Ice Cap, Russia, where the main outlet of the ice cap advanced 8 km into the ocean and thinned by 0.3 m per day over the period 2010-2016, with ice velocities reaching over 6000 m a^{-1} (Willis et al., 2018). Surge events dramatically alter glacier dynamics and cause a variable glacier mass balance between surge phases.

1.1.4 Mass balance of marine-terminating glaciers

Cogley et al. (2011) describe the terms that make up the total mass balance of a glacier as the sum of either accumulation and ablation, or climatic-basal mass balance and frontal ablation. Because frontal ablation is a term included within ablation, this thesis will use the definition of total mass balance as the sum of climatic-basal mass balance and frontal ablation. These terms are defined as follows by Cogley et al. (2011):

(a) The climatic-basal mass balance includes: (i) the climatic mass balance, which incorporates the surface and internal balance, and (ii) the basal balance. The surface balance includes snowfall, refreezing on the glacier surface (e.g. melt water in crevasses), and surface melt. The internal balance consists of melt (e.g. due to strain heating) and refreezing (e.g. in firn) within the glacier. Basal mass balance then takes place at the

glacier-bedrock interface and consists of ablation (e.g. due to geothermal heat flux and/or heating due to sliding) and accumulation (e.g. due to refreezing).

(b) Frontal ablation includes calving of icebergs at the glacier terminus, subaerial frontal melting and sublimation, and subaqueous frontal melting, which are all the mass loss processes occurring at the calving face.

Thus, for land terminating glaciers the total mass balance is equal to the climatic-basal mass balance, while lake and marine-terminating glaciers have the additional frontal ablation term.

Different methods of quantifying glacier mass balance have been developed based on modeling and satellite remote sensing. While modeling efforts can make assumptions about each component of mass balance (e.g., melt vs. snow accumulation), and can better segregate mass loss than other methods, they still primarily rely on remote sensing observations (Huss & Hock, 2015). Geodetic and gravimetric methods are the two main techniques used to compute glacier mass balance from satellites. Geodetic mass balance estimates commonly use laser and radar altimeters (e.g., ICESat-2; CryoSat-2; Moholdt et al., 2010), and photogrammetry derived from stereo satellite images (e.g., ASTER; Hugonnet et al., 2021), to compute glacier height changes, which can be converted to volume and mass based on density assumptions. Gravimetric methods can directly measure the mass changes of glaciers and ice sheets based on small changes in gravitational attraction that can be detected by satellites flying in tandem (e.g., GRACE), but can only do so at coarse resolution (tens of km) and rely on models to account for processes such as isostatic rebound (Ciracì et al., 2020). However, both methods neglect glacier mass loss below sea level as geodetic methods only measure the height difference between the glacier and ocean surface, and gravimetric methods are not able to distinguish between ice and ocean water that is displaced or replaced. Thus, estimates of frontal ablation are needed for two main reasons: first,

to segregate and account for each term when computing mass balance and, second, to compute a complete glacier mass budget including the portion of mass lost below sea level.

To compute frontal ablation, one needs to quantify the mass loss due to ice discharge, and mass change due to terminus retreat or advance. Ice discharge is simpler to quantify because the only required inputs are a flux gate perpendicular to flow near the terminus, glacier thickness, and ice surface velocity. Thus, ice discharge has been quantified for many regions of the Arctic, including Arctic Canada (Van Wychen et al., 2014, 2016, 2021), Greenland (King et al., 2018; Mankoff et al., 2020), Alaska (McNabb et al., 2015), and Svalbard (Błaszczyk et al., 2009). Of these regions only studies from Alaska and Svalbard have included terminus change in their estimates to compute frontal ablation (McNabb et al., 2015; Błaszczyk et al., 2009), but these results have not been updated since at least 2013. Thus, we need a comprehensive and methodologically consistent quantification of frontal ablation for each glacier in the Northern Hemisphere so that a complete mass budget can be computed, and so that the relative importance of each mass balance term can be quantified.

The main reason as to why frontal ablation has not been previously computed on a hemispheric basis was lack of data to quantify the volume gained or lost by each glacier terminus due to advance or retreat. To quantify the volume, one first needs to know the area change of each terminus. These data have been collected for some regions, including Arctic Canada (Cook et al., 2019), Novaya Zemlya (Carr et al., 2014), and Greenland (McFadden et al., 2011; Moon & Joughin, 2008; Murray et al., 2015; King et al., 2020), but measurements have never been undertaken across all glaciers in the Northern Hemisphere using a consistent method during the same time period.

1.2 Purpose and objectives

The primary aim of this thesis is to quantify frontal ablation for all Northern Hemisphere glaciers for the first time. This thesis takes a census approach (i.e., measuring the full population) to document the area and mass balance of marine-terminating glaciers in the Northern Hemisphere from 2000 to 2010, and 2010 to 2020. The major questions this thesis addresses are:

1. How many marine-terminating glaciers are there in the Northern Hemisphere, and where are they located?
2. How have marine-terminating glacier termini in the Northern Hemisphere changed during the last two decades? What are the main factors driving those changes?
3. What is the contribution of frontal ablation of all glaciers and ice sheet outlets in the Northern Hemisphere to total glacier mass balance?

The results of this thesis advance our knowledge of marine-terminating glaciers by providing the first comprehensive study to map the position of all such glaciers in the Northern Hemisphere, and quantifying the area change and frontal ablation of each one. These observations will be critical to close glacier mass budgets, and inform future work on estimating global sea level rise and glacier mass balance.

Chapter 2: Retreat of Northern Hemisphere marine-terminating glaciers, 2000-2020

2.1 Introduction

Globally, average air temperatures for 2001-2020 are 0.99°C higher than they were in 1850-1900 (IPCC, 2021), with enhanced warming in the polar regions driven by polar amplification (Stuecker et al., 2018). Glaciers, ice caps, and ice sheets are increasingly losing mass, with mass loss rates for the Greenland Ice Sheet, for example, increasing from being approximately in balance in the 1990s, to 222 ± 30 Gt a^{-1} for 2013-2017 (Shepherd et al., 2020). To maintain equilibrium with their mass throughput, glaciers, both marine and land terminating, have exhibited terminus retreat (Zemp et al., 2015).

Marine-terminating glaciers, also known as tidewater glaciers, are defined as ice masses which contact the ocean along a grounded terminus, floating terminus, or ice shelf (Cogley et al., 2011). While all glaciers contribute to sea level rise through surface melt, marine-terminating glaciers also contribute via frontal ablation, or the calving of icebergs (Cogley et al., 2011). Quantification of their terminus position provides an essential climate variable (Bojinski et al., 2014) and important information to better understand glacier mass balance, natural hazards, ice-ocean interactions, and the impacts of climate change. Marine-terminating glacier retreat can lead to instabilities at the calving front that further increase glacier velocity and decrease glacier thickness (Meier & Post, 1987; Nick et al., 2009; Schoof, 2007). Changes in terminus position can be non-linear, although over decadal timescales there is evidence that regional retreat is linear (Fahrner et al., 2021). Terminus change is not fully considered in glacier mass balance measurements, as gravimetric (Ciracì et al., 2020) and geodetic (Hugonnet et al., 2021) methods are not able to quantify glacier mass loss below sea level. To first differentiate the mass losses

above and below sea level, we need to map the glacier area change that is also a change in ocean area.

There are several ways to measure the changes of marine-terminating glaciers. Most studies have focused on quantifying length changes, using either a box or centerline approach. This has identified the retreat of most, but not all, marine-terminating glaciers in Alaska from 1948 to 2012 (McNabb et al., 2015), the retreat of 94% of marine-terminating glaciers in the Canadian Arctic between 1958 and 2015 (Cook et al., 2019), and widespread losses in Greenland (McFadden et al., 2011; Moon & Joughin, 2008; Murray et al., 2015; King et al., 2020), Atlantic Arctic (Carr et al., 2017), and the Russian Arctic (Carr et al., 2014). The centerline or box methods rely on a line or multiple lines to calculate length change (Lea et al., 2014). The main problem with quantifying the retreat along a line is that most glaciers have complex terminus shapes, which are difficult to accurately capture with centerline measurements. Thus, the best way to assess glacier terminus change is to directly measure changes in terminus area. However, no study has identified all northern hemisphere marine-terminating glaciers and evaluated their terminus change over a consistent period with a consistent methodology. Here, we manually digitize the terminus region of every marine-terminating glacier in the Northern Hemisphere to quantify their change in terminus area in approximately 2000, 2010, and 2020, and investigate the patterns and causes of those changes.

2.2 Methods

2.2.1 Glaciers included in this study

We manually identified every glacier, regardless of size, in the Northern Hemisphere that contacted the ocean between 2000 and 2020 using Landsat 5, Landsat 7, Landsat 8, and ASTER

satellite imagery. We differentiate between: (a) the Greenland Ice Sheet, and (b) glaciers and ice caps (GICs), which include the peripheral glaciers of Greenland outside of the ice sheet. We used Randolph Glacier Inventory version 6 (RGI6; RGI Consortium, 2017) to help identify marine terminating GICs and to provide a unique identifier for each glacier. For the Greenland Ice Sheet we used outlines from Mouginot and Rignot (2019) for a unique identifier. We used Rastner et al.'s (2012) classification for glaciers that have a weak (CL1) or no (CL0) hydrological connection to the Greenland Ice Sheet to define periphery glaciers, while those with a strong (CL2) hydrological connection are defined as part of the ice sheet.

The number of glaciers reported here may differ from other studies due to the variable treatment of single glaciers that have multiple termini, or single termini that are fed by several tributaries. Various studies split or group such glaciers or termini in different ways, including RGI6, where, for example, low-lying ice caps with little or no outlet definition are inconsistently divided in the Russian Arctic. However, while different inventories may report different numbers of glaciers in a region, it will not impact regional area change totals.

2.2.2 Glacier terminus area change

We manually digitized polygons of the terminus region for every glacier in approximately 2000, 2010, and 2020, primarily based on summer (July and August), cloud-free, true-color Landsat 5, 7, and 8 imagery (30 m resolution). When Landsat imagery was not available, we first attempted to fill the gap with summer true-color ASTER imagery (15 m resolution), particularly for northern Greenland and Arctic Canada North for ~2000 and ~2010. Where no cloud-free optical data was available, we used summer Radarsat-1 fine beam imagery (8 m resolution) for Northern Greenland in ~2000, and fine beam ALOS PALSAR imagery (10

m resolution) for Northern Ellesmere Island in ~2010, available from the Alaska Satellite Facility (asf.sar.edu). Images were selected as close as possible to the target dates, based on image availability and minimum cloud and snow cover. The date for every glacier outline is almost always within 1 year of the target date. Rates of area change are standardized to annual and decadal values to account for these temporal biases.

We drew a polygon around each terminus to capture the portion of the area that changed from ocean to ice (advance), or ice to ocean (retreat). For glaciers that either advanced from land into the ocean, or retreated from the ocean onto land, we only include the area that was or became ocean at the surface. We then differenced the polygons to determine the area change for each glacier for 2000-2010, 2010-2020, and 2000-2020. The glaciers were mapped using QGIS version 3.10 in the WGS84 Arctic Polar Stereographic projection (EPSG 3995). To eliminate area distortions in the area change calculations, we reprojected each terminus into a unique local orthographic coordinate system to perform the area and error calculations. While we report decadal rates here, many area losses can be sudden, caused by large calving events, which are not captured in our decadal average observations. This is likely most important for ice shelf breakup events (Copland et al., 2007), and glaciers which have a basal instability (Fahrner et al., 2021). It is beyond the scope of this study to determine more precise timing for these breakup events.

We assume that area gain/loss uncertainty is one pixel, with total uncertainty derived by multiplying the length of the perimeter of the changed terminus area by the width of a pixel (30 m for Landsat, 15 m for ASTER, ~10 m for SAR imagery; Krumwiede et al., 2014).

2.2.3 Climate and ocean data

To investigate potential causes of observed changes in terminus position, we assessed ocean and air temperatures, and sea ice concentrations, on or adjacent to each glacier terminus. We derived ocean temperatures from the ECMWF ORAS5 model from 2000 to 2018 (Zuo et al., 2017; Zuo et al., 2019), for the ocean surface and 300 m depth. We used ERA5 modelled 2 m air temperature from 2000 to 2020 (Copernicus, 2019). Both the ocean and air temperature datasets have 0.25° spatial resolution and monthly temporal resolution, which we averaged by decade. We used sea ice concentrations derived from passive microwave observations from 2000 to 2020 (Meier et al., 2017; Peng et al., 2013), with a 25 km spatial resolution and monthly temporal resolution, which we averaged seasonally and annually.

2.3 Results

2.3.1. Hemispheric patterns of marine-terminating glacier change

We identified 1704 Northern Hemisphere glaciers that contacted the ocean between 2000 and 2020 (Table 2.1; Figure 2.1). Collectively, these glaciers experienced a net loss of 7527.3 ± 30.7 km^2 (389.7 ± 1.6 km^2 a^{-1}) over this period, with 1453 (85.3%) retreating, 42 (2.5%) advancing, and 209 (12.3%) not changing within the uncertainty of our methods (Figure 2.2). In total, 123 glaciers (7.2%) that were in contact with the ocean in 2000 had retreated enough by 2020 to terminate on land; 52 of these occurred between 2000-2010, and 71 between 2010-2020 (Table 2.2).

Very few glaciers are responsible for most of the terminus change, with only 23 glaciers, or 1.3% of the total, accounting for 50.3% of total terminus area loss over the period 2000-2020. The top 10 glaciers with the highest rate of terminus area loss are all in Greenland, with only 5

glaciers outside of Greenland in the top 21 (1 in Russia, 1 in Alaska, 3 in Svalbard). This is reflected in the fact that Greenland experienced more terminus area loss than any other region, with ice sheet and periphery glaciers combined accounting for 69.6% of total Northern Hemisphere tidewater ice loss from 2000-2020 (Table 2.1; Figure 2.1).

The rate of terminus loss decreased by 21.4% from 2000-2010 (434.4 ± 3.1 km^2 a^{-1}) to 2010-2020 (341.4 ± 2.87 km^2 a^{-1}), primarily due to a 33.6% decrease in the retreat rate of Greenland Ice Sheet outlet glaciers. In contrast, GICs lost area at a rate 2.5% higher during 2010-2020 than 2000-2010.

2.3.2 Greenland Ice Sheet change

Marine-terminating glaciers of the Greenland Ice Sheet lost an average total area of 241.5 ± 1.2 km^2 a^{-1} from 2000 to 2020 (total area loss of 4774 ± 23 km^2), which accounts for 62.0% of the Northern Hemisphere total. The four glaciers with the largest terminus losses from 2000 to 2020 were Zachariae Isstrøm (total 1452.7 ± 14.4 km^2; mean 72.6 ± 0.72 km^2 a^{-1}: Figure 2.3a), Humboldt (total 236.1 ± 7.9 km^2; mean 13.0 ± 0.44 km^2 a^{-1}: Figure 2.3b), Petermann (total 272.6 ± 4.5 km^2; mean 12.9 ± 0.22 km^2 a^{-1}: Figure 2.3c), and Nioghalvfjerdsbrae (total 206.3 ± 7.3 km^2; mean 10.8 ± 0.38 km^2 a^{-1}). Together, these four glaciers, all of which are in Northern Greenland, accounted for 45.3% of the tidewater glacier terminus area loss from the Greenland Ice Sheet, with Zachariae Isstrøm accounting for 30.1% alone. With the addition of Ostenfeld Harder and Hagen Bræ, this group of six glaciers accounted for 53.3% of total ice sheet area loss.

Only six outlets of the Greenland Ice Sheet (out of 207) had a net advance from 2000 to 2020 (Ryder, Qajuuttap Sermia, Ukaasosuaq, Vestfjord, Store, Heimdal). Of these, the largest

advance occurred at Ryder Glacier for a total of 14.6 ± 1.0 km^2 (mean 0.70 ± 0.05 km^2 a^{-1}); the other five glaciers were all at least an order of magnitude less.

The Greenland Ice Sheet experienced a 33.6% decrease in the rate of terminus area loss during the period 2010-2020 compared to 2000-2010 (Table 2.1). There were five glaciers (Petermann, Zachariae Isstrøm, Hagen Bræ, Ostenfeld Harder, Jakobshavn) that each had a reduction in rate of terminus area loss of more than 10 km^2 a^{-1} (combined total 82.7 km^2 a^{-1}) during 2010-2020 compared to 2000-2010. Together, these account for 85.7% of the total observed reduction in rate of terminus area loss for the ice sheet between the measurement periods. Excluding these five glaciers, the Greenland Ice Sheet experienced a 10.2% reduction in the rate of terminus area loss during 2010-2020 compared to 2000-2010.

2.3.3 GIC change

GICs of the Northern Hemisphere (i.e., those outside of the Greenland Ice Sheet, but including the periphery) lost an average of 148.2 ± 1.1 km^2 a^{-1} from 2000 to 2020 (cumulative total of 2753.6 ± 20.0 km^2; Table 2.1). The collapse of the Matusevich Ice Shelf (Figure 2.3d) in the Russian Arctic was the biggest contributor to this loss. In 2000, six glaciers coalesced on Severnaya Zemlya to form this ice shelf, but between 2010 and 2020 the ice shelf collapsed, and the glacier termini separated, resulting in a combined area loss of 157.7 ± 2.8 km^2 (8.3 ± 0.1 km^2 a^{-1}) from 2000 to 2020. The other major GIC terminus area losses from 2000 to 2020 occurred at a northwest outlet of Flade Isblink (Greenland; total 105.1 ± 2.8 km^2, mean 5.0 ± 0.1 km^2 a^{-1}), Stonebreen (Svalbard; total 77.3 ± 3.2 km^2, mean 4.5 ± 0.1 km^2 a^{-1}: Figure 2.3f), and Columbia Glacier (Alaska; total 49.2 ± 1.4 km^2, mean 2.9 ± 0.1 km^2 a^{-1}: Figure 2.3g).

Together, changes of 50 termini (out of 1496 GICs) accounted for 50.1% of total GIC retreat from 2000 to 2020. The region with the most glaciers in this group of 50 was Russia (21 glaciers), followed by Arctic Canada North and Svalbard (11 each), Greenland periphery (6), and Alaska (1).

There were 36 GIC termini that advanced between 2000 and 2020 outside of our uncertainties (Figure 2.1). Three experienced large advances: Vavilov Ice Cap (Severnaya Zemlya; total 132.6 ± 1.7 km^2, mean 7.0 ± 0.1 km^2 a^{-1}: Figure 2.3i), Basin-3 of Austfonna (Svalbard; total 88.7 ± 2.4 km^2, mean 4.7 ± 0.1 km^2 a^{-1}), and Nathorstbreen (Svalbard; total 64.9 ± 1.6 km^2, mean 3.4 ± 0.1 km^2 a^{-1}). The fourth largest advance was more than an order of magnitude less than these.

The overall rate of GIC terminus area loss increased by 2.5% between 2000-2010 and 2010-2020 (Table 2.1). Alaska and the Russian Arctic saw the largest increase in area loss between the two decades, with losses in 2010-2020 being 83.3% and 39.0% higher, respectively, than in 2000-2010 (Table 2.1; Figure 2.1). Both Iceland and Asia North also experienced increased area loss between these periods, but there is only one marine terminating glacier in each of these regions and together they account for <0.001% of total losses. Greenland periphery experienced a 45.2% decrease in the rate of area loss between the two time periods, the most of any region. Arctic Canada South also lost less area from 2010-2020 compared to 2000-2010, with a reduction of 16.6%. Svalbard and Arctic Canada North both only had minor differences between the two decades.

2.4 Discussion

Our measured retreat of 85.3% of Northern Hemisphere marine-terminating glacier termini over the period 2000-2020, with a combined total area loss of 7527.3 ± 30.7 km^2, is consistent with the widespread loss in area and volume of glaciers reported worldwide (Hugonnet et al., 2021; IPCC, 2021). Our analysis of mean annual 2 m air temperatures on glacier termini show that temperatures rose, on average, 1.99°C between 2000-2010 and 2010-2020. The biggest temperature change occurred in Arctic Russia, where the increase was 3.73°C between the two periods. Mean annual ocean temperatures also increased between these decades, by 0.23°C at the surface and by 0.40°C at 300 m depth. Over the same period there was a 3.8% decline in annual sea ice concentration across all regions.

These patterns suggest that pan-Arctic climate and ocean warming over the past two decades is broadly responsible for the reported losses of glacier termini, as has also been reported elsewhere (IPCC, 2021; Zemp et al., 2015). However, it is also clear that there is high local variability in terminus change rates despite similar environmental changes. For example, in Alaska, Columbia Glacier (Figure 2.3g) retreated 49.2 ± 1.4 km^2 (2000-2020), while 24 km away Meares Glacier gained 0.13 ± 0.1 km^2 (2000-2020). In Arctic Canada North, Mittie Glacier changed the most, losing 34.9 ± 1.2 km^2 (2000-2020), while ~30 km to the east a glacier advanced 0.98 ± 0.2 km^2 (2000-2020). Zachariae Isstrøm lost 1452.7 ± 14.4 km^2 (2000-2020), more than any other glacier in the hemisphere (Figure 2.3a), while two glaciers ~140 km further north didn't change within uncertainty limits. Stonebreen (Figure 2.3f), which had the largest terminus area loss of 77.3 ± 3.2 km^2 (2000-2020) in Svalbard, is only 170 km to the south of Basin-3, which had the largest advance of 88.7 ± 2.4 km^2 (2000-2020) in the archipelago. In Russia, the collapse of the Matusevich Ice Shelf (Figure 2.3d) resulted in the biggest terminus

area loss of 157.7 ± 2.8 km^2 (2000-2020), but two glaciers located further within the same fjord, but not connected to the ice shelf, did not change within uncertainty limits.

From this analysis it is evident that changes in climate and ocean conditions alone cannot explain the wide spatial variability in measured terminus change patterns for marine-terminating glaciers, similar to the findings of Carr et al. (2017). Glaciers are retreating at different rates due to unique local circumstances, with each glacier having different thresholds for, and sensitivity to, change at which point they respond to environmental and other forcings in different ways. To further investigate this, we examined the characteristics of glaciers that cumulatively accounted for >50% of measured terminus area losses for the Greenland Ice Sheet (six glaciers), and for GICs (50 glaciers), with reference to previously published literature where possible (Table 2.3). There are four main characteristics of these glaciers that stand out as explanatory causes for their measured changes:

2.4.1 Ice shelf and ice tongue collapse

Most of the biggest terminus losses from both GICs and the Greenland Ice Sheet were at least partially due to ice shelf or tongue collapse. When an ice shelf or tongue collapses it is typically lost over a short period, ranging from a few hours to a couple of years (Copland et al., 2007; White & Copland, 2019), as opposed to other glaciers that often retreat more consistently through time. For example, on the Greenland Ice Sheet five of the six outlets responsible for 53.3% of the 2000-2020 reduction in ice sheet terminus area lost part or all of their ice shelves or tongues (Table 2.3). Zachariae Isstrøm lost almost its entire ice shelf (Mouginot et al., 2015), although part of it remains but is no longer attached to the glacier (Figure 2.3a). Petermann

(Münchow et al., 2014; Figure 2.3c), Nioghalvfjerdsbrae (Mayer et al., 2018), and Ostenfeld Brikkerne Harder (Hill et al., 2017) glaciers all lost ice tongues during large calving events.

Of the 50 marine-terminating glaciers that comprise 50.1% of Northern Hemisphere GIC losses, there are 17 glaciers that lost an ice shelf or tongue (Table 2.3). The largest of these losses was the Matusevich Ice Shelf, which broke apart in 2012 (Willis et al., 2015). Flade Isblink, in NE Greenland, has several outlets, three of which lost ice tongues (Bendtsen et al., 2017). Several unnamed glaciers in northern Greenland also lost ice shelves. Arctic Canada North lost large parts of the Serson and Petersen ice shelves, and the Marine and Yelverton ice tongues (White & Copland, 2019). Overall, these patterns highlight the strong sensitivity of ice shelves and ice tongues to changes in external forcing (Copland & Mueller, 2017), and the precarious existence of the few remaining such ice masses in the northern hemisphere.

2.4.2 Surging

None of the Greenland Ice Sheet outlet glaciers that lost the largest terminus area are surge-type. However, out of the 50 glaciers with the largest GIC terminus losses, 10 are surge-type and another five are possibly surge-type, despite <1% of global glaciers being surge-type (Sevestre & Benn, 2015). Of these glaciers, eight are in Svalbard, six are in the Russian Arctic, and one is in Arctic Canada North (Table 2.3). The largest losses from surge-type glaciers occurred at Stonebreen (Strozzi et al., 2017; Figure 2.3f), and Braasvellbreen (Moholdt et al., 2010), which retreated 3-5 km^2 a^{-1} between 2000 and 2020. Stonebreen is the largest outlet from the largest ice cap on Edgøya Island, Svalbard (26 km calving front), although the northern and southern parts of the calving front have different dynamic controls (Strozzi et al., 2017). The northern portion of the glacier (which accounts for nearly all the retreat since 2000) surged

between 1936 and 1971, while the southern portion displayed increased velocity and thinning in 2012 followed by a small advance (Strozzi et al., 2017).

Only 42 (of 1704) glaciers had a net advance between 2000 and 2020. Out of the 42 advances, at least 23 occurred on surge-type glaciers (Sevestre & Benn, 2015), accounting for 91.9% of the total measured increase in area. The three biggest advances were due to surge events at Vavilov Ice Cap, Russia (Willis et al., 2018; Fig 2.3I; 132.7 ± 1.7 km^2 for 2000-2020), Basin-3, Svalbard (Dunse et al., 2015; 88.7 ± 2.4 km^2 for 2000-2020), and Nathorstbreen Glacier system, Svalbard (Sund et al., 2014; 64.9 ± 1.6 km^2 for 2000-2020). Because few ice shelves or ice tongues still exist in the Northern Hemisphere today (Copland & Mueller, 2017), and surge-type glaciers are relatively common in the Arctic (Sevestre & Benn, 2015), surge-type glaciers are likely to be even more important in future terminus changes.

2.4.3 Unstable basal geometry

Tidewater glaciers can become unstable when resistive stresses are reduced more than driving stresses, such as when a glacier reaches flotation after retreating from a basal pinning point, which can lead to rapid terminus retreat and collapse (Pfeffer, 2007). At least two glaciers on our list retreated primarily due to their basal geometries. Flowing from the Greenland Ice Sheet, Humboldt Glacier has accelerated its retreat since 1999 along a large basal trough in the northern portion of the terminus (Carr et al., 2015). This glacier was the second largest contributor to area change in the Northern Hemisphere since 2000, and has the widest terminus in the hemisphere (90 km), amplifying the impact of even small length changes.

Columbia Glacier is the only GIC that is known to have experienced retreat driven by basal geometry (O'Neel et al., 2005), out of the 50 glaciers that make up 50.1% of GIC terminus

area loss. Columbia Glacier lost an average of 2.9 ± 0.1 km^2 a^{-1} from 2000-2020 due to continued long term retreat into deeper water that resulted in higher velocities and calving rates (O'Neel et al., 2005). It is possible that other glaciers have also experienced retreat due to their basal geometries, but the lack of comprehensive ice thickness and bathymetric information close to glacier termini makes this difficult to quantify. We are therefore likely undercounting the importance of unstable basal geometry in causing rapid terminus retreat, and future work should focus on measuring the basal topography of tidewater glaciers to better understand this phenomena.

2.4.4 Unusually wide calving margins

For GICs, the above explanations account for 33 of the 50 glaciers with the largest area losses. Of the remaining 17 glaciers, four of these are large ice caps. Kvitøyjøkulen is one of these with an area of 600 km^2 in the Barents Sea (Figure 2.3h), which is undivided and therefore has a calving margin width of 85.4 km, the widest of any GIC. Similarly, there are three ice caps in Franz Josef Land that are not subdivided and have calving widths between 38 and 55 km, which puts them in the 99th percentile of all calving front widths. Ten additional glaciers have a calving front width between 15 and 44 km, which is in the 97th percentile. The remaining three GICs (2 in Arctic Canada North, 1 in the Russian Arctic) have calving front widths between 6 and 10 km, within the 88th percentile. Ice masses with wide calving margins are likely particularly sensitive to oceanographic changes, while also producing large area losses for relatively short length changes. Although subdivision of large ice caps into smaller basins would reduce the area lost per basin, this connection to calving margin width also highlights the potential influence of oceanographic factors.

2.5 Conclusions

Our study provides the first complete count of the number of marine-terminating glaciers in the Northern Hemisphere, with a total of 1704 in 2000 and 1581 in 2020. There has been widespread loss of their termini, with 85.3% of glaciers retreating from 2000-2020 and only 2.5% advancing. However, there have been wide variations in the rate of terminus retreat within fjords, regions, and across the hemisphere. While climate and ocean warming, and associated negative mass balance, has been a dominant factor in global glacier retreat (IPCC, 2021), the high spatial variability in marine-terminating glacier retreat rates is primarily dependent on their local characteristics. Glaciers that terminated in ice shelves or ice tongues retreated the fastest. Surge-type glaciers, glaciers with unstable basal geometries, and those with wide calving margins (e.g. ice caps) showed the next biggest changes. These unique factors to each glacier are more important in determining glacier sensitivity and thresholds to climate change than environmental factors alone.

Greenland, including the ice sheet and periphery glaciers, accounted for 69.6% of total hemispheric marine terminating glacier terminus area loss. Only six outlets of the Greenland Ice Sheet and 50 GICs account for more than 50% of the total terminus area loss in each group. This small number of glaciers has had an outsized impact on the rate of terminus loss in the hemisphere. Monitoring glaciers that have already undergone large changes is important as ice dynamics are tied to terminus retreat, as recent examples from Greenland show (King et al., 2020). We have identified specific glacier characteristics that are conducive to retreat and suggest that future study of similar glaciers is important in predicting the response of ice masses to climate change and their contribution to future sea level rise.

The only remaining ice shelves in the Arctic today are found off the north coast of Arctic Canada North, northern Greenland, and Franz Josef Land (Copland & Mueller, 2017). Given the large losses from ice shelves and ice tongues over the last two decades, these locations may also dominate glacier terminus losses in the coming decades, although exhaustion of supply will be a factor once all ice shelves and ice tongues are lost. Because surge-type glaciers have displayed large retreats in recent decades, and given that surge-type marine-terminating glaciers are common across Arctic Canada North, Greenland, Svalbard, Alaska, and the Russian Arctic (Sevestre & Benn, 2015), these are key places to monitor for large retreats and advances in the future.

Table 2.1. Number and change in area of marine-terminating glaciers across the Northern Hemisphere between 2000, 2010 and 2020, by region. See Figure 2.1 for location of regions.

Region	Number of glaciers in 2000	Net area change 2000-2010 (km^2 a^{-1})	Net area change 2010-2020 (km^2 a^{-1})	Net area change 2000-2020 (km^2 a^{-1})	Net area change 2000-2020 (km^2)
Alaska	42	-2.46 ± 0.14	-4.51 ± 0.21	-3.52 ± 0.10	-60.4 ± 1.8
Arctic Canada North	252	-28.96 ± 0.79	-28.78 ± 0.82	-29.09 ± 0.40	-545.7 ± 7.6
Arctic Canada South	86	-1.02 ± 0.08	-0.85 ± 0.07	-0.93 ± 0.04	-16.9 ± 0.7
Asia North	1	0.00 ± 0.01	-0.01 ± 0.01	0.00 ± 0.00	-0.1 ± 0.1
Greenland Ice Sheet	208	-287.54 ± 2.45	-190.99 ± 1.81	-241.47 ± 1.19	-4773.7 ± 23.4
Greenland Periphery	537	-37.10 ± 0.63	-20.32 ± 0.63	-29.92 ± 0.34	-558.2 ± 6.6
Iceland	1	-0.21 ± 0.03	-0.49 ± 0.04	-0.32 ± 0.02	-5.7 ± 0.3
Russian Arctic	411	-49.75 ± 1.38	-69.14 ± 1.63	-57.67 ± 0.74	-1091.5 ± 14.1
Svalbard and Jan Mayen	166	-27.33 ± 0.98	-26.34 ± 1.10	-26.79 ± 0.54	-475.0 ± 9.7
Greenland total	745	-324.63 ± 2.52	-211.30 ± 1.91	-271.39 ± 1.24	-5331.9 ± 24.3
Glacier and ice cap total	1496	-146.83 ± 1.97	-150.44 ± 2.23	-148.24 ± 1.06	-2753.6 ± 20.0
Northern Hemisphere total	1704	-434.37 ± 3.14	-341.42 ± 2.87	-389.71 ± 1.59	-7527.3 ± 30.7

Table 2.2 Number of marine-terminating glaciers in the Northern Hemisphere to retreat, advance, and cease to be marine-terminating by time period.

Region	Number of glaciers in 2000	Glaciers that retreated 2000-2010	Glaciers that advanced 2000-2010	Glaciers that became land terminating 2000-2010	Glaciers that retreated 2010-2020	Glaciers that advanced 2010-2020	Glaciers that became land terminating 2010-2020	Glaciers that retreated 2000-2020	Glaciers that advanced 2000-2020	Glaciers that became land terminating 2000-2020
Alaska	42	12	8	1	19	9	1	19	11	2
Arctic Canada North	252	165	7	3	168	5	4	204	7	7
Arctic Canada South	86	40	0	12	32	0	10	48	0	22
Asia North	1	0	0	0	0	0	0	1	0	0
Greenland Ice Sheet	208	186	5	3	169	12	0	190	6	3
Greenland Periphery	537	288	9	30	247	6	42	366	2	72
Iceland	1	1	0	0	1	0	0	1	0	0
Russian Arctic	411	319	6	1	318	6	1	375	5	2
Svalbard and Jan Mayen	166	120	12	2	111	13	13	126	11	15
Greenland total	745	474	14	33	416	18	42	556	8	75
GIC total	1496	945	42	49	896	39	71	1140	36	120
Total	1704	1131	47	52	1065	51	71	1330	42	123

Table 2.3. The fastest retreating marine-terminating glaciers in the Northern Hemisphere (sum is >50% of total area lost). The category column indicates which group the glacier belongs in: the Greenland Ice Sheet (GrIS) or glaciers and ice caps (GIC).

Glacier name	Database_ID	Latitude	Longitude	Net area change per year 2000-2020 (km^2 a^{-1})	Category	Main cause of terminus retreat	Reference
Zachariae Isstrom	ZACHARIAE_ISSTROM	78.783	-20.073	-72.65	GrIS	Ice shelf	Mouginot et al., 2015
Humboldt Gletscher	HUMBOLDT_GLETSCHER	79.583	-64.916	-13.02	GrIS	Unstable basal geometry	Carr et al., 2015
Petermann Gletscher	PETERMANN_GLETSCHER	81.052	-61.515	-12.94	GrIS	Ice tongue	Münchow et al., 2014
Nioghalvfjerdsbrae	NIOGHALVFJERDSFJORDEN	79.622	-19.848	-10.78	GrIS	Ice tongue	Mayer et al., 2018
Ostenfeld and Harder Gletschers	OSTENFELD_HARDER_GLETSCHER	81.680	-45.771	-10.21	GrIS	Ice tongue	Hill et al., 2017
Hagen Brae	HAGEN_BRAE	81.464	-27.048	-9.19	GrIS	Ice tongue	Hill et al., 2017
Karpinsky Ice Cap (October Revolution Island)	RGI60-09.00515_2	79.904	98.186	-5.53	GIC	Ice shelf	Willis et al., 2015
Flade Isblink Ice Cap	RGI60-05.10315_8	81.692	-16.143	-5.00	GIC	Ice tongue	Bendtsen et al., 2017
Stonebreen	RGI60-07.01554	77.850	24.083	-4.53	GIC	Surge-type	Strozzi et al., 2017
Braasvellbreen	RGI60-07.00025	79.258	23.346	-3.14	GIC	Surge-type	Moholdt et al., 2010
Flade Isblink Ice Cap	RGI60-05.10315_4	81.754	-15.204	-3.05	GIC	Ice tongue	Bendtsen et al., 2017
Columbia Glacier	RGI60-01.10689	61.148	-147.083	-2.89	GIC	Unstable basal geometry	Enderlin et al., 2018
Kvitøyjøkulen	RGI60-07.01394	80.193	32.440	-2.81	GIC	Very wide calving margin (>30 km)	
Ushakova Ice Cap (Ushakova Island)	RGI60-09.00909	80.807	79.461	-2.39	GIC	Very wide calving margin (>30 km)	
Unknown	RGI60-05.10983	83.453	-39.299	-2.08	GIC	Ice shelf	

Negribreen	RGI60-07.01506	78.545	19.232	-2.07	GIC	Surge-type	Haga et al., 2020
Mittie	RGI60-03.01517	76.930	-79.051	-2.04	GIC	Surge-type	Van Wychen et al., 2014
Petersen	RGI60-03.03449	82.494	-81.953	-1.93	GIC	Ice shelf	White et al., 2018
Unknown	RGI60-05.11001	83.465	-37.423	-1.85	GIC	Ice tongue	
Serson	RGI60-03.03997	82.283	-85.869	-1.56	GIC	Ice shelf	Mueller et al., 2017
Easter Island South	RGI60-03.01678	77.584	-77.983	-1.41	GIC	Very wide calving margin (>30 km)	
Flade Isblink Ice Cap	RGI60-05.10315_5	81.735	-14.353	-1.32	GIC	Ice tongue	Bendtsen et al., 2017
Rusanov Ice Cap (October Revolution Island)	RGI60-09.00498_2	79.823	97.760	-1.27	GIC	Ice shelf	Willis et al., 2015
Hinlopenbreen and Oslobreen	RGI60-07.01559	79.124	18.991	-1.25	GIC	Surge-type	Flink et al., 2018
Schmidt Ice Cap (Schmidt Island)	RGI60-09.00520	81.086	90.947	-1.23	GIC	Very wide calving margin (>30 km)	
Yelverton	RGI60-03.03389	81.918	-79.674	-1.18	GIC	Ice tongue	White et al., 2019
Karpinsky Ice Cap (October Revolution Island)	RGI60-09.00515	79.833	97.944	-1.17	GIC	Ice shelf	Willis et al., 2015
Trinity Glacier	RGI60-03.01710_3	77.954	-78.457	-1.08	GIC	Calving margin (>6 km)	
Windy Ice Cap (Graham Bell Island)	RGI60-09.00807	80.860	65.087	-1.08	GIC	Very wide calving margin (>30 km)	
Flade Isblink Ice Cap	RGI60-05.10315_2	80.952	-13.900	-1.04	GIC	Ice tongue	
Znamenity Glacier	RGI60-09.00744	80.489	61.504	-1.02	GIC	Ice shelf	Dowdeswell et al., 1994
Academy of Sciences Ice Cap	RGI60-09.00969	80.527	92.776	-0.99	GIC	Very wide calving margin (>30 km)	

(Komsomolets Island)							
Devon Island Glacier	RGI60-03.02469	74.819	-80.271	-0.98	GIC	Wide calving margin (>15 km)	
Vilkitskiy	RGI60-09.00057	75.612	58.404	-0.97	GIC	Surge-type (possibly)	Grant et al., 2009
Austfonna Leighbreen	RGI60-07.00062	80.152	26.576	-0.95	GIC	Wide calving margin (>15 km)	
Brousilov Ice Cap (Prince George Land)	RGI60-09.00697	80.564	50.925	-0.92	GIC	Ice shelf	Dowdeswell et al., 1994
Vostok-4 Ice Cap (Eva-Liv Island)	RGI60-09.01065	81.646	63.034	-0.90	GIC	Very wide calving margin (>30 km)	
Marine Glacier	RGI60-03.02667	82.420	-82.784	-0.90	GIC	Ice tongue	White et al., 2019
Nordenskiold and North Island Novaya Zemlya	RGI60-09.00077	75.323	57.932	-0.89	GIC	Surge-type	Grant et al., 2009
Devon Ice Cap Southeast2 Glacier	RGI60-03.02467	74.996	-80.324	-0.89	GIC	Calving margin (>6 km)	
Chernyshev	RGI60-09.00136	76.030	60.960	-0.87	GIC	Surge-type (likely)	Grant et al., 2009
Moshchnyy	RGI60-09.00065	75.531	62.840	-0.87	GIC	Surge-type (possibly)	Grant et al., 2009
Severny Island Ice Cap (Severny Island)	RGI60-09.00114	75.452	61.909	-0.84	GIC	Calving margin (>6 km)	
Storbreen	RGI60-07.00238	77.073	16.376	-0.81	GIC	Surge-type	Strzelecki et al., 2020
Hochstetterbreen	RGI60-07.01560	78.901	20.541	-0.81	GIC	Surge-type	Ottesen et al., 2017
Sonklarbreen	RGI60-07.00892	78.697	20.340	-0.77	GIC	Surge-type	Ottesen et al., 2017
Severny Island Ice Cap (Severny Island)	RGI60-09.00945	76.693	66.371	-0.76	GIC	Surge-type (possibly)	Grant et al., 2009

Moon Ice Cap (Alexandra Land)	RGI60-09.00708	80.652	45.881	-0.75	GIC	Wide calving margin (>15 km)	
Austfonna	RGI60-07.00029	79.640	26.173	-0.72	GIC	Wide calving margin (>15 km)	
Unknown	RGI60-03.03560	82.720	-81.627	-0.72	GIC	Ice shelf	Mortimer et al., 2012
Etonbreen: Austfonna	RGI60-07.00681	79.726	21.846	-0.69	GIC	Surge-type	Dowdeswell et al., 1991
Krivosheina	RGI60-09.00088	75.744	58.803	-0.68	GIC	Surge-type (possibly)	Grant et al., 2009
M'Clintock	RGI60-03.02668	82.478	-76.134	-0.67	GIC	Ice tongue	White et al., 2018
Vostok-1 Ice Cap (La Ronciere Island)	RGI60-09.00808	80.904	60.695	-0.67	GIC	Wide calving margin (>15 km)	
(Rudolph Island)	RGI60-09.00860	81.761	59.136	-0.66	GIC	Wide calving margin (>15 km)	
Tyndall Ice Cap (Hall Island)	RGI60-09.00743	80.728	62.125	-0.64	GIC	Wide calving margin (>15 km)	

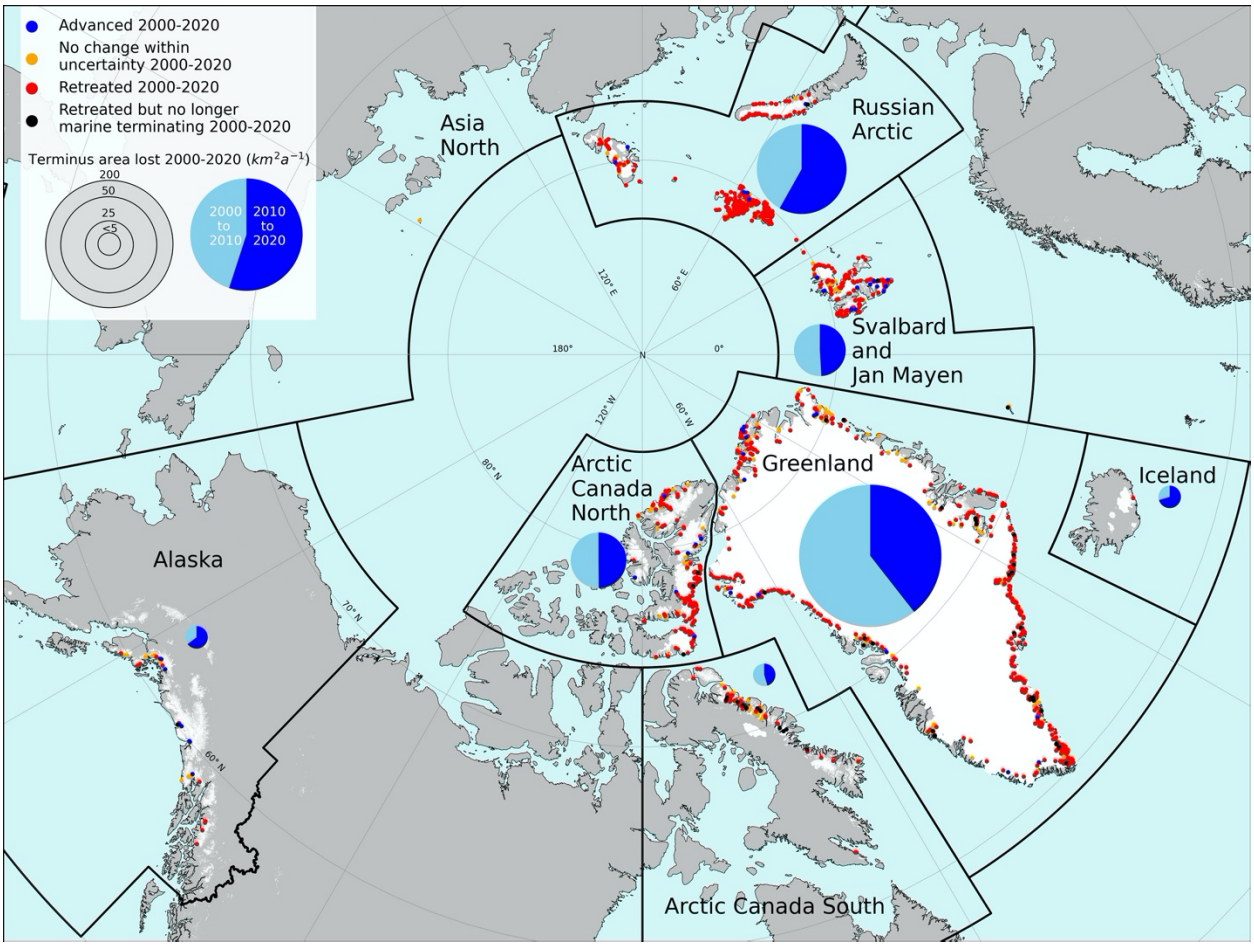


Figure 2.1 Distribution and change of marine-terminating glacier terminus area for 2000 to 2020. Circles are scaled (non-linearly) to the area loss of each major region in the Randolph Glacier Inventory.

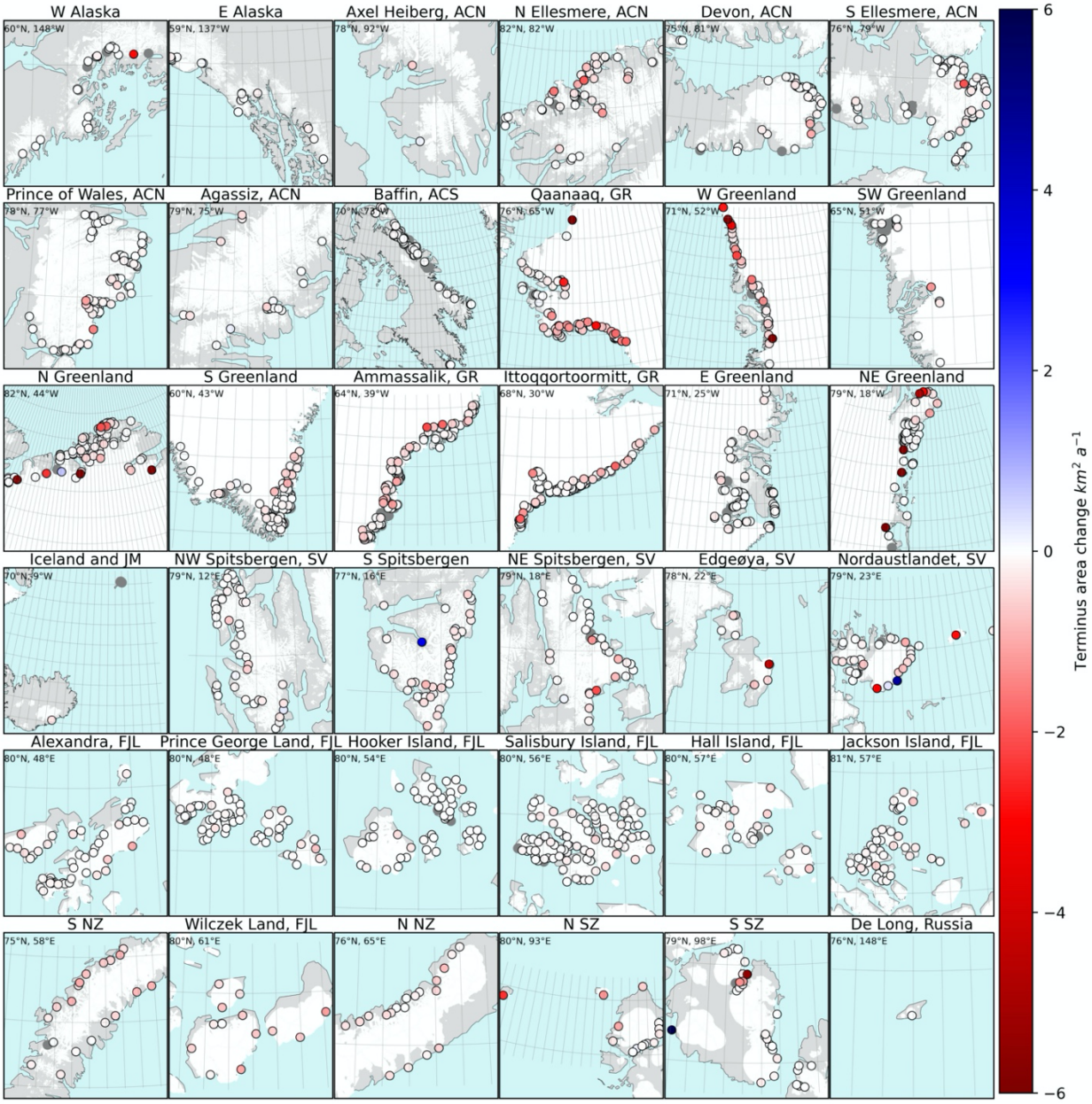


Figure 2.2 Change in the terminus area of Northern Hemisphere marine-terminating glaciers from 2000 to 2020. Subregions are shown from west to east across the hemisphere. Retreats of > 6 km^2 a^{-1} are saturated as dark blue. Abbreviations: Arctic Canada North (ACN), Arctic Canada South (ACS), GR (Greenland), Svalbard (SV), Franz Josef Land (FJL), Novaya Zemlya (NZ), Severnaya Zemlya (SZ); all other abbreviations are cardinal directions.

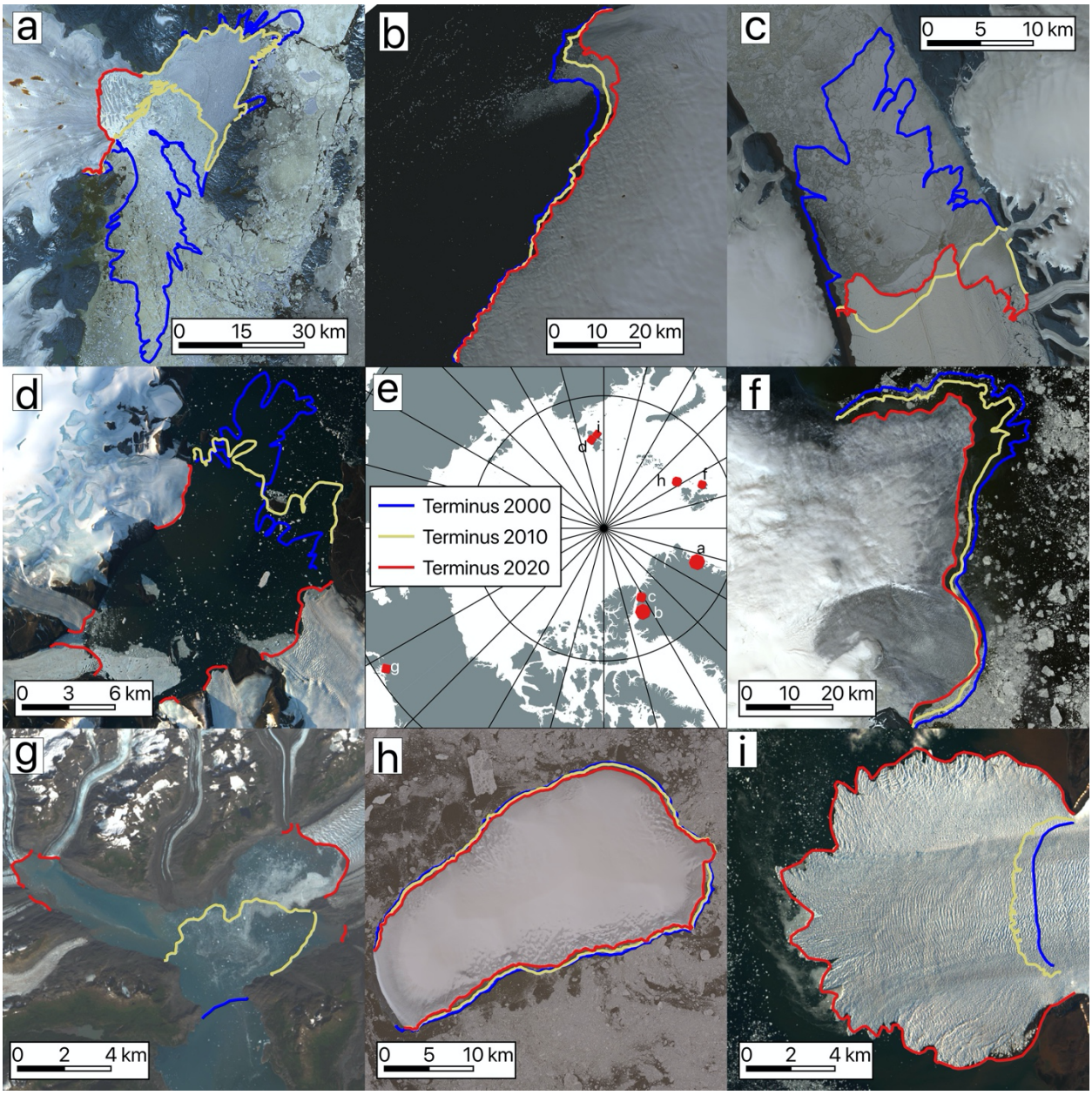


Figure 2.3 Examples of glaciers with major changes from 2000 to 2020: a) Zachariae Isstrøm, loss after ice shelf collapse (base image: Landsat 8, 24 August 2019); b) Humboldt, loss due to unstable basal geometry (Landsat 8, 17 August 2020); c) Petermann, loss after ice tongue collapse (Landsat 8, 8 July 2020); d) Matusevich, loss after ice shelf collapse (Landsat 8, 26 August 2019); e) Location of glaciers shown in other subplots; f) Stonebreen, loss after surging (Landsat 8, 2 August 2019); g) Columbia, loss due to unstable basal geometry (Landsat 8, 8 August 2019); h) Kvitøyjøkulen, loss due to wide calving margin (Landsat 8, 5 August 2019); i) Vavilov Ice Cap, gain due to surging (Landsat 8, 26 August 2019).

Chapter 3: Frontal ablation: the unquantified mass loss of Northern Hemisphere marine-terminating glaciers, 2000-2020

3.1 Introduction

When glaciers terminate in the ocean, mass is lost by frontal ablation at the ice-ocean interface, including mass loss due to iceberg calving (i.e. the mechanical release of icebergs or smaller pieces of ice to the ocean), submarine frontal melting, and subaerial frontal melting and sublimation (Cogley et al., 2011). Quantifying frontal ablation is essential to partitioning glacier mass loss components, which informs sea-level budgets, estimates of glacier freshwater contributions to the ocean, impacts on marine ecosystems and iceberg hazards. Recent model results suggest that Northern Hemisphere frontal ablation from glaciers (i.e., excluding the Greenland Ice Sheet) was around 39 Gt a^{-1} from 1980-1999 (Huss & Hock, 2015). Frontal ablation accounted for 10% of the 882 Gt a^{-1} global glacier ablation rate (which includes surface melt), although about half of this occurred in the Southern Hemisphere (Huss & Hock, 2015). The same modeling study projected a Northern Hemisphere frontal ablation rate of 50.6 ± 23.8 Gt a^{-1} for 2020-2040 (Huss & Hock, 2015). However, observation-based estimates of frontal ablation have been limited, partially because many studies only quantify ice discharge (Sánchez-Gámez et al., 2019; Van Wychen et al., 2021) as they do not include mass changes due to terminus retreat or advance, or these are only computed for individual glaciers (Schellenberger et al., 2015). Alaska (McNabb et al., 2015) and Svalbard (Błaszczyk et al., 2009) are the only regions in the Northern Hemisphere with complete observation-based frontal ablation estimates, but these have not been updated since 2013.

Whereas many regional-scale studies have derived regional total glacier mass changes from glaciological and geodetic methods (Hugonnet et al., 2021; RGI Consortium, 2017; Tepes

et al., 2021; Zemp et al., 2019), satellite gravimetry (Ciracì et al., 2020; Wouters et al., 2019), and numerical modeling (Noël et al., 2017; Noël et al., 2018; Østby et al., 2017), no study has determined the frontal ablation rate for the entire Northern Hemisphere. This has mainly been due to a previous lack of spatially and temporally consistent glacier ice thickness, surface velocity and terminus position observations, from either field or remote sensing surveys, which is exacerbated at high latitudes.

Here we identify every marine-terminating glacier in the Northern Hemisphere, distinct from the Greenland Ice Sheet, and use measurements or estimates of ice thickness, surface velocity, and terminus position changes, together with a climatic mass balance model, to estimate mean frontal ablation (see Methods, Section 3.6). We split the observations into two periods: 2000 to 2010 and 2010 to 2020. The former decade is based on terminus position observations from summer 2000 and 2010, and velocity observations from 2000 to 2009. The latter decade is based on terminus position observations from summer 2010 and 2020, and velocity observations from 2010 to 2019. Because directly measuring frontal ablation components (i.e. calving, sublimation, and melting) is difficult, we estimate frontal ablation indirectly, by calculating ice discharge (i.e. mass flux through a flux gate perpendicular to glacier flow upstream of the terminus) and mass change due to retreat or advance (henceforth, terminus mass change), while accounting for the climatic mass balance (i.e. the mass changes due to snow accumulation, surface melt and refreezing) below the flux gate. Our computation of frontal ablation excludes submarine melting below floating tongues, but this is likely negligible as virtually no floating glacier tongues remain in the Arctic (Dowdeswell, 2017; White & Copland, 2019). The residual examples are primarily within Franz Josef Land, Russia (Dowdeswell, 2017).

3.2 Complete hemispheric estimates of discharge and terminus change

Guided by the Randolph Glacier Inventory version 6.0 (RGI6) (Pfeffer et al., 2014; RGI Consortium, 2017), we identified 1496 marine-terminating glaciers and manually mapped their terminus positions in summer 2000, 2010 and 2020 from satellite imagery (see Methods, Section 3.6) (Kochtitzky & Copland, 2022). The Greenland Periphery has the most marine-terminating glaciers (537), followed by the Russian Arctic (412), Arctic Canada North (252), Svalbard and Jan Mayen (160 + 6 = 166; hereafter Svalbard), Arctic Canada South (86), Alaska (42), and Iceland (1). However, the length of terminus flux gates in Russia is more than three times that of Greenland Periphery glaciers (Table 3.1). North Asia has one small marine-terminating glacier on one of the De Long Islands, and we therefore include it in the Russian Arctic RGI6 region. Between 2000 and 2010, 49 of the marine-terminating glaciers lost contact with the ocean and became land-terminating, with another 120 glaciers following in the next decade.

The frontal ablation rate from all 1496 glaciers was 44.47 ± 6.23 Gt a^{-1} (all uncertainties given at the 95% confidence level, i.e. two standard deviations) between 2000-2010, and 51.98 ± 4.62 Gt a^{-1} between 2010-2020 (Table 3.1). While this suggests a slight increase in frontal ablation between the two decades, the estimates are within the uncertainties of each other. Ice discharge accounted for 80% and 78% of the frontal ablation for 2000-2010 and 2010-2020, respectively, with the remaining losses due to terminus retreat. Rates of frontal ablation, ice discharge, and terminus mass loss did not vary significantly (i.e. non-overlapping uncertainties) between 2000-2010 and 2010-2020, with few exceptions (Table 3.1). In Alaska, terminus mass loss increased tenfold while ice discharge decreased by about 15%. In Svalbard, ice discharge more than doubled, primarily due to the surge of Basin-3 of Austfonna ice cap. Owing to

improved data quality during 2010-2020 and smaller uncertainties, we focus primarily on estimates from this decade, unless otherwise specified.

Among the seven glacierized regions studied, the Russian Arctic experienced the highest frontal ablation rate, followed by Svalbard and Alaska (Table 3.1; Figure 3.1). Greenland Periphery and Arctic Canada North had similar frontal ablation rates, while Iceland and Arctic Canada South were markedly lower (Table 3.1; Figure 3.1). From 2000-2010 Hubbard Glacier in Alaska showed the highest frontal ablation rate (4.13 ± 0.0 Gt a^{-1}) for a single glacier, but was surpassed by Basin-3 of Austfonna in Svalbard (6.10 ± 0.24 Gt a^{-1}) during the next decade (Figure 3.2).

Even though Arctic Canada North has 40% of the total Northern Hemisphere area of marine-terminating glaciers, Alaska, Svalbard, and the Russian Arctic each produce more frontal ablation. The Russian Arctic contains 22% of the marine-terminating glacier area, but it accounts for 33% of total frontal ablation.

3.3 Uneven distribution of frontal ablation across all regions

Within each region, a few large glaciers have a disproportionate impact on the total frontal ablation over the study period (Figures 3.2, 3.3, 3.4, 3.5). In Svalbard and the Russian Arctic, 27% and 32% of glaciers (i.e. 61% and 80% of regional marine-terminating glacier area), respectively, make up 90% of the regional frontal ablation rate. A similar, small number of glaciers make up about 90% of frontal ablation in other regions as well, including 24% of glaciers in Arctic Canada North, 14% in Alaska, 28% in Greenland Periphery, and 28% in Arctic Canada South. In total, merely 1% (15 out of 1496) of marine-terminating glaciers account for

45% of Northern Hemisphere frontal ablation, and 2% (30 glaciers) account for 55% of frontal ablation.

Most marine-terminating glaciers (87% of the 1496 glaciers) contribute less than 0.04 Gt a^{-1} to the ocean, together accounting for ~14% of Northern Hemisphere frontal ablation. Hence, further studies should focus on the ~200 marine-terminating glaciers contributing more than 0.04 Gt a^{-1}, although future glacier changes (e.g. due to surging (Meier & Post, 1969), or the tidewater glacier cycle (Meier & Post, 1987)) will modify this list.

To investigate which parts of the ocean are most affected by frontal ablation, and thus susceptible to related iceberg hazards and marine ecosystem impacts, we introduce an 'intensity index' that spatially aggregates frontal ablation from all glaciers occurring within 50 km of any point in the ocean on a 10 km grid (Figure 3.6). The index depends on both the frontal ablation rate and the number of glaciers in the vicinity of each point, and thus varies in a pattern that is largely consistent with the spatial variation in frontal ablation of glaciers in each ocean region (Figures 3.2 and 3.4). Several coastal regions show exceptionally high intensity indices, indicating hotspots of potential iceberg occurrence.

The highest intensity index occurs around northeastern Svalbard, due to the vigorous surge of Basin-3 of Austfonna which started in 2012 (Dunse et al., 2015), in addition to substantial contributions from the rest of the ~1200 km^2 ice cap. High indices are also present in the strait between October Revolution and Komsomolets islands in Severnaya Zemlya (Figure 3.6), partly due to recent ice shelf break up (Dowdeswell, 2017; Willis et al., 2015). In Alaska, high indices close to Hubbard and Columbia glaciers are due to exceptionally high frontal ablation rates of these glaciers; these alone accounted for 63% of regional frontal ablation and are thus the conduits for most ice entering the Gulf of Alaska. Higher intensity indices along the

western coast than the eastern coast of Novaya Zemlya is also consistent with a concentration of glaciers with high frontal ablation rates. Despite the relative low frontal ablation rates (mean 0.02 Gt a^{-1}) of glaciers in Franz Josef Land, the large number of glaciers there yields a high index.

3.4 Role of ice discharge versus terminus retreat

Quantifying the relative importance of ice discharge versus terminus retreat is key to understanding mass loss mechanisms and highlights where future efforts should be focused to reduce observational uncertainties. Terminus retreat was most important in Arctic Canada South, Arctic Canada North, and Greenland Periphery, where it made up 67%, 48%, and 41%, respectively, of total frontal ablation, while only amounting to 8% in Alaska. Thus, ice discharge is dominant in controlling frontal ablation rates in Alaska.

For a retreating glacier, frontal ablation is larger than ice discharge across the flux gate; conversely, for an advancing glacier, frontal ablation is lower than ice discharge. Two examples in Severnaya Zemlya illustrate the connection between terminus change and frontal ablation. We found that the eight glaciers that fed the now collapsed Matusevich Ice Shelf (Willis et al., 2015) had a frontal ablation rate of 0.20 ± 0.17 Gt a^{-1} from 2000-2010, compared to 1.88 ± 0.23 Gt a^{-1} in 2010-2020 due to the 18.91 ± 0.28 km^2 a^{-1} terminus retreat during that decade, the largest of any Northern Hemisphere glacier. On the other hand, the surging outlet of Vavilov Ice Cap (Willis et al., 2018) discharged 1.24 ± 0.01 Gt a^{-1}, but frontal ablation was only 0.29 ± 0.10 Gt a^{-1}, due to terminus advance. Both these events are unique because the Matusevich Ice Shelf is now gone, and Vavilov Ice Cap is unlikely to surge again in the coming decades as no previous surge events have been identified since at least the 1980s, indicating a very long quiescent phase (Dowdeswell & Williams, 1997; Willis et al., 2018). For the entire Northern Hemisphere, the

total terminus mass loss of 11.57 ± 3.81 Gt a^{-1} during 2010-2020 consisted of 2.98 ± 0.70 Gt a^{-1} of terminus advance and 14.54 ± 5.97 Gt a^{-1} of terminus retreat.

We examined glaciers with advancing termini for morphological indicators (Jiskoot, 2011) consistent with dynamic instabilities such as surging or pulsing (hereafter surge-type glaciers). During the surge phase, these glaciers have elevated velocities, typically by an order of magnitude or more above normal, for months to years, which can lead to increased frontal ablation over a similar period (Jiskoot et al., 2001; Mansell et al., 2012; Van Wychen et al., 2016). Of the 45 glaciers that advanced during the 2000-2010 period, we found 13 confirmed, two probable, and five possible surge-type glaciers, whereas 25 showed no signs of instability, in total accounting for 6.74 ± 0.40 Gt a^{-1} of frontal ablation. From 2010-2020, 39 glaciers advanced, of which 14 were confirmed, five probable, and four possible surge-type glaciers, while 16 showed no signs of instability, in total accounting for 11.19 ± 0.71 Gt a^{-1}. Only 13 glaciers, six of which are surge-type, advanced over both 2000-2010 and 2010-2020, compared to 745 glaciers that retreated during both time periods.

3.5 Conclusions and comparisons with regional mass balance

Total glacier mass balance is equal to the climatic-basal balance (the mass changes at the surface, inside, and under a glacier) and frontal ablation (Cogley et al., 2011). We subtract our frontal ablation estimates from total mass balance estimates (Hugonnet et al., 2021) derived from elevation change observations of all glaciers in a region to estimate the climatic-basal balance. Since these estimates (Hugonnet et al., 2021) do not include any mass changes below sea level due to retreat or advance, we correct these geodetic balances assuming two end-member scenarios (see Methods, Section 3.6) of 5.16 to 9.29 Gt a^{-1} of ice lost below sea level from 2000

to 2020. This suggests that the Northern Hemisphere glacier net mass loss of 223.7 ± 14.6 Gt a^{-1} from 2000-2020 by Hugonnet et al. (2021) is currently underestimated by 2-4%, although this portion will not contribute to sea-level rise. We find a total mass loss due to ice discharge equivalent to 2.10 ± 0.22 mm of sea level rise between 2000 and 2020 (accounting for the effect of displacement of ocean water by changes in submarine ice; see Methods, Section 3.6), with an additional 0.11 ± 0.11 mm coming from terminus mass loss above sea level.

In the Russian Arctic, frontal ablation is greater (by 6.38 ± 5.27 Gt a^{-1}) than the total net mass loss rate, suggesting a positive regional climatic-basal balance. We estimate a climatic-basal balance close to zero (1.71 ± 3.45 Gt a^{-1}) in Svalbard, which has overlapping uncertainties with published estimates (Noël et al., 2020; Schuler et al., 2020). All other regions have negative climatic-basal balances. Estimates of climatic-basal balance exist for one other region, Greenland Periphery (Noël et al., 2017), with which we find agreement.

While it should be possible to compare our results with recent observations of Greenland Ice Sheet ice discharge (King et al., 2020; Mankoff et al., 2020), the ice sheet currently lacks discharge estimates for approximately 77 to 211 of the slower flowing ice sheet outlet glaciers, dependent on how outlet margins are combined or separated. Furthermore, recent studies of Greenland Ice Sheet discharge (King et al., 2020; Mankoff et al., 2020) include some peripheral glaciers and do not account for mass changes due to terminus advance or retreat, making the comparison less useful. Even so, our hemispheric ice discharge estimate is an order of magnitude lower than the most recent Greenland Ice Sheet discharge estimates (King et al., 2020; Mankoff et al., 2020).

Even though the 1496 marine-terminating glaciers comprise only 0.007% of Northern Hemisphere glaciers by count, our first Northern Hemisphere wide frontal ablation estimate

indicates that they play a critical role in global glacier mass balance through mass losses by frontal ablation. Our individual glacier estimates provide valuable information for calibrating global glacier models, as well as for coastal communities affected by icebergs and related navigational hazards, and for assessing glacier impacts on near-coastal marine ecosystems.

3.6 Methods

3.6.1 Marine-terminating glacier inventory

We identified every glacier that had an interface with the ocean during at least part of a daily tidal cycle by manual examination of Landsat 5, Landsat 7, and ASTER imagery from 1999 to 2020. The only glacier not touching the ocean between 1999-2002 was Good Friday Glacier (Arctic Canada North), which advanced to become marine-terminating between 2000 and 2010 (Medrzycka et al., 2019), yielding a total of 1496 marine-terminating glaciers in the Northern Hemisphere.

For Greenland Periphery, beyond the ice-sheet margin, we included glaciers that were defined by Rastner et al. (2012) as having either a weak (CL1) or no (CL0) hydrological connection to the ice sheet. Our total number of glaciers and terminus outlines differs from classification of the RGI6 due to missing glaciers (RGI Consortium, 2017), poorly mapped ones, and misclassified terminus types. Poorly mapped glaciers in RGI6 include those with multiple distinct termini and glaciers that share one terminus (mostly in Svalbard).

3.6.2 Flux gates

We drew 5016 km of flux gates manually, although after correcting fluxgate width to be perpendicular to flow the total length is 3802 km (Table 1). We drew fluxgates with a preference

for near-terminus locations where ice thickness observations exist (Figure 3.7). If no thickness observations were available, flux gates were drawn as close to the terminus as practical without entering an area that was lost (median distance from the terminus in 2010 was 630 m). Flux gates are constrained horizontally by a lightly edited (to have one terminus per glacier) version of RGI6 (RGI Consortium, 2017). Unconstrained ice caps that terminate in the ocean, such as those found in the Russian Arctic, have one flux gate that encircles the ice cap. Flux gates were drawn approximately perpendicular to flow direction based on the orientation of medial moraines, structural patterns of other surface-flow features, and/or the orientation of valley walls. We used the x and y component velocity observations to adjust the flux gate width such that the entire width of all flux gates were perpendicular to flow (Van Wychen et al., 2021). Flux gates were subdivided into approximately 25 m segments (hereafter flux gate segments) using a unique orthographic coordinate system for each glacier to minimize the effect of distortion from regional projections. We then used these points to extract values from the velocity and ice thickness datasets.

3.6.3 Frontal ablation estimation

The velocity, ice thickness, and area change measurements were combined to derive mean frontal ablation rates for every glacier in the Northern Hemisphere over the periods 2000-2010 and 2010-2020. We computed the frontal ablation rate (A_f; Gt a^{-1}, defined as positive here) from the ice discharge rate ($\dot{D}_{ice}$, Gt a^{-1}, defined as positive here) across a flux-gate close to the glacier terminus and the mass change rate associated with terminus position change ($\dot{M}_{term}$; Gt a^{-1}; defined positive for retreat and negative for advance):

$$\dot{A}_f = \dot{D}_{ice} + \dot{M}_{term} \quad (3.1)$$

$\dot{D}_{ice}$ is given by:

$$\dot{D}_{ice} = (\rho(\sum_{n=1}^{N}(V_n \cdot H_n \cdot d_n)) - (S_f \cdot \dot{B}_{clim})) \quad (3.2)$$

where ρ is the vertically averaged density of the ice column (900 kg m^{-3}; Cuffey & Paterson, 2010), N is the total number of flux gate segments along the flux gate, V_n is the vertically averaged ice velocity component normal to the flux gate at segment n (assumed to be 95% of the surface velocity at that location; m a^{-1}; Cuffey & Paterson, 2010), H_n is the ice thickness (m), d_n is the flux gate segment width, S_f is the area of the region below the flux gate not involved in terminus retreat or advance (m^2; area shown in Figure 3.7a), and $\dot{B}_{clim}$ is the mean specific climatic mass balance rate (kg m^{-2} a^{-1}; defined as positive here).

We calculated the mass change due to terminus advance or retreat by:

$$\dot{M}_{term} = (\rho \cdot \frac{\Delta S_{term}}{\Delta t} \cdot \overline{H} + \Delta S_{term}/2 \cdot \dot{B}_{clim}) \quad (3.3)$$

where $\overline{H}$ is the mean thickness of the terminus in the area gained or lost (in m) and ΔS_{term} is the area (m^2) of the glacier that is now replaced by the ocean for retreating glaciers, or which occupies previous ocean area for advancing glaciers (division by 2 is necessary to account for the average area over the decade as no area was lost at the start of decade), and is computed from the digitized termini positions in 2000, 2010 and 2020 (Figure 3.7). Δt is the number of years between observations.

3.6.4 Ice surface velocity

Ice surface velocities were primarily derived from Landsat-based, annual displacement mosaics of the Inter-mission Time Series of Land Ice Velocity and Elevation (ITS_LIVE; Figure 3.7D (Gardner et al., 2019) at 240 m resolution (Lei et al., 2021). Data gaps smaller than one pixel were filled from the nearest neighbor. To improve the Greenland Periphery and Russian

Arctic observations, we included MEaSUREs InSAR (Joughin et al., 2018) and Sentinel-1 data (Friedl et al., 2021), respectively, when the signal-to-noise ratio was lower than that of ITS_LIVE. For glaciers with no ITS_LIVE observations, such as those above 82.7°N, we used Landsat or Sentinel-2 imagery from 2016-2020 and AutoRIFT (Gardner et al., 2018) to produce velocity maps. For a small ice cap in the Barents Sea (300 km^2) and a glacier in the De Long Islands (10 km^2), we could not generate reliable velocity results, and thus assumed a 5 ± 5 m a^{-1} velocity based on evidence of little ice motion (i.e. no flow bands). For Svalbard and the Russian Arctic, where the optical velocity record from 2000-2010 was sparse in ITS_LIVE, we filled this gap using 1992-2012 observations from the JERS1, ERS1, ALOS PALSAR, and TerraSAR-X satellites. We used synthetic-aperture radar (SAR) offset-tracking to compute winter velocity from these scenes at 100 m resolution (Paul et al., 2015). We combined all available velocity observations over each decade to derive a mean decadal velocity along the flux gate for each glacier. We do not account for seasonal variability in ice motion due to a lack of data to quantify this variability. In the few instances for which no velocity data was available for the 2000-2010 period (3.9% of flux gates), mean decadal values from 2010-2020 were used to fill the gaps.

3.6.5 Ice thickness

Direct radar-derived measurements, primarily from the Glacier Thickness Database (GlaThiDa) 3.0.3 (GlaThiDa Consortium, 2019), were used to determine ice thickness along the flux gates and over deglaciated areas due to terminus retreat since 2000. For Arctic Canada North, Center for Remote Sensing of Ice Sheets (CReSIS, 2016) radar tomography observations acquired in ~3 km swaths from the 2014 NASA Operation IceBridge mission provided the main ice thickness source. Additional radio-echo sounding observations were incorporated for the

Russian Arctic, where available (Dowdeswell et al., 1996, 2002; Glazovsky et al., 2018; Glazovsky et al., 2018; Macheret et al., 2000; Sochnev et al., 2018; Tarasov et al., 2019). Whereas most of our observations were acquired during the study period, we used 1288 Svalbard thickness measurements in GlaThiDa from 1980 to 1995 and some observations in Russia that were collected in 1994 (Dowdeswell et al., 1996) and 1997 (Dowdeswell et al., 2002). To ensure thickness data are contemporaneous, we used elevation change estimates from Hugonnet et al. (2021) to correct ice thickness at the fluxgate from the time of the measurement or model to 2005 and 2015 for use in ice discharge calculations. Where point thickness observations exist, we averaged all observations within 100 m of each flux gate segment to derive the thickness at that point (Equation 3.2). When only a centerline observation was available, or the thickness observations did not cover the entire length of the flux gate, we assumed a U-shaped valley to determine thickness where no observations are available (Van Wychen et al., 2014):

$$H_n = \frac{10 - H_{center}}{W_1} * {W_2}^2 + H_{center} \quad (3.4)$$

where W_1 (m) is distance from the glacier margin and W_2 (m) is distance from the glacier centerline with thickness H_{center} (m). We use 10 m as a minimum ice thickness on the glacier margins. Similar approaches can be found in Sánchez-Gámez and Navarro (2018). This may not accurately reflect the glacier thickness if the centerline observation is not the deepest point on the glacier, or if the glacier valley is not U-shaped, although we have no way to quantify this.

In all, there is at least one ice thickness observation for 268 glaciers, which together contribute 69% of the total frontal ablation from 2010-2020. Out of these 268 glaciers, 250 have at least a centerline observation (middle 20% of glacier), 161 have at least 75% coverage across the flux gate, and 120 have at least 90% coverage across the flux gate. When no thickness observations were available, data gaps were filled with modeling results from Millan et al.

(2022) (Figure 3.4C). We found that the model results overestimated glacier thickness at the fluxgate, even after accounting for elevation changes with an average 135 m bias between model estimates and observations. We empirically removed this bias by modelling it as a linear function of the glacier thickness to match existing measurements.

For five small glaciers where no modeled thickness data were available, we assigned a similar thickness to that of a morphologically similar nearby glacier. For small glaciers, modeling occasionally produces ice thickness values that are unrealistically small (e.g. less than 5 m average). When the model results suggested that the average ice thickness along the flux gate is less than 30 m, we replaced these values with 30 m and assigned an uncertainty of 20 m (for 144 glaciers during 2000-2010, and 230 glaciers during 2010-2020). For the six marine-terminating glaciers on Jan Mayen we used scarce point measurements (Millan et al., 2022) and flow-law theory (Cuffey & Paterson, 2010) to estimate the thickness.

To determine mean ice thickness $\overline{H}$ (Equation 3.3) over the glacier area that was lost or gained we averaged all available observations. Where no observations were available, we used modelled thickness estimates (debiased in the same way as above) for the terminus area that was gained or lost unless these data were not available, in which case we assumed the thickness to be 60 ± 30% of the mean thickness along the flux gate. On 74 glaciers, primarily in East Greenland, model thickness estimates were unrealistically low (less than 10 m) in an area that was gained or lost, so we replaced those values with 60 ± 30% of the mean thickness along the flux gate.

3.6.6 Glacier terminus front positions

To determine ΔS_{term} (Equation 3.3) for the periods 2000-2010 and 2010-2020, glacier terminus positions were digitized manually for every glacier in approximately 2000, 2010, and

2020, primarily from summer, cloud-free, true-color Landsat 5, 7, and 8 imagery (30 m spatial resolution). When Landsat images were not available, we first attempted to fill the gap with true-color ASTER data (15 m spatial resolution), particularly in northern Greenland and Arctic Canada North for 2000 and 2010. Where no cloud-free optical observations were available, we used Radarsat-1 fine beam mode (2000; 8 m pixel resolution; used in Northern Greenland) and ALOS PALSAR fine beam single polarization (2010; 10 m pixel resolution; used in Arctic Canada North) imagery downloaded from the Alaska Satellite Facility. Mapping was carried out in QGIS version 3.10 in a WGS84 Arctic Polar Stereographic projection (EPSG 3995). To measure the area of each polygon we reprojected the dataset into a unique orthographic projection centered on each glacier to eliminate the impact of distortion.

3.6.7 Climatic mass balance below the flux gate

To account for mass changes unrelated to frontal ablation (e.g. surface melting) between the flux gate and glacier front), we used the Python Glacier Evolution Model (PyGEM) (Rounce et al., 2020) to model the climatic mass balance $\dot{B}_{clim}$ for each glacier. $\dot{B}_{clim}$ is defined as the mass changes due to snow accumulation, and melt at the surface and refreezing of melt and rain water below the surface (Cogley et al., 2011). PyGEM assumes the basal mass balance and internal ablation is negligible. We calibrated PyGEM using geodetic mass balance estimates (Hugonnet et al., 2021). We used monthly ERA5 air temperature and precipitation data (Hersbach et al., 2020) to compute glacier melt with a degree-day model, accumulation with a temperature threshold, and refreezing from annual air temperature. We extracted $\dot{B}_{clim}$ for the lowest two 10-m elevation bins of each glacier. The glacier area was assumed constant in PyGEM. For two well-investigated glaciers with high frontal ablation rates we used estimates of

climatic balance from direct observations: Columbia Glacier, Alaska (8 ± 2 m water equivalent) (Rasmussen et al., 2011), and for Basins 2 and 3 of Austfonna, Svalbard (-0.6 ± 0.3 m water equivalent) (Hagen et al., 2003; Schuler et al., 2020). For glaciers lacking appropriate input data (7 small glaciers), we used regional (defined by RGI primary regions) averages of the climatic mass balance.

For 490 glaciers from 2000-2010 and 602 glaciers from 2010-2020 the absolute $\dot{B}_{clim}$ was greater than the ice discharge, which is physically impossible. For 369 (2000-2010) and 406 (2010-2020) of these glaciers, we increased the average discharge and reduced the average climatic balance within uncertainties to constrain each variable to real-world possibilities. For the remaining glaciers, we used ice discharge values neglecting $\dot{B}_{clim}$, but with 100% uncertainty. These 488 and 601 glaciers only made up 0.70 ± 0.44 Gt a^{-1} (2000-2010) and 0.54 ± 0.46 Gt a^{-1} (2010-2020) of ice discharge, accounting for 2% of total ice discharge during both time periods.

3.6.8 Surge-type glaciers and instabilities

We individually examined glaciers that exhibited a terminus advance from 2000-2010 and/or 2010-2020 to determine if the advance was due to a dynamic instability such as pulsing or surging. We classified the glaciers according to the RGI classification scale (0: no evidence, 1: possible, 2: probable, 3: observed) based on glacier morphology (including tear-drop moraines, pothole fields, crevasse patterns; Jiskoot, 2011) viewed from satellite imagery and literature where available (Clarke et al., 1986; Copland et al., 2003; Dowdeswell & Williams, 1997; Grant et al., 2009; Jiskoot et al., 2003; Sevestre & Benn, 2015).

For the Nathorstbreen system and an outlet of the Leningradskiy Ice Cap, our measured discharge was greater than terminus mass gain. However, we adjusted these totals within their uncertainties to make physical sense. For six glaciers from 2000-2010 and one from 2010-2020 the discharge was less than the terminus change; however, in each instance the mass held in terminus advance was less than 0.02 Gt a^{-1}, so we artificially increased discharge to be within the uncertainty of terminus change while assigning 100% uncertainty to the discharge. These adjusted glaciers accounted for a total frontal ablation of 0.02 Gt a^{-1}.

3.6.9 Sea-level rise calculations

We estimated the sea-level equivalent of frontal ablation assuming a global ocean area (Cogley et al., 2011) of 362.5 x 10^6 km^2. To account for mass changes below sea level that do not contribute to sea-level change as the ice displaces ocean volume, we subtracted the mass losses due to retreat below sea-level or add the gains due to advance. Since the ice fraction of total ice thickness below sea level is unknown, we calculate a higher bound scenario (assuming a fraction of 90% which corresponds to ice close to flotation) and a best estimate lower-bound scenario (50%).

3.6.10 Uncertainty in frontal ablation estimates

We estimate the uncertainty in ice discharge $\sigma_{\dot{D}}$ assuming each uncertainty component (Equation 3.2) is independent, which yields:

$$\sigma_{\dot{D}}{}^2 = \rho_{ice} \sum_n \left(\sqrt{\left(\frac{\sigma_{V_n}}{V_n}\right)^2 + \left(\frac{\sigma_{H_n}}{H_n}\right)^2 + \left(\frac{\sigma_{d_n}}{d_n}\right)^2} \cdot V_n H_n d_n \right)^2 + \left(S_f \sigma_{\dot{B}_{clim}}\right)^2 + \left(\sigma_{S_f} \dot{B}_{clim}\right)^2 \quad (3.5)$$

where σ_{V_n} is the uncertainty in vertically integrated velocity (assumed to be 95% of the surface velocity at that location; Cuffey & Paterson, 2010), σ_{H_n} is the uncertainty in ice thickness, σ_{d_n} is the fluxgate width uncertainty, all associated to the flux gate point n. At the glacier-scale, $\sigma_{\dot{B}_{clim}}$ is the uncertainty in climatic specific-mass balance, and σ_{S_f} is the uncertainty in the area below the flux gate. Similarly, we estimate the uncertainty in terminus mass change $\sigma_{\dot{M}_{term}}$ assuming each uncertainty component (Equation 3.3) is independent, which yields:

$$\sigma_{\dot{M}_{term}}{}^2 = \left(\sigma_{\Delta S_{term}} \underline{H}\right)^2 + \left(\sigma_{\underline{H}}\, \Delta S_{term}\right)^2 + \left(\sigma_{\dot{B}_{clim}} \frac{\Delta S_{term}}{2}\right)^2 + \left(\dot{B}_{clim} \frac{\sigma_{\Delta S_{term}}}{2}\right)^2 \quad (3.6)$$

where $\sigma_{\Delta S_{term}}$ is the uncertainty in the terminus area change and $\sigma_{\underline{H}}$ is the uncertainty in the mean thickness over ΔS_{term}. Finally, the uncertainty in frontal ablation $\sigma_{\dot{A}}$ is estimated by considering the ice discharge and terminus mass change uncertainties (Equation 3.1) as independent:

$$\sigma_{\dot{A}}{}^2 = \sigma_{\dot{D}}{}^2 + \sigma_{\dot{M}}{}^2 \quad (3.7)$$

3.6.11 Uncertainty sources at flux gate point or glacier-scale

We relied on the uncertainties reported by each dataset, whether at the scale of a flux gate point, flux gate, or glacier to propagate the uncertainties through Equations 3.5 and 3.6.

At flux gate points, we found good agreement (<50% difference) between the average velocity uncertainties σ_{V_n} reported in ITS_LIVE and the average dispersion between the ITS_LIVE and MEaSURES estimates at the same flux gates. We found a similar agreement (<30% difference) between measured and modelled ice thicknesses (Millan et al., 2022), after accounting for elevation changes (Hugonnet et al., 2021) and debiasing. The SAR-derived velocity uncertainties average 10 m a^{-1} for TerraSAR-X and ALOS PALSAR (Paul et al., 2015), 20 m a^{-1} for JERS-1

(Strozzi et al., 2008), and 40 m a^{-1} for ERS (Dowdeswell et al., 2008). We derived the uncertainty in flow direction based on the stated uncertainties in the x and y velocity products, translated into a flux gate segment width uncertainty σ_{d_n}. When these data were unavailable, we assumed a 10° uncertainty in flow direction.

Unless otherwise reported, we assumed a 10% uncertainty in ice thickness σ_{H_n}. We also assumed a 10% uncertainty for ice thicknesses derived from U-shaped valley-based modeling from a centerline depth measurement (Van Wychen et al., 2014). When a model depth or thickness observation in the terminus region was not available to calculate terminus mass change, we assumed that the average thickness of the area gained or lost is 60 ± 30% of the average flux gate thickness.

The uncertainty in area gained or lost σ_{S_f} was assumed to be one pixel and derived by multiplying the length of the perimeter of the changed terminus area by the width of a pixel (30 m for Landsat and 15 m for ASTER) (Krumwiede et al., 2014).

We estimated the uncertainty in the climatic specific-mass balance from the median absolute deviation of 50 simulations from Bayesian calibration of model parameters (Rounce et al., 2020) forced with ERA5 air temperature and precipitation (Hersbach et al., 2020) calibrated on 2000-2019 glacier mass balances (Hugonnet et al., 2021) for each glacier. We assumed the uncertainties in climatic mass balance are independent between glaciers.

3.6.12 Spatial correlations in ice thickness and velocity uncertainties

We quantified the spatial correlation of velocity and ice thickness uncertainties (Figure 3.8) by estimating global-scale, empirical variograms (Mälicke & Schneider, 2019; Matheron, 1965) using the difference between independent sources of estimates at the same flux gates. We

performed the spatial correlation analysis at distances covering several orders of magnitude (from 25 m to 1000 km), thereby accounting for biases at glacier and regional scales through long-range correlations (Hugonnet et al., 2021).

We compared ITS_LIVE and MEaSUREs velocity observations in Greenland (Figure 3.9) and found fully correlated (100%) variance at short distances (<50 m), and correlated variances at 40-100% within ~700 m. We attribute these short-range correlations to the resolution of optical imagery and image-matching. Velocity estimates remain correlated at 15-40% within 25 km and 0-15% within 1000 km, highlighting moderate glacier and regional scale errors due to seasonal differences when estimating yearly velocity. Beyond 1000 km, the velocity estimates are fully decorrelated.

We compared all available ice thickness measurements to debiased model estimates (Millan et al., 2022) (Figure 3.10). Ice thickness variance was correlated at 80-100% within 2 km, the result of short-scale modelling artefacts. Ice thickness variance remains correlated between 50-80% within 150 km, and between 0-50% within 1000 km, implying large-scale biases in modelled ice thicknesses that are likely due to the temporal inconsistency of glacier outlines. After 1000 km, ice thickness estimates are fully decorrelated.

3.6.13 Uncertainty propagation from pixel to glacier and regional scales

For the ice discharge uncertainty (Equation 3.5), we independently considered the ice discharge at the flux gate $\dot{D}_{gate}$ based on velocity and ice thickness estimates (Equation 3.1):

$$\dot{D}_{gate} = \sum_n \dot{D}_n = \sum_n \rho_{ice} V_n H_n d_n \quad (3.8)$$

We propagated the uncertainties in ice discharge at the flux gate from flux gates n to glaciers, and then repeated the same approach from glacier to region, accounting for spatial

correlations in velocity and ice thickness uncertainties (Hugonnet et al., 2021; Webster & Oliver, 2008):

$$\sigma_{\dot{D}_{gate}}{}^2 = \sum_n^N \sigma_{\dot{D}_n}{}^2 + \sum_n^N \sum_{n \neq m}^N C_{\dot{D}}(l_{n-m})\, \sigma_{\dot{D}_n} \sigma_{\dot{D}_m} \quad (3.9)$$

where $C_{\dot{D}}(l)$ is the spatial correlation in ice discharge at the spatial lag l, and l_{n-m} is the distance between flux gates n and m in the glacier, or between glacier n and m in the region. The correlation in ice discharge $C_{\dot{D}}(l)$, ranging from 0 to 1, is estimated either for each glacier or region based on the velocity and ice thickness empirical variograms (Figure 3.9 and 3.10).

For the terminus mass change uncertainty, we applied a similar approach to propagate the uncertainty in average ice thickness over the area gained or lost $\sigma_{\underline{H}}$, based solely on the ice thickness variogram (Figure 3.10)

Table 3.1. Frontal ablation and components. Decadal mean mass losses (± uncertainties) by region (from west to east) for all Northern Hemisphere marine-terminating glaciers, due to advance or retreat of terminus position (terminus mass change), ice flow through a terminus flux gate (ice discharge), and the sum of these (frontal ablation).

	Frontal ablation (Gt a^{-1})		Ice discharge (Gt a^{-1})		Terminus mass change (Gt a^{-1})		Length of flux gates	
	2000-2010	2010-2020	2000-2010	2010-2020	2000-2010	2010-2020	(km)	Number of glaciers in 2000
Alaska	11.36 ± 0.43	10.47 ± 0.34	11.26 ± 0.39	9.58 ± 0.20	-0.10 ± 0.17	-0.89 ± 0.28	80	42
Arctic Canada N	4.13 ± 1.18	4.26 ± 1.19	2.68 ± 0.75	2.23 ± 0.37	-1.45 ± 0.91	-2.03 ± 1.14	522	252
Arctic Canada S	0.09 ± 0.07	0.09 ± 0.08	0.04 ± 0.03	0.03 ± 0.02	-0.05 ± 0.07	-0.06 ± 0.07	38	86
Greenland periphery	4.35 ± 1.60	3.21 ± 1.10	2.3 ± 0.85	1.91 ± 0.46	-2.06 ± 1.36	-1.30 ± 1.00	750	537
Iceland	0.11 ± 0.12	0.04 ± 0.09	0.11 ± 0.12	0.02 ± 0.08	-0.00 ± 0.02	-0.03 ± 0.05	5	1
Svalbard and Jan Mayen	8.64 ± 3.36	17.02 ± 2.55	5.91 ± 2.86	14.62 ± 1.21	-2.73 ± 1.77	-2.40 ± 2.25	766	166
Russia: Franz Josef Land	13.11 ± 6.90	8.19 ± 3.69	11.43 ± 6.67	5.43 ± 2.77	-1.68 ± 1.76	-2.75 ± 2.44	1747	328
Russia: Novaya Zemlya	2.68 ± 1.17	4.16 ± 0.96	2.03 ± 1.02	3.15 ± 0.43	-0.65 ± 0.57	-1.00 ± 0.86	196	39
Russia: Severnaya Zemlya	4.51 ± 1.48	5.72 ± 0.95	4.15 ± 1.41	4.62 ± 0.7	-0.36 ± 0.43	-1.10 ± 0.64	349	45
Total	48.98 ± 8.16	53.15 ± 4.97	39.91 ± 7.56	41.59 ± 3.19	-9.07 ± 3.07	-11.56 ± 3.81	4454	1496

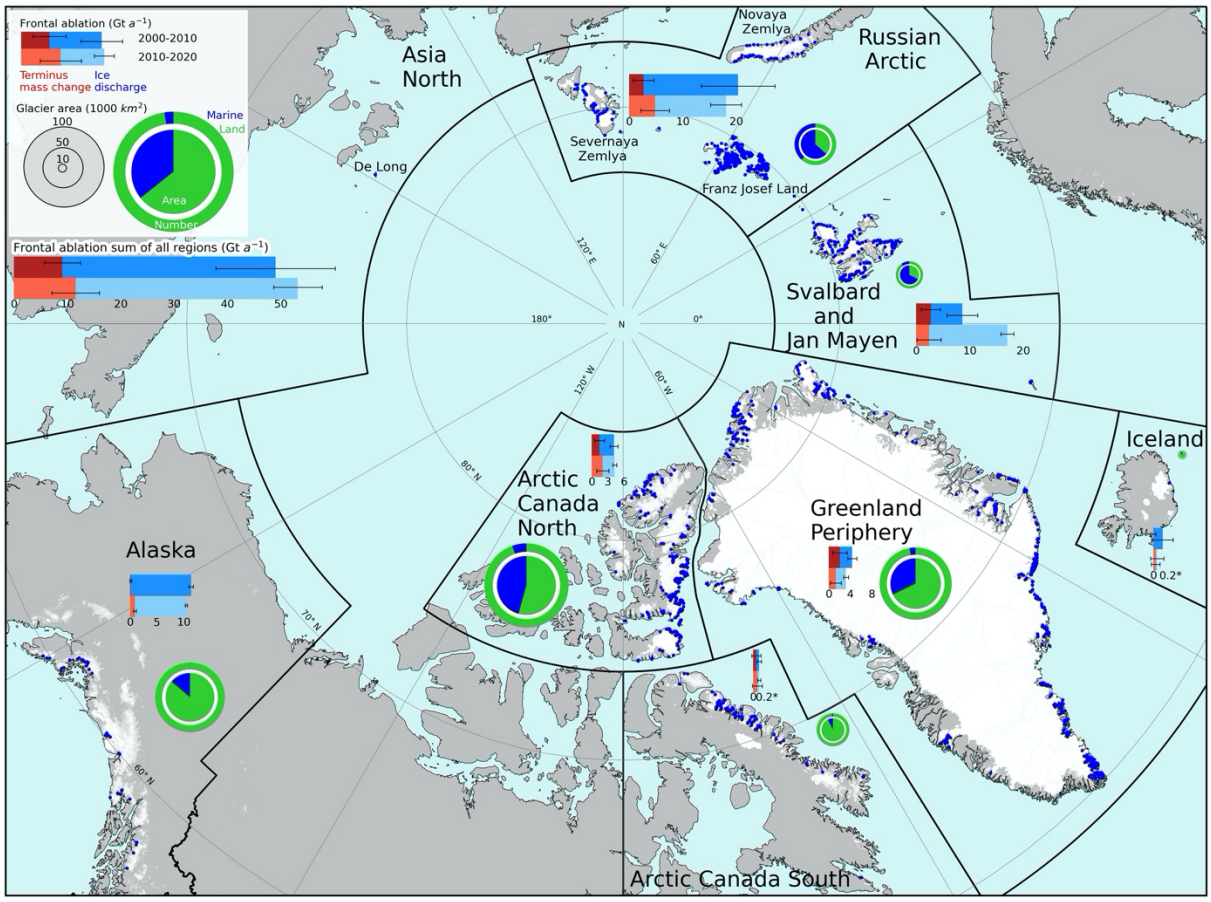


Figure 3.1 Regional frontal ablation of marine-terminating glaciers. Bar charts show the decadal-mean frontal ablation rates by Northern Hemisphere region from 2000-2020 and are divided into ice discharge and terminus mass change (uncertainties are black lines). Pie charts show the proportion of marine vs. land terminating glaciers for each region. The Northern Hemisphere glacier proportions are shown in the legend.

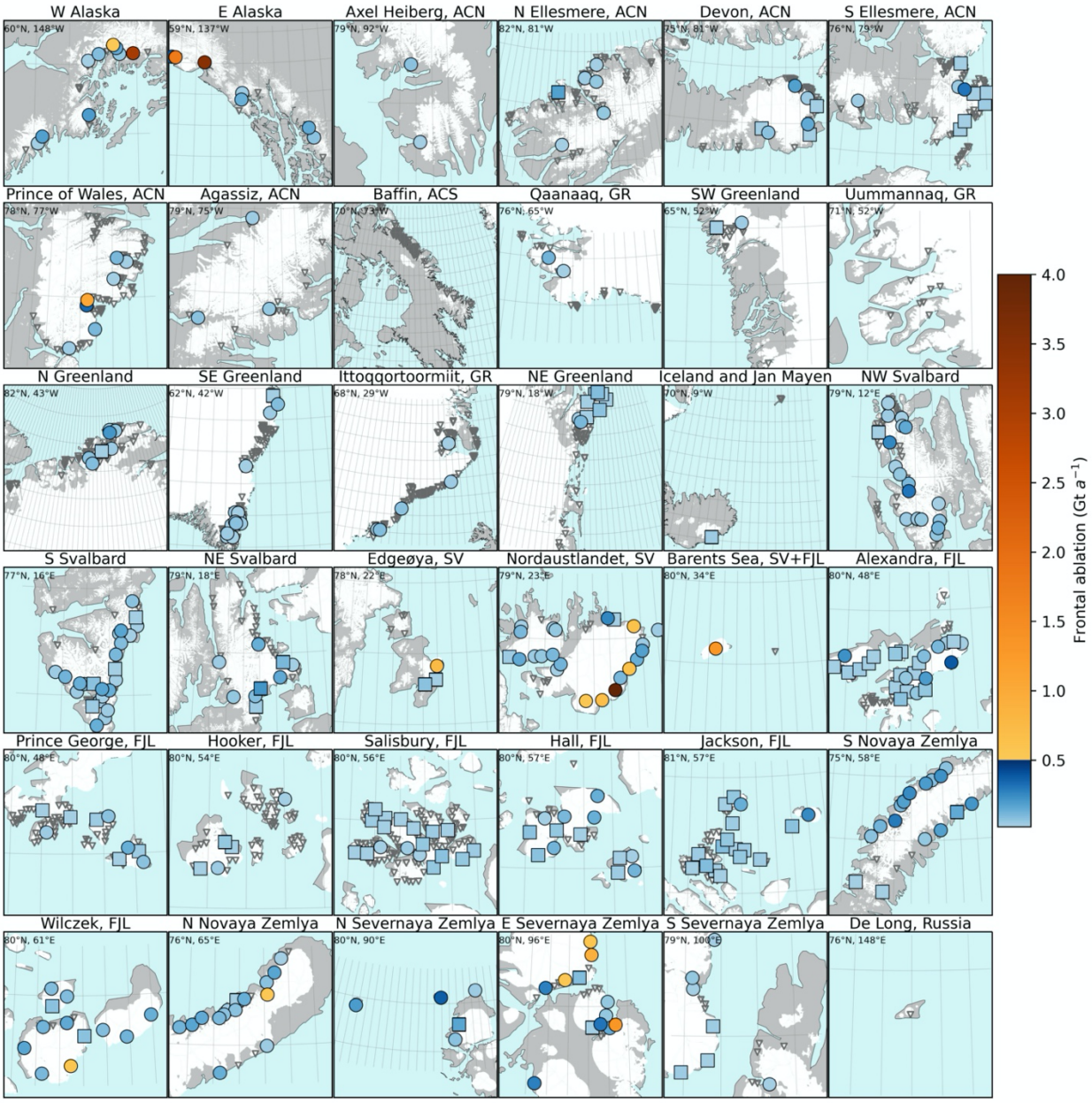


Figure 3.2 Mean frontal ablation rate by glacier for 2010-2020. Dark gray triangles indicate glaciers that have a frontal ablation less than 0.02 Gt a^{-1} (not shown in color bar) and squares indicate glaciers where the uncertainty is more than 50% of total frontal ablation. Glacierized area is marked in white. Latitude and longitude in top left of each panel indicate the center point of that panel and the grid is 1° by 1° for all panels, with 1 degree of latitude equal to 111 km. The only glacier off the color bar scale is Basin-3 of Austfonna (6.18 Gt a^{-1}; Nordaustlandet). For uncertainties see Figure 3.5. Frontal ablation for 2000-2010 is shown in Figure 3.3. Abbreviations: ACN is Arctic Canada North, ACS is Arctic Canada South, GR is Greenland Periphery, SV is Svalbard, FJL is Franz Josef Land, NZ is Novaya Zemlya, SZ is Severnaya Zemlya; other abbreviations are cardinal directions.

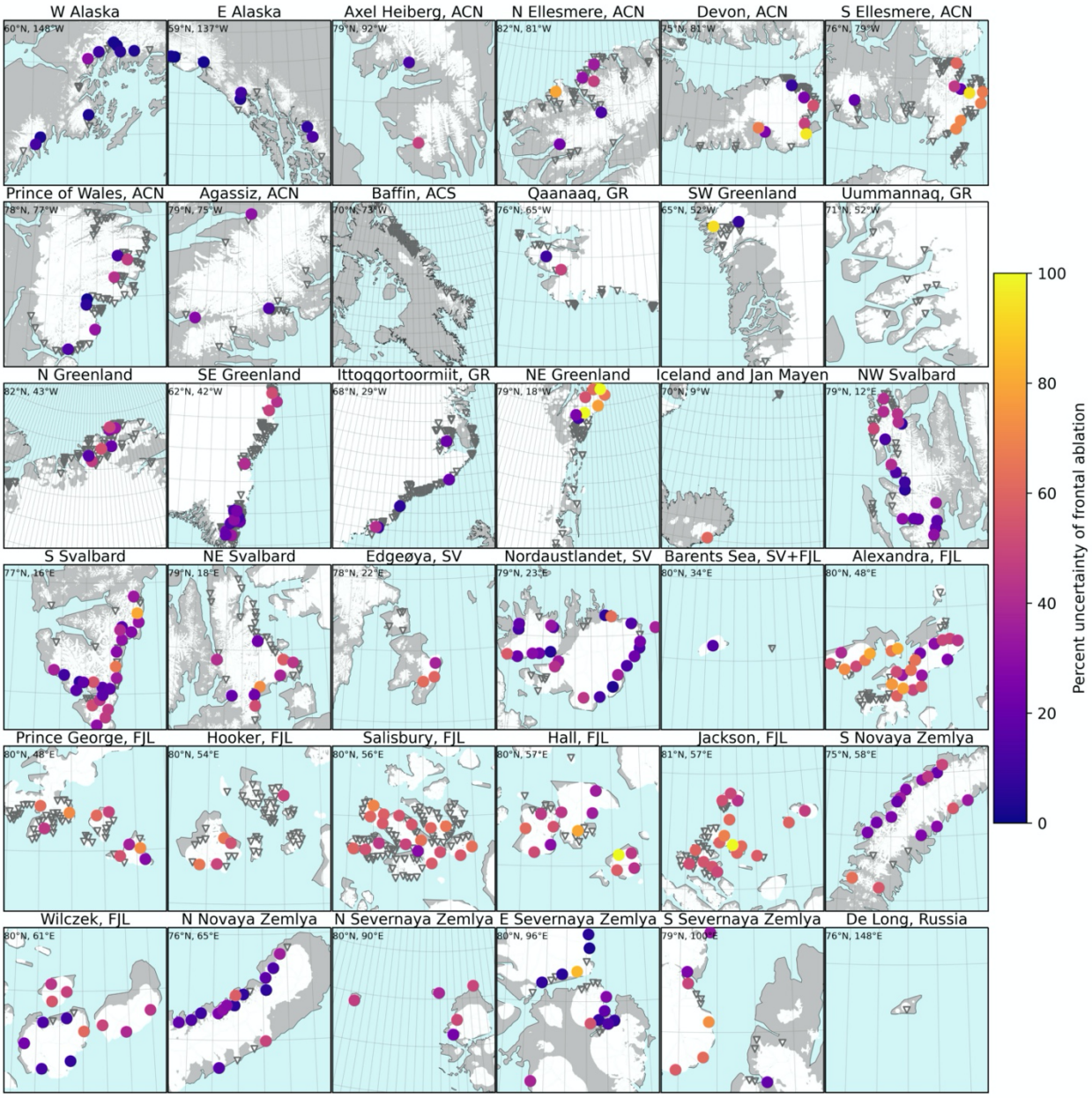


Figure 3.3 Frontal ablation uncertainties by glacier for 2010-2020. Colored dots correspond to the uncertainty of the frontal ablation calculation from 0% (cool colors) to 100% (warm colors) of the total shown in Figure 3.2. Grey triangles indicate glaciers that have a frontal ablation of less than 0.02 Gt a^{-1}. Grid is 1° by 1° for all subplots and the coordinates in the top left of each subplot shows the center latitude and longitude of that subplot. Abbreviations: ACN is Arctic Canada North, ACS is Arctic Canada South, GR is Greenland Periphery, SV is Svalbard, FJL is Franz Josef Land, NZ is Novaya Zemlya, SZ is Severnaya Zemlya; other abbreviations are cardinal directions.

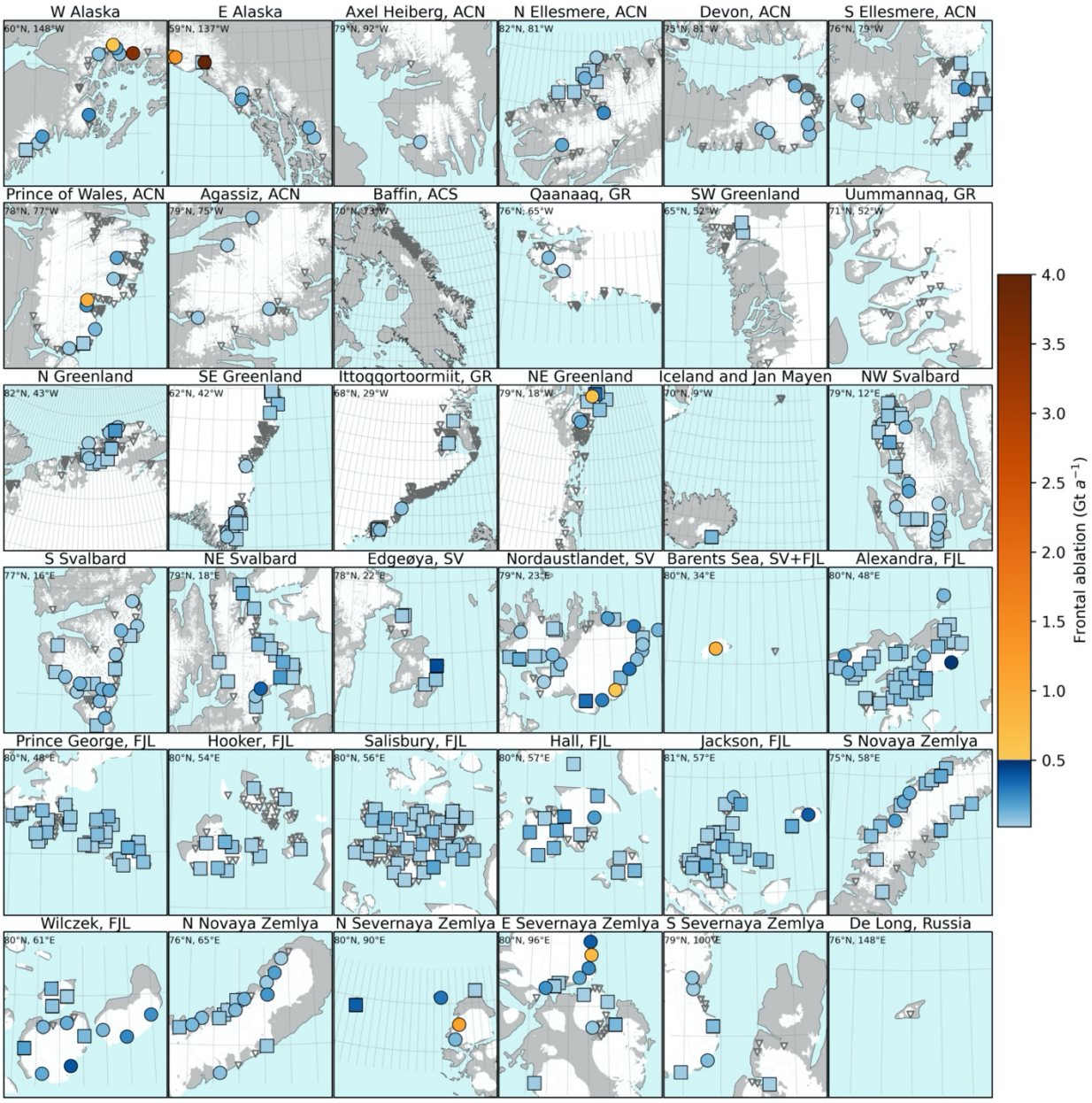


Figure 3.4 Frontal ablation by glacier for 2000-2010. Dark gray triangles indicate glaciers that have a frontal ablation less than 0.02 Gt a^{-1} (not shown in color bar) and squares indicate glaciers where the uncertainty is more than 50% of total frontal ablation. Glacierized area is marked in white. Latitude and longitude in top left of each panel indicate the center point of that panel and the grid is 1° by 1° for all panels, with 1 degree of latitude equal to 111 km. The only glacier off the color bar scale is Hubbard Glacier (4.05 Gt a^{-1}; E Alaska). For uncertainties see Figure 3.5. Abbreviations: ACN is Arctic Canada North, ACS is Arctic Canada South, GR is Greenland Periphery, SV is Svalbard, FJL is Franz Josef Land, NZ is Novaya Zemlya, SZ is Severnaya Zemlya; other abbreviations are cardinal directions.

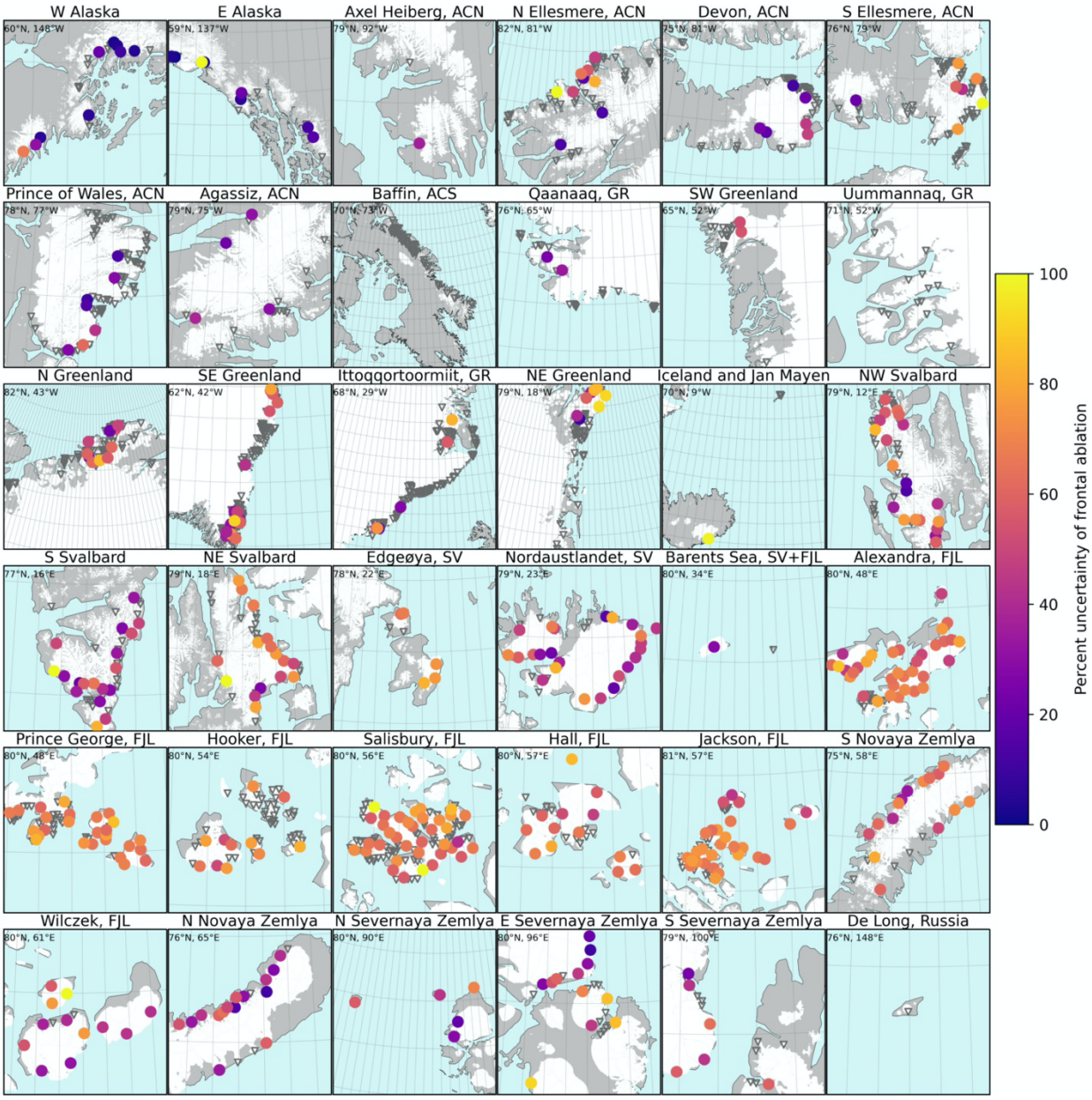


Figure 3.5 Frontal ablation uncertainties by glacier for 2000-2010. Colored dots correspond to the uncertainty of the frontal ablation calculation from 0% (cool colors) to 100% (warm colors) of the total shown in Figure 3.4. Grey triangles indicate glaciers that have a frontal ablation of less than 0.02 Gt a^{-1}. Grid is 1° by 1° for all subplots and the coordinates in the top left of each subplot shows the center latitude and longitude of that subplot. Abbreviations: ACN is Arctic Canada North, ACS is Arctic Canada South, GR is Greenland Periphery, SV is Svalbard, FJL is Franz Josef Land, NZ is Novaya Zemlya, SZ is Severnaya Zemlya; other abbreviations are cardinal directions.

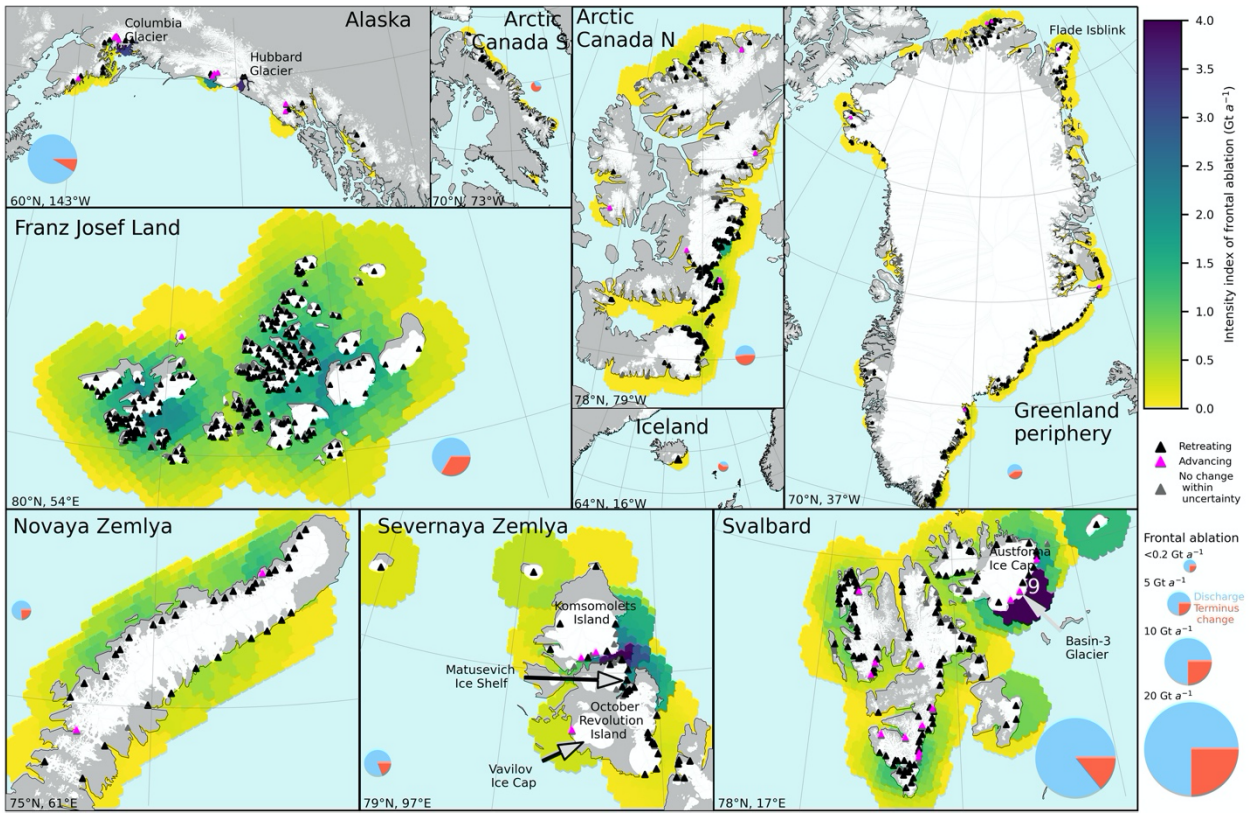


Figure 3.6 Intensity index of frontal ablation in near-coastal ocean environments 2010-2020. The index is defined as the sum of the frontal ablation rates of all glaciers within 50 km of their terminus, based on a 10 km ocean grid. Text in white indicates values above 4.5 Gt a^{-1}. The pie charts show the proportion of ice discharge (blue) and terminus change (red) to total frontal ablation for each region, and are scaled to frontal ablation for that region. Glacier-covered area is shown in white, ocean in light blue, and other land surfaces in grey. Individual glaciers or ice caps mentioned in the text are named. The grid shows lines of latitude every 10° and longitude every 5°, or 1106 km between lines of latitude for all panels. The coordinates in the bottom left of each box show the center latitude and longitude.

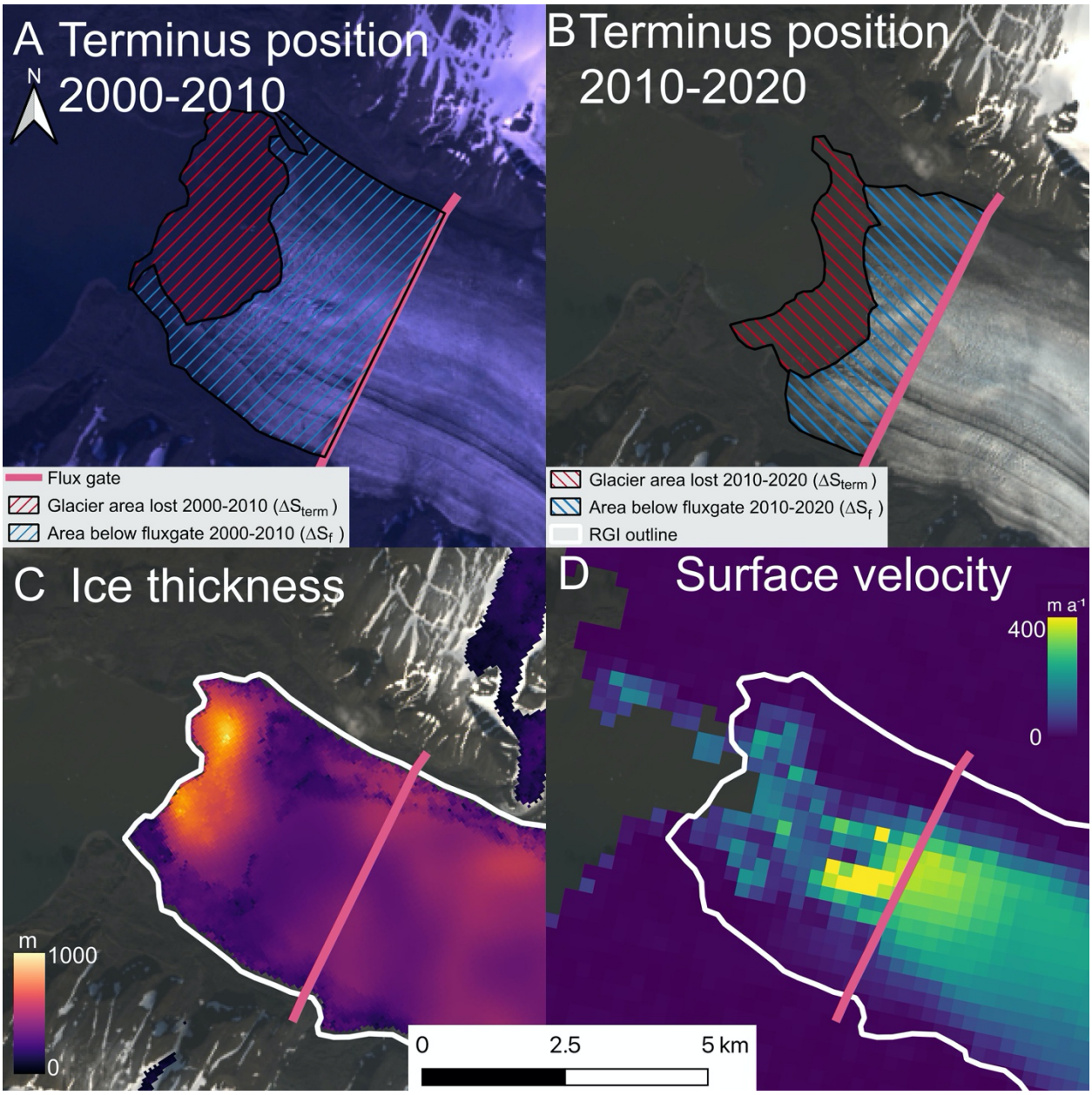


Figure 3.7 Data sets used to compute frontal ablation exemplified for a glacier on Novaya Zemlya, Russia (75.2°N, 57.1°E). A) Glacier termini positions and glacier area lost by retreat or gained by advance (red hatching, ΔS_{term} in Equation 3.3) and area not involved in retreat/advance below the fluxgate (blue hatching, S_f in Equation 3.2) for 2000-2010. B) Same as Figure 3.7A except for 2010-2020. C) Glacier thickness distribution derived from model data generated by Millan et al. (2022). D) Surface velocity data for 2018 from ITS_LIVE (Gardner et al., 2019). Thickness (H_n) and velocity (V_n) data along the flux gate are used in Equation 3.2. Thickness data averaged over the most extended glacier terminus position during the considered period ($\overline{H}$) is used in Equation 3.3.

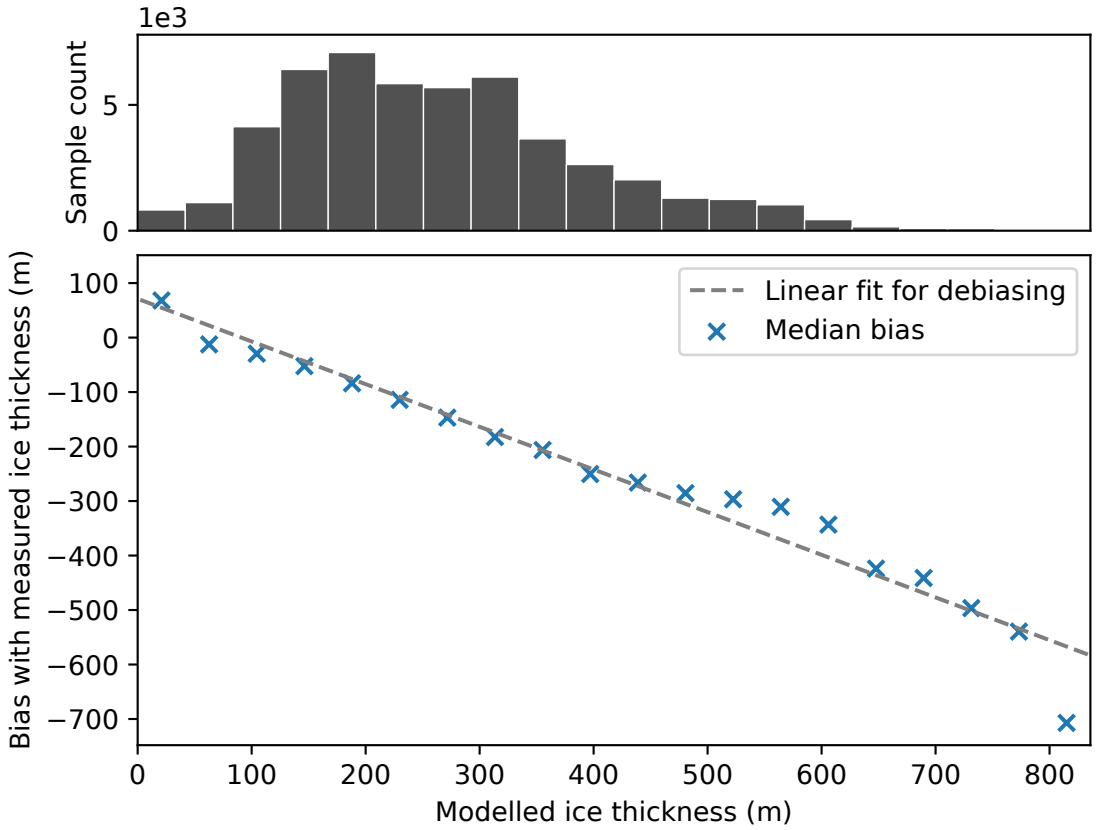


Figure 3.8 Debiasing of modelled ice thickness estimates. Bias between modelled and measured ice thicknesses after adjustment of surface elevations to 2005 (for 2000-2010 period) or 2015 (for 2000-2020 period) to account for geodetic mass balance. The bias is empirically estimated by binning the difference of measurement and model estimates within 20 intervals (every 40 m) of modelled ice thickness. The sample count of each bin represents the number of flux gate points where measured and modelled ice thickness were compared. The bias dependency to modelled ice thickness is constrained by a linear function optimized by least-squares. The bias is later removed by subtracting the value of this function at each location.

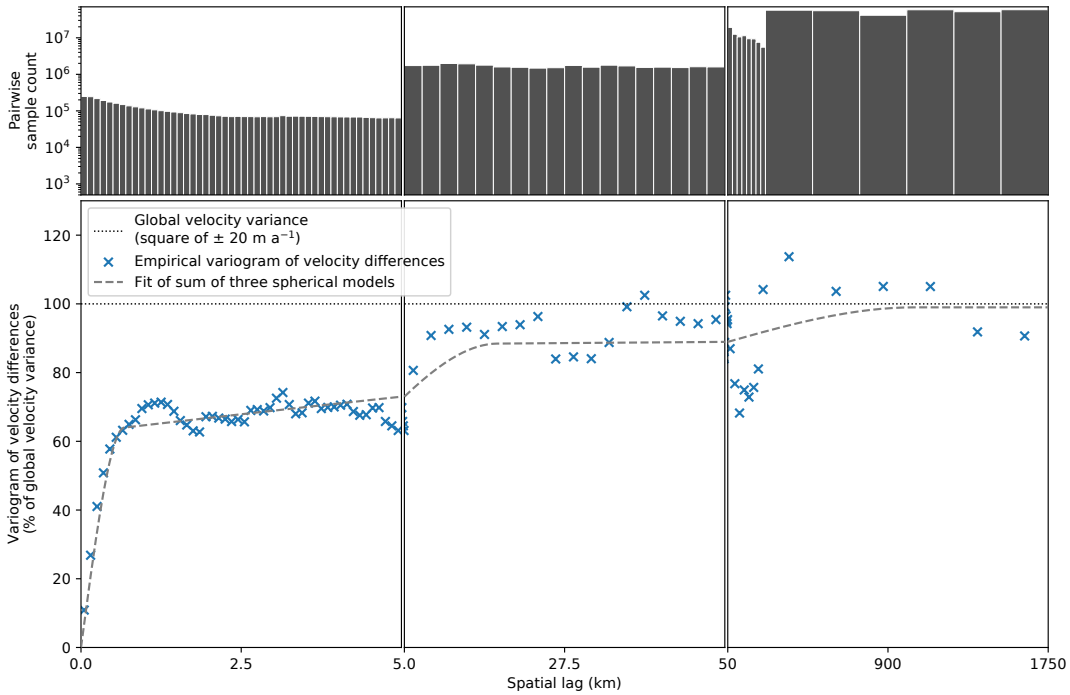


Figure 3.9 Spatial correlation of velocity estimates. Empirical and modelled variogram of velocity estimates, expressed as a percentage of the global velocity variance. The empirical variogram is estimated from the differences between ITS_LIVE and MEaSUREs velocities in Greenland compared at the same locations and for the same yearly periods. The sample count describes the number of pairwise flux gate comparisons used to estimate the variogram at each spatial lag (i.e. distance between observations). The modelled variogram is a sum of three spherical models optimized by least-squares. The first spherical model with range (correlation length) of 0.7 km has a partial sill (correlated variance) of 63% of the global velocity variance, the second model with range 18 km of 26% of the variance, and the third model with range 1,040 km of 11% of the variance. The spatial correlation of velocity is deduced by subtracting the modelled variogram to the global variance and used to propagate uncertainties from pixel to larger scales in ice discharge estimates.

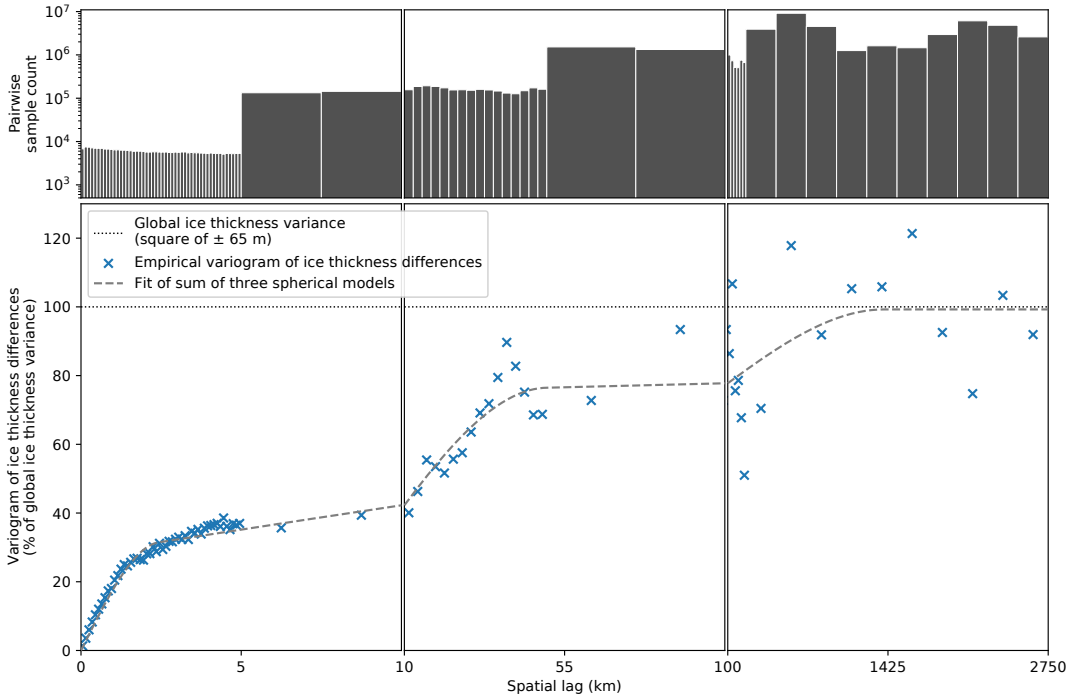


Figure 3.10 Spatial correlation of ice thickness estimates. Empirical and modelled variogram of ice thickness estimates, expressed as a percentage of the global ice thickness variance. The empirical variogram is estimated from the differences between measured and de-biased modelled ice thicknesses compared at the same locations and adjusted to the same year with elevation changes. The sample count describes the number of pairwise flux gate comparisons used to estimate the variogram at each spatial lag (i.e. distance between observations). The modelled variogram is a sum of three spherical models optimized by least-squares. The first spherical model with range (correlation length) of 2 km has a partial sill (correlated variance) of 27% of the global ice thickness variance, the second model with range 47 km of 50% of the variance, and the third model with range 1,404 km of 23% of the variance. The spatial correlation of ice thickness is deduced by subtracting the modelled variogram to the global variance, and used to propagate uncertainties from pixel to larger scales in both ice discharge and terminus mass change estimates.

Chapter 4: Closing Greenland's mass balance: frontal ablation for every Greenlandic glacier from 2000 to 2020

4.1 Introduction

Greenland is likely to contribute the most to sea level rise from any ice mass by 2100 with projected contributions of between 32 and 90 mm, depending on future development pathways (Goelzer et al., 2020). The Greenland Ice Sheet and periphery glaciers (hereafter Greenland) have already contributed 0.35 mm a^{-1} (very likely range of 0.23 to 0.46 mm a^{-1}) to sea level from 1901 to 2018, for a total of 40.4 mm (IPCC, 2021). Mass balance is comprised of two components: climatic-basal mass balance and frontal ablation (Cogley et al., 2011). Climatic-basal mass balance includes accumulation and ablation occurring at the glacier surface, within the glacier, and at the bed (Cogley et al., 2011), which for land terminating glaciers is the entire mass balance. For lake and marine-terminating glaciers, frontal ablation is the process of mass loss at a typically near-vertical glacier margin (i.e. terminus) including calving, subaerial melting, subaerial sublimation, and subaqueous melting (Cogley et al., 2011), and must be added to the climatic-basal balance to determine the total mass balance. The climatic mass balance for Greenland has been calculated by several studies (Fettweis et al., 2020; Noël et al., 2018), but frontal ablation has only been computed for Greenland peripheral glaciers (Recinos et al., 2021; Chapter 3). Ice discharge is the closest approximation of frontal ablation, but excludes ice volume change due to terminus retreat or advance.

Current estimates of Greenland Ice Sheet discharge include 487 ± 49 Gt a^{-1} for 2010 to 2017 (Mankoff et al., 2020) and ~490 Gt a^{-1} from 2006-2016 (King et al., 2018). However, these and other estimates are incomplete as they only include the larger, faster glaciers (King et al., 2020; Mankoff et al., 2020; Mouginot et al., 2019; Wood et al., 2021), excluding at least dozens

of small outlets, and do not account for periphery glaciers. They also include melt below the fluxgate, which should not be considered in frontal ablation estimates (Cogley et al., 2011).

The mass balance of the Greenland Ice Sheet has been increasingly negative since the 1980s. From 2010 to 2018 the Greenland Ice Sheet lost 285 ± 20 Gt a^{-1} (Mouginot et al., 2019). From 1992 to 2018 the contributions of meltwater runoff and ice discharge were approximately equal (Shepherd et al., 2020). However, these studies use ice discharge to approximate frontal ablation, which does not fully account for mass changes.

Greenland marine-terminating glaciers lost 5331.9 ± 24.3 km^2 at the ice-ocean interface from 2000 to 2020 (Kochtitzky & Copland, 2022; Chapter 2). Of the 745 glaciers that ended in the ocean in 2000, 556 retreated and eight advanced through 2020, with three ice sheet outlets and 71 peripheral glaciers no longer ending in the ocean by 2020 (Kochtitzky & Copland, 2022). The retreat of glaciers in Greenland has typically been accompanied by an increase in discharge and loss of mass from those glaciers (King et al., 2020).

Frontal ablation includes both ice discharge (i.e. flow of ice through a fluxgate) and terminus volume change (e.g. volume loss due to retreat). Calculating frontal ablation is challenging because glacier termini frequently advance and retreat, necessitating having a fluxgate up-glacier from the calving margin and accounting for terminus volume change. Thus, in addition to ice discharge, we need to account (by removing) for subaerial melting below the fluxgate and terminus position changes. Here, we use a suite of model and remote sensing datasets to calculate the frontal ablation for every glacier in Greenland, regardless of size, velocity, or connectivity to the ice sheet, for 2000-2010 and 2010-2020.

4.2 Results

There were a total of 213 ice sheet outlets and 537 peripheral glaciers in Greenland in the year 2000, compared to 210 and 465, respectively, in 2020 (Figure 1). We find a total frontal ablation of 481.8 ± 12.0 Gt a^{-1} for 2000-2010 and 510.2 ± 11.5 Gt a^{-1} for 2010-2020 (Table 1). Discharge made up ~90% of this total during 2000-2010 and 2010-2020, while terminus volume change comprised the remainder (Figure 2). The increase in frontal ablation between the two decades was entirely due to an increase in discharge from 434.5 ± 10.6 to 468.1 ± 7.7 Gt a^{-1}. Meanwhile, terminus volume loss underwent a slight reduction from 46.1 ± 5.8 Gt a^{-1} in 2000-2010 to 41.3 ± 5.3 Gt a^{-1} from 2010-2020, although the error limits for these periods overlap.

Nearly all frontal ablation in Greenland comes from ice sheet outlet glaciers. The periphery glaciers made up 1.2% and 0.6% of frontal ablation during 2000-2010 and 2010-2020, respectively. The Greenland Ice Sheet alone had a frontal ablation rate of 475.9 ± 15.9 Gt a^{-1} and 507.0 ± 11.5 Gt a^{-1} during 2000-2010 and 2010-2020, respectively, while periphery glacier frontal ablation decreased from 5.9 ± 3.8 Gt a^{-1} to 3.3 ± 2.4 Gt a^{-1} between these periods.

Sermeq Kujalleq (Jakobshavn Isbræ) had the largest frontal ablation rate during both decades of 36.3 ± 0.8 Gt a^{-1} and 42.3 ± 0.5 Gt a^{-1} during 2000-2010 and 2010-2020, respectively, with 94% and 99% coming from ice discharge (Figure 2). The same nine out of the top 10 glaciers accounted for the highest frontal ablation rates during both decades: Sermeq Kujalleq, Helheim Gletsjer, Kangerlussuaq Gletsjer, Zachariae Isstrøm, Køge Bugt, Kangilliup Sermia (Rink Isbræ), Tuttulikassaap Sermia (Hayes) & Kjer Gletsjer, Petermann Gletsjer, and Nioghalvfjerdsfjorden (Figure 1). Rounding out the top 10 in 2000-2010 was Nuussuup Sermia (Kong Oscar Gletsjer, and in 2010-2020 it was Sermeq (Upernavik Isstrøm) North.

These top 10 glaciers in each decade comprised ~40.0% of total frontal ablation. Just 17 outlets from 2000-2010 and 16 outlets from 2010-2020 made up just over 50% of total frontal ablation. This list includes all 11 glaciers mentioned in the previous paragraph, as well as Alison, Sermeq (Upernavik Isstrøm) South, Daugaard-Jensen Gletsjer, Sermersuaq (Humboldt Gletsjer), and Sermeq Kujalleq (Store Gletsjer). The one glacier included in the top 50% for 2000-2010, but not for 2010-2020, is an unnamed glacier in southeast Greenland (67.60°N, 33.45°W).

Zachariae Isstrøm drains a large portion of northeast Greenland and is one of the top four glaciers during both decades in terms of total frontal ablation. This outlet lost more than twice the terminus volume of any other glacier in Greenland over the study period, and alone accounted for 24% of total Greenland terminus volume loss from 2000-2010, and 35% from 2010-2020. Zachariae Isstrøm was also in the top six glaciers during both decades in terms of ice discharge. It was the only glacier in the top 10 frontal ablation mass losses that lost more mass due to terminus volume loss than ice discharge during either period.

To quantify the impact of frontal ablation inputs to the ocean, regardless of the source of the ice, we created a frontal ablation intensity index (Figure 4.1). This index illuminates locations where marine environments will be most impacted by icebergs within 80 km of glaciers reaching the ocean. We find that most frontal ablation occurs in areas where individual glaciers also have high contributions. These areas include near Tuttulikassaap Sermia (Hayes) & Kjer, Sermeq Kujalleq, Køge Bugt, and Nioghalvfjerdsfjorden, with peaks just under 60 Gt a^{-1} within 80 km of that point.

4.3 Discussion

4.3.1 Comparison with previous estimates of Greenland ice discharge

Recent estimates of ice sheet discharge include 487 ± 49 Gt a^{-1} for 2010-2017 (Mankoff et al., 2020) and ~490 Gt a^{-1} from 2006-2016 (King et al., 2018), although both studies exclude some ice sheet outlets and all peripheral glaciers. We found ice sheet discharge to be 465.8 ± 10.5 Gt a^{-1} for 2010-2020, or ~6% lower than previous estimates. Most of this difference is due to the location of our fluxgates typically nearer to the terminus than those used in other studies (King et al., 2018; Mankoff et al., 2020), as well as the removal of melt below our fluxgates, as discussed in detail in the following section. Our estimates for peripheral glaciers, which represent about 1% of total Greenland frontal ablation, are within the uncertainties of Chapter 3, but differ slightly due to modified assumptions about ice velocity, density, and thickness as outlined in the Materials and Methods, Section 4.5.

4.3.2 Correction due to subaerial melting

The main difference between previous discharge estimates (King et al., 2018; Mankoff et al., 2020) and our estimate here is the inclusion of subaerial melting below the fluxgate. While these numbers strongly depend on fluxgate location (i.e. a fluxgate further upstream will result in a higher melt correction), it is useful to review our estimates for approximate comparisons with other work. We calculated a mass loss of 17.0 ± 3.4 Gt a^{-1} for 2000-2010, and 14.5 ± 2.9 Gt a^{-1} for 2010-2020, due to subaerial melting after the ice passes through the fluxgate, which is therefore not included in our frontal ablation estimates. Similarly, terminus volume loss was reduced by 2.4 ± 0.5 Gt a^{-1} for 2000-2010, and 1.6 ± 0.3 Gt a^{-1} for 2010-2020, due to subaerial melting on the portion of the terminus that was either lost due to retreat or gained during

advance. Because our fluxgates were typically located lower, by tens to hundreds of meters, than those in other studies (King et al., 2018; Mankoff et al., 2020), the melt correction for these other studies would be higher than the values presented here, although it is beyond the scope of this study to determine what those values would be.

The correction due to subaerial melting below the fluxgate is less during the second decade than it is during the first decade, because there is an overall total of 35% less area below fluxgates during the later time period due to terminus retreat. The melt correction for terminus volume loss is smaller during the second decade because Greenland lost 40% less ice area during that period than in the previous decade. Even though our overall melt correction terms were smaller in both instances during 2010-2020 than 2000-2010, the specific melt rate was greater during the later period but applied over a smaller area.

4.3.3 Closing Greenland's mass budget

Estimates of the net mass loss of Greenland include 261 ± 43 Gt a^{-1} from satellite gravimetry for 2002 to 2019 (Velicogna et al., 2020), 222 ± 30 Gt a^{-1} for 2013 to 2017 (Shepherd et al., 2020), and 187 ± 17 Gt a^{-1} for 2000-2010 and 286 ± 20 Gt a^{-1} for 2010-2018 (Mouginot et al., 2019). While each of these estimates come with their own limitations and advantages, our estimates of frontal ablation over a similar period are 220-300 Gt a^{-1} greater than the net mass loss. This suggests a positive climatic-basal balance of a similar magnitude coming primarily from the accumulation of mass on the surface, but potentially also within or at the bed of the ice sheet and peripheral glaciers.

4.3.4 Northern Hemisphere frontal ablation

Combining our results with those of Chapter 3, the total frontal ablation for all glaciers that terminate in the ocean in the Northern Hemisphere is 522.0 ± 17.4 Gt a^{-1} for 2000-2010 and 559.1 ± 12.6 Gt a^{-1} for 2010-2020 (Table 4.1). We combine the results assuming that the uncertainties are uncorrelated, consistent with both studies. Greenland Ice Sheet discharge, excluding the peripheral glaciers, comprises 83% of total hemispheric frontal ablation in 2000-2010 and 2010-2020. Terminus mass loss in Greenland accounts for 9% in 2000-2010 and 7% in 2010-2020 of Northern Hemisphere frontal ablation. Overall, the Greenland Ice Sheet is by far the biggest contributor to frontal ablation in the hemisphere, making up 91% of all frontal ablation during both decades.

4.4 Conclusion

We present the first estimate of frontal ablation from all ice masses in Greenland, including both outlet glaciers from the ice sheet and periphery glaciers. There were 213 ice sheet outlets and 537 peripheral glaciers that ended in the ocean in 2000. We found frontal ablation of 481.8 ± 12.0 Gt a^{-1} for 2000-2010 and 510.2 ± 9.3 Gt a^{-1} for 2010-2020, with periphery glaciers accounting for only 1.2% of frontal ablation in 2000-2010, and 0.6% in 2010-2020. When combined with total mass balance estimates, this shows that Greenland had a positive climatic-basal balance, indicating that surface, internal, and basal accumulation is greater than surface, internal, and basal ablation.

We find that discharge made up ~90% of frontal ablation while terminus volume loss accounts for the remainder, showing the importance of fast outlet glaciers. Jakobshavn Isbrae was the largest contributor with a total frontal ablation of 42.3 ± 0.5 Gt a^{-1} from 2010-2020, almost all of which came from ice discharge. Zachariae Isstrøm lost more than twice the

terminus volume of any other glacier in Greenland during either decade, and is one of the few glaciers to have lost more mass from terminus retreat than ice discharge. In all, just 16 glaciers account for over half the total frontal ablation from 2010-2020. These glaciers are the most important to continue monitoring for future impacts on glacier mass loss and sea level rise. As a whole, Greenland accounts for 91% of frontal ablation in the northern hemisphere.

4.5 Materials and Methods

Our methods are similar to those described in Chapter 3, so we describe the highlights and differences here. The differences mainly arise where we needed to find a single unified solution to determine changes for periphery glaciers and the ice sheet, as some datasets are only available for one type of ice mass in Greenland.

4.5.1 Estimating frontal ablation

To compute frontal ablation, we sum two terms: ice discharge and terminus volume change. Ice discharge is defined as the mass through a fluxgate perpendicular to flow, calculated from the product of glacier surface velocity and thickness. We compute the terminus volume change from terminus area gained or lost multiplied by the thickness of that area. Changes in ice discharge will contribute to sea level rise, but for terminus volume change only a portion of grounded ice lost during terminus retreat, and grounded ice below water during an advance, will contribute to sea level rise. For all calculations we assume ice density is 917 kg m^{-3} to be consistent with other studies from Greenland (King et al., 2018; Mankoff et al., 2020).

4.5.2 Identification of marine-terminating glaciers.

We manually identified all marine-terminating glaciers in Greenland from Landsat 5, 7, and 8 imagery by mapping those glaciers that touched the ocean in 2000. We use RGI6 (RGI Consortium, 2017) and Mouginot and Rignot (2019) to assign unique identifiers to the periphery and ice sheet glaciers, respectively, to facilitate comparisons with past and future work. We separated periphery and ice sheet glaciers based on the Rastner et al. (2012) framework, with periphery glaciers defined as those that had either a weak (CL1) or no (CL0) hydrological connection to the ice sheet. Future work may choose to segregate glaciers differently, which our census approach allows for, and which would not change our total frontal ablation values.

4.5.3 Ice discharge

To compute ice discharge, we manually drew 3053 km of fluxgates approximately perpendicular to flow as close to the terminus of each glacier as practical, preferentially choosing fluxgate locations where ice thickness observations are available from Operation Ice Bridge (https://nsidc.org/data/icebridge) flight lines. We then extracted surface velocity and thickness estimates every 25 m along these fluxgates to compute discharge at each discrete point.

We calculate decadal average glacier surface velocities from optical and synthetic aperture radar (SAR) derived velocity datasets. We use the Inter-mission Time Series of Land Ice Velocity and Elevation (ITS_LIVE; Gardner et al., 2019) and MEaSUREs InSAR (Joughin et al., 2018) datasets for glacier surface velocity estimates. Given that optical velocity mapping is primarily undertaken from imagery acquired in summer months, and SAR derived velocities are primarily computed from imagery acquired during winter months, we combine these data to approximate decadal mean velocity. We assume that ice velocity at the surface is the same as

velocity at the bed, consistent with previous work on Greenland Ice Sheet discharge (King et al., 2018; Mankoff et al., 2020). Using the x and y components of velocity from each data source, we corrected the width of any non-perpendicular fluxgate to ensure that it was perpendicular to ice flow direction.

To obtain glacier thickness at each point along our fluxgates we preferentially use observations from Operation Ice Bridge (MacGregor et al., 2021). When those were not available we use data from Bed Machine version 4 (Morlighem et al., 2017). For many periphery glaciers Bed Machine does not include thickness estimates, so for those we use model estimates based on a similar inversion method to Bed Machine from Millan et al. (2022). For small glaciers, when no thickness observations or model results were available, we manually confirmed that the fluxgate is located on the glacier and used a thickness of 30 ± 20 m, lacking any other reasonable estimate. Of these data sources, Operation Ice Bridge observations covered 9%, Bed Machine covered 57%, Millan et al. (2022) covered 33%, and 1% of fluxgate distance was filled with a thickness of 30 ± 20 m.

4.5.4 Terminus volume change

To quantify frontal ablation due to terminus retreat or advance, we manually digitized the terminus position of each glacier in approximately 2000, 2010, and 2020, based on satellite image availability. We preferentially chose imagery as close as possible to each of these years, first from Landsat 5, 7, and 8, then from ASTER, and finally from Radarsat-1 when no optical imagery was available. We downloaded Landsat imagery from Earth Explorer (earthexplorer.usgs.gov), ASTER imagery from NASA Earth Data (earthdata.nasa.gov), and level-1 Rasarsat-1 imagery from Alaska Satellite facility (asf.alaska.edu). We reprojected the

polygon of each glacier terminus into a unique orthographic coordinate system centered on each polygon for area calculations, to eliminate errors associated with regional projections.

To convert terminus area change into a volume change, we combined the area change observation with the best available thickness data. We first use thickness observations within the terminus area gained or lost, although such observations are only available for 85 glaciers during 2000-2010 and 110 glaciers during 2010-2020. When no observations are available we use Bed Machine version 4 (Morlighem et al., 2017) or Millan et al. (2022) thickness values within the area gained or lost, which covers all remaining glaciers. When the glacier thickness was unrealistically low, less than 30 m, we assumed that these were errors in the mass conservation modeling. We instead use 60 ±30% of the mean fluxgate thickness for the thickness of area lost for these glaciers, and if it was still < 30 m, we assumed that the thickness of the area lost was 30 ± 20 m, which commonly occurred for small peripheral glaciers where modeling is challenging due to poor observations.

4.5.5 Surface mass balance and other adjustments

We use annual surface mass balance estimates from the Regional Atmospheric Climate Model version 2.3 at 1 km resolution (Noël et al., 2017) from 2000 to 2019 to determine the climatic mass balance for each glacier in order to account for sub-aerial melting once mass has passed through the fluxgate but before it calves.

To account for changes in ice thickness along a fluxgate during the study period we use geodetic mass balance estimates from Hugonnet et al. (2021) for 2000-2019, which includes all locations within 10 km of a peripheral glacier. Thus, we also used this dataset for some of the ice

sheet outlet glaciers. When these data were not available, we used geodetic mass balance estimates from Khan et al. (2022) for outlet glaciers.

While we use the same corrections to debias the data as described in Chapter 3, there are small differences. We found a bias of 43 m (model ice is too thin) when comparing observations from Operation Ice Bridge along our fluxgates and Bed Machine version 4 (Morlighem et al., 2017). We examined how this bias correlated with depth, but did not find a linear relationship, as exists with data from Millan et al. (2022). Thus, we are not able to debias Bed Machine results, but we do debias data from Millan et al. (2022), as described in Chapter 3.

4.5.6 Error analysis

Our error analysis mirrors that of Chapter 3. We use the stated uncertainties available with the velocity (Gardner et al., 2019), thickness (MacGregor et al., 2021; Millan et al., 2022; Morlighem et al., 2017), surface mass balance (Shepherd et al., 2020), and geodetic mass balance (Hugonnet et al., 2021; Khan et al., 2022) datasets. We find the uncertainty of our manual digitization of glacier termini by multiplying the perimeter of each polygon by the pixel resolution (30 m for Landsat, 15 m for ASTER, 8 m for Radarsat-1 fine beam mode) of each type of imagery used (Krumwiede et al., 2014). To examine the spatial correlation of velocity and thickness uncertainties we used global-scale, empirical variograms (Mälicke & Schneider, 2019; Matheron, 1965), testing the spatial autocorrelation from 25 m to 1000 km.

Table 4.1. Frontal ablation for different regions in the northern hemisphere, and their components due to ice discharge and terminus mass change. Values for Greenland from this study; values for glaciers outside Greenland from Chapter 3. All values show net mass loss.

	Frontal ablation (Gt a^{-1})		Ice discharge (Gt a^{-1})		Terminus mass change (Gt a^{-1})		Length of fluxgates (km)	Number of glaciers in 2000
	2000-2010	2010-2020	2000-2010	2010-2020	2000-2010	2010-2020		
Periphery Greenland	5.92 ± 3.81	3.29 ± 2.39	3.15 ± 3.73	2.31 ± 2.32	-2.77 ± 0.79	-0.99 ± 0.59	854	537
Greenland Ice Sheet	475.92 ± 15.85	506.96 ± 11.51	431.38 ± 15.09	465.83 ± 10.51	-44.54 ± 4.84	-41.13 ± 4.71	2200	213
Total Greenland	481.83 ± 12.02	510.24 ± 9.31	434.53 ± 10.61	468.13 ± 7.65	-47.31 ± 5.65	-42.12 ± 5.32	3053	750
Northern hemisphere glaciers outside Greenland	40.2 ± 6.02	48.80 ± 4.49	33.15 ± 5.36	38.53 ± 2.57	-7.01 ± 2.76	-10.27 ± 3.68	3105	959
Northern hemisphere glaciers	44.47 ± 6.23	51.98 ± 4.62	35.40 ± 5.41	40.41 ± 2.61	-9.07 ± 3.07	-11.57 ± 3.81	3802	1496
Total Northern Hemisphere	522.00 ± 17.38	559.05 ± 12.59	467.68 ± 16.44	506.69 ± 11.06	-54.33 ± 5.64	-52.38 ± 6.02	6159	1709

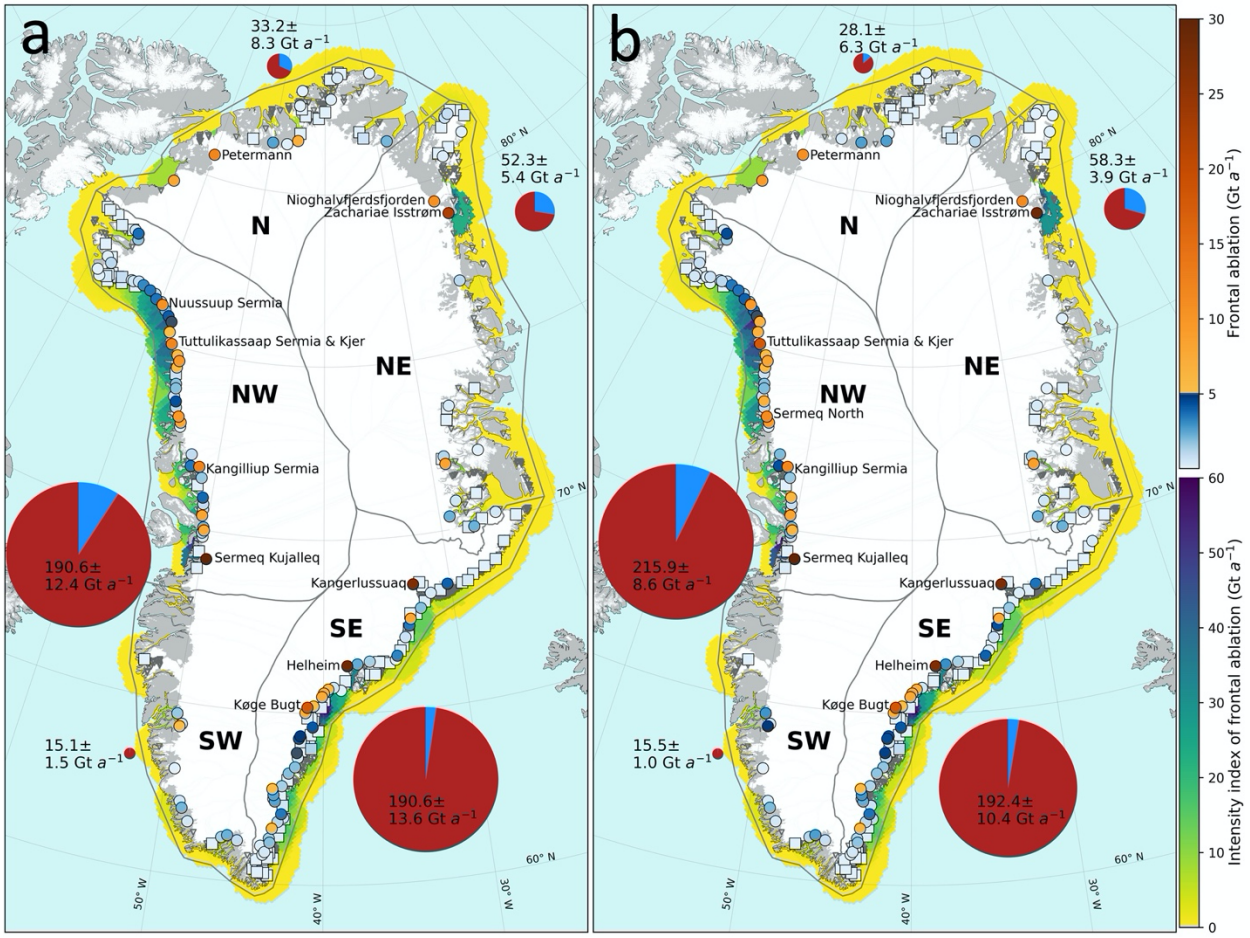


Figure 4.1 Mean annual frontal ablation of Greenland for: a) 2000-2010, b) 2010-2020. Jakobshavn Isbrae is the only glacier with frontal ablation exceeding the blue/red color scale at 36.3 Gt a^{-1} for 2000-2010 and 42.3 Gt a^{-1} for 2010-2020. The graduated circles show the portions of frontal ablation due to terminus volume loss (blue) and ice discharge (red) in each region. Squares indicate glaciers with >50% uncertainty in their frontal ablation estimates and triangles indicate glaciers with <0.02 Gt a^{-1} of frontal ablation. The yellow/green/blue color scale shows the frontal ablation intensity in the ocean for each period, defined as the sum of frontal ablation occurring within 80 km of a glacier terminus. Regions are delineated based on glacier basins from Mouginot and Rignot (2019). Labeled glaciers during each time period are the 10 largest frontal ablation rates in Greenland.

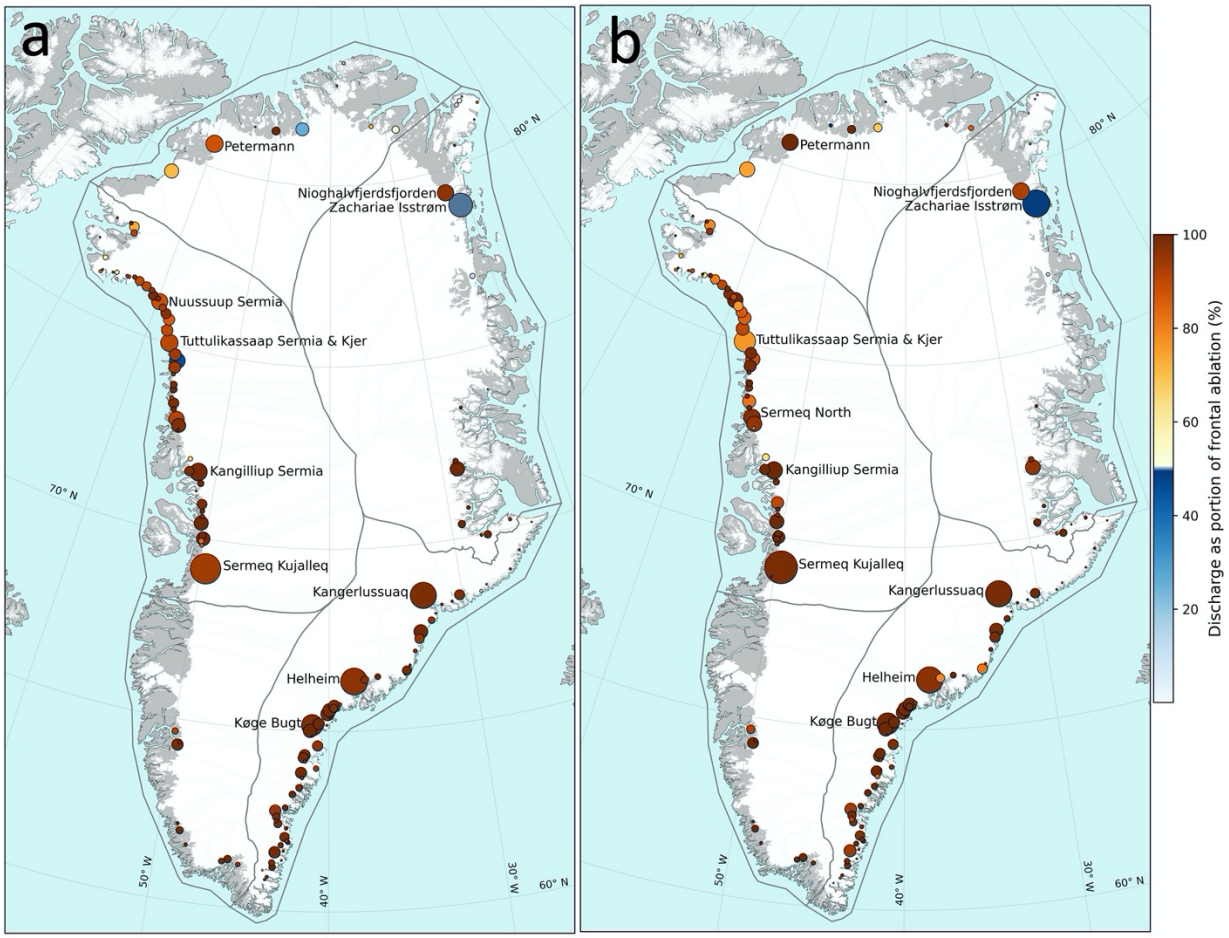


Figure 4.2 Discharge as total percent of frontal ablation for: a) 2000-2010, b) 2010-2020. The remaining portion of frontal ablation is due to terminus volume loss (retreat). Larger dots represent more frontal ablation, and the map only shows glaciers with > 0.1 Gt a^{-1} of frontal ablation. The absolute values of frontal ablation are shown in Figure 4.1 for the same periods.

Chapter 5: Conclusion

5.1 Summary

This thesis provides the first identification of every marine-terminating glacier in the Northern Hemisphere in 2000, 2010, and 2020. Locating every such glacier is critical as they represent the only mechanism to input meteoric ice into the ocean, besides direct precipitation, and are the largest contributors to sea level rise. This thesis has quantified the area change and frontal ablation of all these glaciers, which has illuminated fundamental controls on glacier retreat and completed hemispheric glacier mass budgets for the first time.

Coinciding with a negative mass balance for nearly all glaciers on Earth (Hugonnet et al., 2021), we show that 85.3% of Northern Hemisphere marine-terminating glaciers retreated from 2000-2020 and only 2.5% advanced. While warming of the ocean and atmosphere, primarily driven by increased levels of CO_2 in the atmosphere caused by anthropogenic burning of fossil fuels, has caused the recent volume loss of glaciers (IPCC, 2021), a suite of common environmental variables are unable to explain the largest retreats we observed in the Northern Hemisphere since 2000. Instead, we find that unique glacier characteristics are more important in determining if glaciers experience large and rapid retreats.

Ice shelves are particularly sensitive to small changes in the ocean and atmosphere, and their loss has resulted in the largest retreats over the last 20 years, such as the unparalleled retreat of Zachariae Isstrøm, NE Greenland. Surge-type glaciers also exhibit large retreats and are the only glaciers observed to have major advances. Due to the cyclical nature of the surge cycle (Meier & Post, 1969) these glaciers have large variations in their terminus position. This can cause glaciers to advance several kilometers, as we observed at Basin-3, Vavilov Ice Cap, and Nathorstbreen. When the surge terminates and the glacier returns to a quiescent phase, ice

velocity decreases and termini commonly retreat to account for the shifting upstream glacier dynamics. Indeed, some of the largest retreats we observed in the Northern Hemisphere occurred at surge-type glaciers including Stonebreen, Braasvellbreen, Negribreen, and Mittie, which all have been known to surge in the past but did not surge during the study period. While glacier bed observations are sparse, basal geometries with a reverse slope are particularly conducive to large retreat rates (Carr et al., 2015; O'Neel et al., 2005; Pfeffer, 2007). This is particularly true where a small initial retreat leads to further instability and retreat due to changing ice thickness and basal conditions (Carr et al., 2015; Pfeffer, 2007).

While very few glaciers have thickness observations, we identified two glaciers, Humboldt and Columbia, that displayed large retreats and have unstable basal geometries. With more thickness observations globally, we would likely find that many more glaciers have unstable geometries that contribute to, or are the primary cause of, their retreat. Glaciers with wide calving margins (e.g. ice caps and large outlets) also displayed some of the largest retreat rates since 2000 as a small amount of retreat across a wide margin can result in a large total area change. Glaciers are likely to continue retreating around the world under current and predicted future climate warming, meaning that the characteristics identified here will continue to play a key role in their future changes, and that rapidly retreating glaciers identified in this study provide priority targets for future monitoring. The advance and retreat of termini also adds to or subtracts from frontal ablation, while changes at the terminus can impact glacier dynamics.

While area change is an effective and easy monitoring tool, mass loss is much more important for sea level rise estimates and glacier mass balance modeling. Although many regional estimates of ice discharge volume exist (Błaszczyk et al., 2009; Gardner et al., 2011; King et al., 2018; Mankoff et al., 2020; Schellenberger et al., 2015; Van Wychen et al., 2012,

2014, 2016), only Alaska has complete frontal ablation estimates based on observations for any time period (McNabb et al., 2015). While discharge may approximate frontal ablation, it is not the same as it frequently includes surface ablation that occurs downstream of the arbitrarily drawn fluxgate, and does not include terminus volume change. This thesis quantifies, for the first time, a complete and methodologically consistent frontal ablation rate for each marine-terminating glacier in the Northern Hemisphere for 2000-2010 and 2010-2020.

Marine-terminating glaciers, outside the Greenland Ice Sheet, lost an average of 44.8 ± 6.2 Gt a^{-1} of ice to the ocean from 2000 to 2010 by frontal ablation, and 52.0 ± 4.6 Gt a^{-1} from 2010 to 2020. Ice discharge comprised 78 ± 13% of frontal ablation from 2000-2020, while terminus volume change made up the remainder. Total Greenland frontal ablation was 481.8 ± 12.0 Gt a^{-1} for 2000-2010 and 510.2 ± 9.3 Gt a^{-1} for 2010-2020, ~90% of which was due to ice discharge. These estimates allow for comparisons with other mass balance terms, for the first time, to close glacier mass budgets. Because total mass balance is equal to the sum of climatic-basal mass balance and frontal ablation, we can examine these three terms to better understand how different glacierized regions of the world are changing.

In Arctic Russia, the difference between frontal ablation and total mass balance, or the climatic-basal mass balance, is positive at 6.38 ± 5.27 Gt a^{-1}. This indicates that without frontal ablation the region would have a positive mass balance. Similarly, in Greenland estimates of mass balance for both ice sheet and periphery glaciers totals between 187 and 286 Gt a^{-1} from 2000-2020 (Mouginot et al., 2019; Shepherd et al., 2020; Velicogna et al., 2020). Combined with estimates of frontal ablation for the same glaciers, this indicates a positive climatic-basal mass balance of 220-300 Gt a^{-1}. In Svalbard, the frontal ablation rate is approximately equivalent to the total mass balance (Hugonnet et al., 2021), which indicates a climatic-basal balance near

zero. In the rest of the Northern Hemisphere, the total mass balance is much greater than the frontal ablation, indicating negative climatic-basal balances elsewhere.

While it is impossible to fully assess the sea level rise contributions of frontal ablation, because we cannot disentangle and account for other sources of mass loss, frontal ablation from Northern Hemisphere glaciers has been equivalent to ~30 cm of sea level rise from 2000 to 2020, with more than 90% of that coming from the Greenland Ice Sheet. However, sea level has not risen this much because this number does not consider accumulation over the same time period.

5.2 Key contributions

The primary contributions of this thesis consist of identifying all marine-terminating glaciers in the Northern Hemisphere, and individually quantifying their area and volume changes from 2000 to 2010 and 2010 to 2020, to advance our understanding of climate change impacts on glaciers, close glacier mass budgets, and inform glacier evolution models. While previous work (RGI Consortium, 2017) had attempted to identify marine-terminating glaciers, the identification was inconsistent between regions and/or incomplete. By identifying all such marine-terminating glaciers in 2000, and identifying if they continued to be marine-terminating in 2010 and 2020, future studies will be able to use this attribute for a wide variety of purposes. This could include glacier mass balance work, ice-ocean interactions, and ecology studies, among many topics. The identification of which Northern Hemisphere glaciers are marine-terminating should be included in the next release of the Randolph Glacier Inventory version 7 (RGI Consortium, 2017).

While previous studies had quantified glacier retreat within a region (Carr et al., 2017; Carr et al., 2014; Cook et al., 2019; Hill et al., 2017; King et al., 2020; McFadden et al., 2011; McNabb et al., 2015; Moon & Joughin, 2008; Murray et al., 2015), no study had quantified

retreat in a complete way for all regions using consistent methods. This approach has enabled us to understand which region in the hemisphere lost the most ice (Greenland) and understand first order controls on glacier retreat. We found that a suite of environmental variables alone could not explain the observed retreat patterns and that instead unique glacier characteristics were best able to explain the retreat, including glaciers that terminate in ice shelves or ice tongues, those with wide calving margins (e.g. ice caps), are surge-type, and those with unstable basal geometries.

Frontal ablation was the last missing part of glacier mass balance that could be quantified using observations. Previous work either relied on modeling frontal ablation (Huss & Hock, 2015), or only had regional (McNabb et al., 2015) or local (Schellenberger et al., 2015) frontal ablation estimates. For the first time, we now have frontal ablation estimates for all 1704 marine-terminating glacier outlets in the North Hemisphere, regardless of region, connectivity to the Greenland Ice Sheet, glacier size, surface velocity, or any other variable. These estimates are critically important for glacier mass balance modeling work, but can also be used to inform work on ice-ocean interactions more broadly.

5.3 Future work

To improve our understanding of the recent history, current dynamics, and future evolution of marine-terminating glaciers there are a variety of future needs at local, regional, hemispheric, and global scales. While this thesis has identified and mapped all marine-terminating glaciers and computed decadal frontal ablation rates, it relies on several underlying datasets that can be improved.

At the individual glacier scale, we need more ice thickness observations. NASA's Operation Ice Bridge has just finished (MacGregor et al., 2021), which provided air support for the systematic collection of glacier thickness measurements. While modeling techniques have recently improved (Millan et al., 2022), they still rely on velocity and thickness observations. Increasing the quantity and quality of ice thickness observations, especially at glaciers without observations, will greatly enhance model reliability and reduce any biases in the model results. New observations are particularly needed in Franz Josef Land, Russia and Greenland. New thickness observations will thus directly improve work on quantifying frontal ablation, as well as improve thickness modeling efforts.

At regional scales, studies of frontal ablation with higher temporal resolution would better illuminate changes. For example, one of the key areas with high uncertainties in frontal ablation is Svalbard. Due to the many surge-type glaciers in this region, frontal ablation can greatly vary year-to-year, but this study only provides decadal estimates. Higher temporal resolution estimates would thus be useful for ice dynamics work and to better understand ice-ocean and ecosystem interactions. Besides Svalbard, few observations of glacier change exist in the Russian Arctic archipelagos. We need fundamental work in documenting the ice shelves and ice caps of Franz Josef Land to improve forecasts of change in this region, which is one of the regions with the highest frontal ablation rates.

At hemispheric scales, future updates to this dataset will continue to help the glaciological community. With the continued explosion of Earth observation data, future updates to Northern Hemisphere frontal ablation may be available every five, or fewer, years. In the meantime, continued improvements in glacier surface velocity observations (including processing and reprocessing of satellite image archives collected since the 1970s) will improve

past and future frontal ablation estimates. While recent efforts have focused on creating the first complete velocity maps through time (Gardner et al., 2019; Lei et al., 2021) using the Landsat and Sentinel-2 satellites, the explosion in the number of Earth observing satellites in the last few years will continue to improve velocity mapping capabilities.

At the global scale, we are still missing frontal ablation estimates from Antarctica and the surrounding islands. Recent work quantifying frontal ablation from Patagonia (Minowa et al., 2021), along with this thesis, now complete all areas outside Antarctica and the surrounding islands. While frontal ablation estimates in Antarctica are complicated by the presence of large ice shelves and complex grounding line dynamics, they would greatly improve our understanding of ice-ocean interactions and enhance glacier mass balance modeling. Even though global frontal ablation estimates are not complete, results from this thesis are already being incorporated into global glacier evolution models to forecast the response of glaciers to a range of scenarios out to 2100 to inform policy makers.

This work relies on several assumptions that are necessary, but problematic, and may cause a bias in frontal ablation estimates. In Chapter 3, we assume that glacier ice has a density of 900 kg m^{-3} (Cuffey and Paterson, 2010), which is lower than the density of pure ice (917 kg m^{-3}), to account for air trapped within the ice, crevasses, firn, snow, etc. Similarly, Chapter 3 assumes that the depth-averaged velocity is 95% of the observed surface velocity. In contrast, in Chapter 4, we assume an ice density of 917 kg m^{-3} and that the depth-averaged velocity is equivalent to the surface velocity to match previous work in Greenland. Both assumptions are problematic as glacier ice must have a density of less than 917 kg m^{-3} and the depth-averaged velocity must be less than the surface velocity, but it is impossible to quantify either amount

through time or space. Thus, these assumptions make this work possible, but also introduce a bias into the resulting datasets.

Chapter 6: References

Bendtsen, J., Mortensen, J., Lennert, K., Ehn, J. K., Boone, W., Galindo, V., et al. (2017). Sea ice breakup and marine melt of a retreating tidewater outlet glacier in northeast Greenland (81°N). *Scientific Reports*, *7*(1), 1–11. https://doi.org/10.1038/s41598-017-05089-3

Bigg, G., & Billings, S. (2014). The iceberg risk in the Titanic year of 1912: Was it exceptional? *Significance*, *11*(3), 6–10. https://doi.org/10.1111/j.1740-9713.2014.00746.x

Bintanja, R. (2018). The impact of Arctic warming on increased rainfall. *Scientific Reports*, *8*(1), 6–11. https://doi.org/10.1038/s41598-018-34450-3

Bintanja, R., & Andry, O. (2017). Towards a rain-dominated Arctic. *Nature Climate Change*, *7*(4), 263–267. https://doi.org/10.1038/nclimate3240

Błaszczyk, M., Jania, J. A., & Hagen, J. O. (2009). Tidewater glaciers of Svalbard: Recent changes and estimates of calving fluxes. *Polish Polar Research*, *30*(2), 85–142.

Bojinski, S., Verstraete, M., Peterson, T. C., Richter, C., Simmons, A., & Zemp, M. (2014). The concept of essential climate variables in support of climate research, applications, and policy. *Bulletin of the American Meteorological Society*, *95*(9), 1431–1443. https://doi.org/10.1175/BAMS-D-13-00047.1

Carr, J. R., Vieli, A., Stokes, C. R., Jamieson, S. S. R., Palmer, S. J., Christoffersen, P., et al. (2015). Basal topographic controls on rapid retreat of Humboldt Glacier, northern Greenland. *Journal of Glaciology*, *61*(225), 137–150. https://doi.org/10.3189/2015JoG14J128

Carr, J. R., Stokes, C. R., & Vieli, A. (2017). Threefold increase in marine-terminating outlet glacier retreat rates across the Atlantic Arctic: 1992–2010. *Annals of Glaciology*, *58*(74), 72–91.

Carr, R., Stokes, C., & Vieli, A. (2014). Recent retreat of major outlet glaciers on Novaya Zemlya, Russian Arctic, influenced by fjord geometry and sea-ice conditions. *Journal of Glaciology*, *60*(219), 155–170. https://doi.org/10.3189/2014JoG13J122

Ciracì, E., Velicogna, I., & Swenson, S. (2020). Continuity of the mass loss of the world's glaciers and ice caps from the GRACE and GRACE Follow-On missions. *Geophysical Research Letters*, *47*, 9.

Clarke, G. K. C., Schmok, J. P., Ommanney, C. S. L., & Collins, S. G. (1986). Characteristics of surge-type glaciers. *Journal of Geophysical Research*, *91*, 7165–7180.

Cogley, J. G., Hock, R., Rasmussen, L. A., Arendt, A. A., Bauder, A., Braithwaite, R. J., et al. (2011). Glossary of Glacier Mass Balance and Related Terms. *IHP-VII Technical Documents in Hydrology No*, *86*.

Cook, A. J., Copland, L., Noël, B. P. Y., Stokes, C. R., Bentley, M. J., Sharp, M. J., et al. (2019). Atmospheric forcing of rapid marine-terminating glacier retreat in the Canadian Arctic Archipelago. *Science Advances*, *5*(3), 1–11. https://doi.org/10.1126/sciadv.aau8507

Copernicus. (2019). ERA5 monthly averaged data on single levels from 1979 to present. https://doi.org/10.24381/cds.f17050d7

Copland, L., & Mueller, D. (2017). *Arctic Ice Shelves and Ice Islands*. *Arctic Ice Shelves and Ice Islands*.

Copland, L., Sharp, M. J., & Dowdeswell, J. A. (2003). The distribution and flow characteristics of surge-type glaciers in the Canadian High Arctic. *Annals of Glaciology*, *36*, 73–81. https://doi.org/10.3189/172756403781816301

Copland, L., Mueller, D. R., & Weir, L. (2007). Rapid loss of the Ayles Ice Shelf, Ellesmere

Island, Canada. *Geophysical Research Letters*, *34*(21), 1–6. https://doi.org/10.1029/2007GL031809
Crawford, A., Crocker, G., Mueller, D., Desjardins, L., Saper, R., & Carrieres, T. (2018). The Canadian Ice Island Drift, Deterioration and Detection (CI2D3) Database. *Journal of Glaciology*, *64*(245), 517–521. https://doi.org/10.1017/jog.2018.36
CReSIS. (2016). Multichannel Coherent Depth Sounder (MCoRDS) L3 Gridded Data.
Cuffey, K. M., & Paterson, W. S. B. (2010). *The Physics of Glaciers*. Academic Press.
Dowdeswell, J A. (2017). Eurasian Arctic ice shelves and tidewater ice margins. In L Copland & D. R. Mueller (Eds.), *Arctic Ice Shelves and Ice Islands* (pp. 55–74). Dordrecht: Springer.
Dowdeswell, J. A., & Williams, M. (1997). Surge-type glaciers in the Russian High Arctic identified from digital satellite imagery. *Journal of Glaciology*, *43*(145), 489–494.
Dowdeswell, J. A., Gorman, M. R., Glazovsky, A. F., & Macheret, Y. Y. (1996). Airborne radio-echo sounding of the ice caps on Franz Josef Land in 1994. *Materialy Glyatsiologicheskikh Issledovaniy, Khronika*, *80*, 248–254.
Dowdeswell, J. A., Bassford, R. P., Gorman, M. R., Williams, M., Glazovsky, A. F., Macheret, Y. Y., et al. (2002). Form and flow of the Academy of Sciences Ice Cap, Severnaya Zemlya, Russian High Arctic. *Journal of Geophysical Research*, *107*. https://doi.org/10.1029/2000JB000129
Dowdeswell, J. A., Benham, T. J., Strozzi, T., & Hagen, J. O. (2008). Iceberg calving flux and mass balance of the Austfonna ice cap on Nordaustlandet, Svalbard. *Journal of Geophysical Research: Earth Surface*, *113*. https://doi.org/10.1029/2007JF000905
Dowdeswell, J. A., Hamilton, G. S., & Hagen, J. O. (1991). The duration of the active phase on surge-type glaciers: contrasts between Svalbard and other regions. *Journal of Glaciology*, *37*(127), 388–400. https://doi.org/10.3189/S0022143000005827
Dunse, T., Schellenberger, T., Hagen, J. O., Kääb, A., Schuler, T. V., & Reijmer, C. H. (2015). Glacier-surge mechanisms promoted by a hydro-thermodynamic feedback to summer melt. *The Cryosphere*, *9*(1), 197–215. https://doi.org/10.5194/tc-9-197-2015
Fahrner, D., Lea, J. M., Brough, S., Mair, D. W. F., & Abermann, J. (2021). Linear response of the Greenland ice sheet's tidewater glacier terminus positions to climate. *Journal of Glaciology*, *67*(262), 193–203. https://doi.org/10.1017/jog.2021.13
Fettweis, X., Hofer, S., Krebs-Kanzow, U., Amory, C., Aoki, T., Berends, C. J., et al. (2020). GrSMBMIP: Intercomparison of the modelled 1980-2012 surface mass balance over the Greenland Ice Sheet. *The Cryosphere*, *14*(11), 3935–3958. https://doi.org/10.5194/tc-14-3935-2020
Friedl, P., Seehaus, T., & Braun, M. (2021). Global time series and temporal mosaics of glacier surface velocities, derived from Sentinel-1 data Peter, (June), 1–33. ??? Missing name of journal or website
Gardner, A. S., Moholdt, M., Wouters, B., Wolken, G. J., Burgess, D. O., Sharp, M., et al. (2011). Sharply increased mass loss from glaciers and ice caps in the Canadian Arctic Archipelago. *Nature*, *473*, 7347. https://doi.org/10.1038/nature10089
Gardner, A. S., Moholdt, G., Scambos, T., Fahnstock, M., Ligtenberg, S., van den Broeke, M., & Nilsson, J. (2018). Increased West Antarctic and unchanged East Antarctic ice discharge over the last 7 years. *The Cryosphere*, *12*, 2. https://doi.org/10.5194/tc-12-521-2018
Gardner, A. S., Fahnestock, M. A., & Scambos, T. A. (2019). *ITS_LIVE regional glacier and ice sheet surface velocities*. Data archived at National Snow and Ice Data Center; https://doi.org/10.5067/6II6VW8LLWJ7

Gerringa, L. J. A., Alderkamp, A.-C., Laan, P., Thuróczy, C.-E., De Baar, H. J. W., Mills, M. M., et al. (2012). Iron from melting glaciers fuels the phytoplankton blooms in Amundsen Sea (Southern Ocean): Iron biogeochemistry. *Deep Sea Research Part II: Topical Studies in Oceanography*, *71–76*, 16–31. https://doi.org/https://doi.org/10.1016/j.dsr2.2012.03.007

GlaThiDa Consortium. (2019). *Glacier Thickness Database 3.0.1*. Zurich, Switzerland: World Glacier Monitoring Service. https://doi.org/10.5904/wgms-glathida-2019-03

Glazovsky, A., Lavrentiev, I., & Vasilenko, E. I. (2018). Ice thickness and frontal ablation of nine outlet glaciers on Novaya Zemlya (Vol. 2018). Davos: Open Science Conference POLAR 2018.

Glazovsky, A., Lavrentiev, I., Vasilenko, E., & Elagina, N. R. (2018). N. RES ice thickness and frontal ablation of outlet glaciers in Russian Arctic (pp. 22–24). IASC Workshop on the Dynamics and Mass Budget of Arctic Glaciers & Proglacial Marine Ecosystems, Obergurgl, Austria.

Goelzer, H., Nowicki, S., Payne, A., Larour, E., Seroussi, H., Lipscomb, W. H., et al. (2020). The future sea-level contribution of the Greenland ice sheet: A multi-model ensemble study of ISMIP6. *The Cryosphere*, *14*(9), 3071–3096. https://doi.org/10.5194/tc-14-3071-2020

Grant, K. L., Stokes, C. R., & Evans, I. S. (2009). Identification and characteristics of surge-type glaciers on Novaya Zemlya, Russian Arctic. *Journal of Glaciology*, *55*(194), 960–972.

Hagen, J. O., Melvold, K., Pinglot, F., & Dowdeswell, J. A. (2003). On the Net Mass Balance of the Glaciers and Ice Caps in Svalbard, Norwegian Arctic. *Arctic, Antarctic, and Alpine Research*, *35*(2), 264–270. https://doi.org/10.1657/1523-0430(2003)035[0264:OTNMBO]2.0.CO;2

Hersbach, H., Bell, B., Berrisford, P., Hirahara, S., Horányi, A., Muñoz-Sabater, J., et al. (2020). The ERA5 global reanalysis. *Quarterly Journal of the Royal Meteorological Society*, *146*(730), 1999–2049. https://doi.org/10.1002/qj.3803

Hill, E. A., Carr, J. R., & Stokes, C. R. (2017). A review of recent changes in major marine-terminating outlet glaciers in northern Greenland. *Frontiers in Earth Science*, *4*(January), 1–23. https://doi.org/10.3389/feart.2016.00111

Hopwood, M. J., Carroll, D., Dunse, T., Hodson, A., Holding, J. M., Iriarte, J. L., et al. (2020). Review article: How does glacier discharge affect marine biogeochemistry and primary production in the Arctic? *The Cryosphere*, *14*(4), 1347–1383. https://doi.org/10.5194/tc-14-1347-2020

Huang, J., Zhang, X., Zhang, Q., Lin, Y., Hao, M., Luo, Y., et al. (2017). Recently amplified arctic warming has contributed to a continual global warming trend. *Nature Climate Change*, *7*(12), 875–879. https://doi.org/10.1038/s41558-017-0009-5

Hugonnet, R., McNabb, R., Berthier, E., Menounos, B., Nuth, C., Girod, L., et al. (2021). Accelerated global glacier mass loss in the early twenty-first century. *Nature*, *592*(April). https://doi.org/10.1038/s41586-021-03436-z

Huss, M., & Hock, R. (2015). A new model for global glacier change and sea-level rise. *Frontiers in Earth Science*, *3*. https://doi.org/10.3389/feart.2015.00054

IPCC. (2021). *Climate Change 2021: The Physical Science Basis. Contribution of Working Group I to the Sixth Assessment Report of the Intergovernmental Panel on Climate Change*. (R. Y. and B. Z. Masson-Delmotte, V., P. Zhai, A. Pirani, S. L. Connors, C. Péan, S. Berger, N. Caud, Y. Chen, L. Goldfarb, M. I. Gomis, M. Huang, K. Leitzell, E. Lonnoy, J. B. R. Matthews, T. K. Maycock, T. Waterfield, O. Yelekçi, Ed.). Cambridge University Press.

Jevrejeva, S., Moore, J. C., & Grinsted, A. (2012). Sea level projections to AD2500 with a new generation of climate change scenarios. *Global and Planetary Change*, *80–81*, 14–20. https://doi.org/10.1016/j.gloplacha.2011.09.006

Jiskoot, H. (2011). Glacier Surging. In S. P. P. & U. K. Haritashya (Eds.), *Encyclopedia of Snow Ice and Glaciers*. Dordrecht: Springer. https://doi.org/10.1007/978-90-481-2642-2_559

Jiskoot, H., Pedersen, A. K., & Murray, T. (2001). Multi-model photogrammetric analysis of the 1990s surge of Sortebræ, East Greenland. *Journal of Glaciology*, *47*(159), 677–687. https://doi.org/10.3189/172756501781831846

Jiskoot, H., Murray, T., & Luckman, A. (2003). Surge potential and drainage-basin characteristics in East Greenland. *Annals of Glaciology*, *36*, 142–148. https://doi.org/10.3189/172756403781816220

Joughin, I., Smith, B., Howat, I., Scambos, T. and Moon, T. (2018). MEaSUREs Greenland Ice Sheet Velocity Map from InSAR Data, Version 2. *NASA National Snow and Ice Data Center Distributed Active Archive Center*. Boulder. https://doi.org/10.5067/OC7B04ZM9G6Q.

Khan, S. A., Bamber, J. L., Rignot, E., Helm, V., Aschwanden, A., Holland, D. M., et al. (2022). Greenland mass trends from airborne and satellite altimetry during 2011-2020. *Journal of Geophysical Research: Earth Surface*, 1–20. https://doi.org/10.1029/2021jf006505

King, M. D., Howat, I. M., Jeong, S., Noh, M. J., Wouters, B., Noël, B., & Van Den Broeke, M. R. (2018). Seasonal to decadal variability in ice discharge from the Greenland Ice Sheet. *The Cryosphere*, *12*(12), 3813–3825. https://doi.org/10.5194/tc-12-3813-2018

King, M. D., Howat, I. M., Candela, S. G., Noh, M. J., Jeong, S., Noël, B. P. Y., et al. (2020). Dynamic ice loss from the Greenland Ice Sheet driven by sustained glacier retreat. *Communications Earth & Environment*, *1*(1), 1–7. https://doi.org/10.1038/s43247-020-0001-2

Kochtitzky, W., & Copland, L. (2022). Retreat of Northern Hemisphere Marine-Terminating Glaciers, 2000–2020. *Geophysical Research Letters*, *49*(3), 1–10. https://doi.org/10.1029/2021gl096501

Krumwiede, B. S., Kamp, U., Leonard, G. J., Kargel, J. S., Dashtseren, A., & Walther, M. (2014). Recent glacier changes in the Mongolian Altai Mountains: case studies from Munkh Khairkhan and Tavan Bogd. In R. B. Kargel J., Leonard G., Bishop M., Kääb A. (Ed.), *Global Land Ice Measurements From Space* (pp. 481–508). Berlin: Springer. https://doi.org/10.1007/978-3-540-79818-7_22

Lea, J. M., Mair, D. W. F., & Rea, B. R. (2014). Instruments and Methods :Evaluation of existing and new methods of tracking glacier terminus change. *Journal of Glaciology*, *60*(220), 323–332. https://doi.org/10.3189/2014JoG13J061

Lei, Y., Gardner, A., & Agram, P. (2021). Autonomous repeat image feature tracking (Autorift) and its application for tracking ice displacement. *Remote Sensing*, *13*(4), 1–20. https://doi.org/10.3390/rs13040749

Lesins, G., Duck, T., & Drummond, J. (2010). Climate trends at Eureka in the Canadian high arctic. *Atmosphere - Ocean*, *48*(2), 59–80. https://doi.org/10.3137/AO1103.2010

MacGregor, J. A., Boisvert, L. N., Medley, B., Petty, A. A., Harbeck, J. P., Bell, R. E., et al. (2021). The Scientific Legacy of NASA's Operation IceBridge. *Reviews of Geophysics*, *59*(2). https://doi.org/10.1029/2020RG000712

Macheret, Y. Y., Glazovsky, A. F., Dowdeswell, J. A., & Gorman, M. R. (2000). Ice volume change on Franz Josef Land during the last 40 years. *Zeitschrift Für Gletscherkunde Und*

Glazialgeologie, *35*, 103–116.
Maksym, T. (2019). Arctic and antarctic sea ice change: Contrasts, commonalities, and causes. *Annual Review of Marine Science*, *11*, 187–213. https://doi.org/10.1146/annurev-marine-010816-060610
Mälicke, M., & Schneider, H. D. (2019). Scikit-GStat 0.2.6: A scipy flavored geostatistical analysis toolbox written in Python. https://doi.org/10.5281/ZENODO.3531816
Mankoff, K. D., Solgaard, A., Colgan, W., Ahlstrøm, A. P., Khan, S. A., & Fausto, R. S. (2020). Greenland Ice Sheet solid ice discharge from 1986 through March 2020. *Earth System Science Data*, *12*(2), 1367–1383. https://doi.org/10.5194/essd-12-1367-2020
Mansell, D., Luckman, A., & Murray, T. (2012). Dynamics of tidewater surge-type glaciers in northwest Svalbard. *Journal of Glaciology*, *58*(207), 110–118. https://doi.org/10.3189/2012JoG11J058
Matheron, G. (1965). *Les variables régionalisées et leur estimation. Une application de la théorie des fonctions aléatoires aux sciences de la nature. Masson et Cie*.
Mayer, C., Schaffer, J., Hattermann, T., Floricioiu, D., Krieger, L., Dodd, P. A., et al. (2018). Large ice loss variability at Nioghalvfjerdsfjorden Glacier, Northeast-Greenland. *Nature Communications*, *9*(1), 1–11. https://doi.org/10.1038/s41467-018-05180-x
McFadden, E. M., Howat, I. M., Joughin, I., Smith, B. E., & Ahn, Y. (2011). Changes in the dynamics of marine terminating outlet glaciers in west Greenland (2000-2009). *Journal of Geophysical Research: Earth Surface*, *116*(2), 1–16. https://doi.org/10.1029/2010JF001757
McNabb, R. W., Hock, R., & Huss, M. (2015). Variations in Alaska tidewater glacier frontal ablation, 1985-2013. *Journal of Geophysical Research Earth Surface*, *120*, 120–136. https://doi.org/10.1002/2014JF003276
Medrzycka, D., Copland, L., Van Wychen, W., & Burgess, D. (2019). Seven decades of uninterrupted advance of Good Friday Glacier, Axel Heiberg Island, Arctic Canada. *Journal of Glaciology*, *65*(251), 440–452.
Meier, M., & Post, A. (1987). Fast tidewater glaciers. *Journal of Geophysical Research*, *92*(B9). https://doi.org/10.1029/JB092iB09p09051
Meier, Mark F., & Post, A. (1969). What are glacial surges? *Canadian Journal of Earth Sciences*.
Meier, W. N., Fetterer, F., Savoie, M., Mallory, S., Duerr, R., & Stroeve, J. (2017). NOAA/NSIDC Climate Data Record of Passive Microwave Sea Ice Concentration, Version 3. Boulder, Colorado USA: NSIDC: National Snow and Ice Data Center. https://doi.org/https://doi.org/10.7265/N59P2ZTG
Meire, L., Mortensen, J., Meire, P., Juul-Pedersen, T., Sejr, M. K., Rysgaard, S., et al. (2017). Marine-terminating glaciers sustain high productivity in Greenland fjords. *Global Change Biology*, *23*(12), 5344–5357. https://doi.org/10.1111/gcb.13801
Millan, R., Mouginot, J., Rabatel, A., & Morlighem, M. (2022). Ice velocity and thickness of the world's glaciers. *Nature Geoscience*, *15*, 1–6. https://doi.org/10.1038/s41561-021-00885-z
Minowa, M., Schaefer, M., Sugiyama, S., Sakakibara, D., & Skvarca, P. (2021). Frontal ablation and mass loss of the Patagonian icefields. *Earth and Planetary Science Letters*, *561*, 116811. https://doi.org/10.1016/j.epsl.2021.116811
Moholdt, G., Hagen, J. O., Eiken, T., & Schuler, T. V. (2010). Geometric changes and mass balance of the Austfonna ice cap, Svalbard. *The Cryosphere*, *4*(1), 21–34. https://doi.org/10.5194/tc-4-21-2010
Moon, T., Sutherland, D. A., Carroll, D., Felikson, D., Kehrl, L., & Straneo, F. (2018).

Subsurface iceberg melt key to Greenland fjord freshwater budget. *Nature Geoscience*, *11*(1), 49–54. https://doi.org/10.1038/s41561-017-0018-z

Moon, T., & Joughin, I. (2008). Changes in ice front position on Greenland's outlet glaciers from 1992 to 2007. *Journal of Geophysical Research: Earth Surface*, *113*(2), 1–10. https://doi.org/10.1029/2007JF000927

Morlighem, M., Williams, C. N., Rignot, E., An, L., Arndt, J. E., Bamber, J. L., et al. (2017). BedMachine v3: Complete Bed Topography and Ocean Bathymetry Mapping of Greenland From Multibeam Echo Sounding Combined With Mass Conservation. *Geophysical Research Letters*, *44*(21), 11,051-11,061. https://doi.org/10.1002/2017GL074954

Mouginot, J., & Rignot, E. (2019). Glacier catchments/basins for the Greenland Ice Sheet. *Dryad*. https://doi.org/doi.org/10.7280/D1WT11

Mouginot, J., Rignot, E., Scheuchl, B., Fenty, I., Khazendar, A., Morlighem, M., et al. (2015). Fast retreat of Zachariæ Isstrøm, northeast Greenland. *Science*, *350*(6266). https://doi.org/10.1126/science.aac7111

Mouginot, J., Rignot, E., Bjørk, A. A., van den Broeke, M., Millan, R., Morlighem, M., et al. (2019). Forty-six years of Greenland Ice Sheet mass balance from 1972 to 2018. *Proceedings of the National Academy of Sciences of the United States of America*, *116*(19), 9239–9244. https://doi.org/10.1073/pnas.1904242116

Münchow, A., Padman, L., & Fricker, H. A. (2014). Interannual changes of the floating ice shelf of Petermann Gletscher, North Greenland, from 2000 to 2012. *Journal of Glaciology*, *60*(221), 489–499. https://doi.org/10.3189/2014JoG13J135

Murray, T., Scharrer, K., Selmes, N., Booth, A. D., James, T. D., Bevan, S. L., et al. (2015). Extensive Retreat of Greenland Tidewater Glaciers, 2000-2010. *Arctic, Antarctic, and Alpine Research*, *47*(3), 427–447. https://doi.org/10.1657/AAAR0014-049

Nerem, R. S., Beckley, B. D., Fasullo, J. T., Hamlington, B. D., Masters, D., & Mitchum, G. T. (2018). Climate-change–driven accelerated sea-level rise detected in the altimeter era. *Proceedings of the National Academy of Sciences of the United States of America*, *115*(9), 2022–2025. https://doi.org/10.1073/pnas.1717312115

Nick, F. M., Vieli, A., Howat, I. M., & Joughin, I. (2009). Large-scale changes in Greenland outlet glacier dynamics triggered at the terminus. *Nature Geoscience*, *2*(2), 110–114. https://doi.org/10.1038/ngeo394

Noël, B., Van De Berg, W. J., Lhermitte, S., Wouters, B., Machguth, H., Howat, I., et al. (2017). A tipping point in refreezing accelerates mass loss of Greenland's glaciers and ice caps. *Nature Communications*, *8*(9296). https://doi.org/10.1038/ncomms14730

Noël, B, van de Berg, W. J., Lhermitte, S., Wouters, B., Schaffer, N., & van den Broeke, M. (2018). Six decades of glacial mass loss in the Canadian Arctic Archipelago. *Journal of Geophysical Research: Earth Surface*, *123*(6), 1430–1449.

Noël, B., Van De Berg, W. J., Van Wessem, J. M., Van Meijgaard, E., Van As, Di., Lenaerts, J. T. M., et al. (2018). Modelling the climate and surface mass balance of polar ice sheets using RACMO2 - Part 1: Greenland (1958-2016). *The Cryosphere*, *12*(3), 811–831. https://doi.org/10.5194/tc-12-811-2018

Noël, B., Jakobs, C. L., van Pelt, W. J. J., Lhermitte, S., Wouters, B., Kohler, J., et al. (2020). Low elevation of Svalbard glaciers drives high mass loss variability. *Nature Communications*, *11*(1), 1–8. https://doi.org/10.1038/s41467-020-18356-1

O'Neel, S., Pfeffer, W. T., Krimmel, R., & Meier, M. (2005). Evolving force balance at Columbia Glacier, Alaska, during its rapid retreat. *Journal of Geophysical Research: Earth*

Surface, *110*(3), 1–18. https://doi.org/10.1029/2005JF000292
Østby, T. I., Vikhamar Schuler, T., Ove Hagen, J., Hock, R., Kohler, J., & Reijmer, C. H. (2017). Diagnosing the decline in climatic mass balance of glaciers in Svalbard over 1957-2014. *The Cryosphere*, *11*(1), 191–215. https://doi.org/10.5194/tc-11-191-2017
Paul, P., Bolch, T., Kääb, A., Nagler, T., Nuth, C., Scharrer, K., et al. (2015). The glaciers climate change initiative: Methods for creating glacier area; elevation change and velocity products. *Remote Sensing of Environment*, *162*, 408.
Peng, G., Meier, W. N., Scott, D. J., & Savoie, M. H. (2013). A long-term and reproducible passive microwave sea ice concentration data record for climate studies and monitoring. *Earth System Science Data*, *5*(2), 311–318. https://doi.org/10.5194/essd-5-311-2013
Pfeffer, W. T. (2007). A simple mechanism for irreversible tidewater glacier retreat. *Journal of Geophysical Research: Earth Surface*, *112*(3), 1–12. https://doi.org/10.1029/2006JF000590
Pfeffer, W. Tad, Arendt, A. A., Bliss, A., Bolch, T., Cogley, J. G., Gardner, A. S., et al. (2014). The Randolph Glacier Inventory: A globally complete inventory of glaciers. *Journal of Glaciology*, *60*(221), 537–552. https://doi.org/10.3189/2014JoG13J176
Pörtner, H.- O., Roberts, D.C., Masson-Delmotte, V., Zhai, P., Tignor, M., Poloczanska, E. , Mintenbeck, K., Nicolai, M., Okem, A., Petzold, J., Rama, B. (2019). *IPCC Special Report on the Ocean and Cryosphere in a Changing Climate*.
Rasmussen, L. A., Conway, H., Krimmel, R. M., & Hock, R. (2011). Surface mass balance, thinning and iceberg production, Columbia Glacier, Alaska, 1948-2007. *Journal of Glaciology*, *57*(203), 431–440. https://doi.org/10.3189/002214311796905532
Rastner, P., Bolch, T., Mölg, N., Machguth, H., Le Bris, R., & Paul, F. (2012). The first complete inventory of the local glaciers and ice caps on Greenland. *The Cryosphere*, *6*(6), 1483–1495.
Recinos, B., Maussion, F., Noël, B., Möller, M., & Marzeion, B. (2021). Calibration of a frontal ablation parameterisation applied to Greenland's peripheral calving glaciers. *Journal of Glaciology*, *67*(266), 1177–1189. https://doi.org/10.1017/jog.2021.63
RGI Consortium. (2017). *Randolph Glacier Inventory – A Dataset of Global Glacier Outlines: Version 6.0:*
Rounce, D. R., Hock, R., & Shean, D. E. (2020). Glacier Mass Change in High Mountain Asia Through 2100 Using the Open-Source Python Glacier Evolution Model (PyGEM). *Frontiers in Earth Science*, *7*(January), 1–20. https://doi.org/10.3389/feart.2019.00331
Rounce, D. R., Khurana, T., Short, M. B., Hock, R., Shean, D. E., & Brinkerhoff, D. J. (2020). Quantifying parameter uncertainty in a large-scale glacier evolution model using Bayesian inference: Application to High Mountain Asia. *Journal of Glaciology*, *66*(256), 175–187. https://doi.org/10.1017/jog.2019.91
Sánchez-Gámez, P., & Navarro, F. (2018). Ice discharge error estimates using different cross-sectional area approaches: A case study for the Canadian High Arctic, 2016/17. *Journal of Glaciology*, *64*(246), 595–608. https://doi.org/10.1017/jog.2018.48
Sánchez-Gámez, P., Navarro, F., Benham, T., Glazovsky, A., Bassford, R., & Dowdeswell, J. (2019). Intra- and inter-annual variability in dynamic discharge from the Academy of Sciences Ice Cap, Severnaya Zemlya, Russian Arctic, and its role in modulating mass balance. *Journal of Glaciology*, *65*(253), 780–797. https://doi.org/10.1017/jog.2019.58
Scambos, T. A., Berthier, E., Haran, T., Shuman, C. A., Cook, A. J., Ligtenberg, S. R. M., & Bohlander, J. (2014). Detailed ice loss pattern in the northern Antarctic Peninsula: Widespread decline driven by ice front retreats. *The Cryosphere*, *8*(6), 2135–2145.

https://doi.org/10.5194/tc-8-2135-2014
Scheick, J., Enderlin, E. M., Miller, E. E., & Hamilton, G. (2019). First-Order Estimates of Coastal Bathymetry in Ilulissat and Naajarsuit Fjords, Greenland, from Remotely Sensed Iceberg Observations. *Remote Sensing*, *11*(8). https://doi.org/10.3390/rs11080935
Schellenberger, T., Dunse, T., Kääb, A., Kohler, J., & Reijmer, C. H. (2015). Surface speed and frontal ablation of Kronebreen and Kongsbreen, NW Svalbard, from SAR offset tracking. *The Cryosphere*, *9*(6), 2339–2355.
Schoof, C. (2007). Ice sheet grounding line dynamics: Steady states, stability, and hysteresis. *Journal of Geophysical Research: Earth Surface*, *112*(3), 1–19. https://doi.org/10.1029/2006JF000664
Schuler, T. V, Kohler, J., Elagina, N., Hagen, J. O. M., Hodson, A. J., Jania, J. A., et al. (2020). Reconciling Svalbard glacier mass balance. *Frontiers in Earth Science*, *8*.
Sevestre, H., & Benn, D. I. (2015). Climatic and geometric controls on the global distribution of surge-type glaciers: implications for a unifying model of surging. *Journal of Glaciology*, *61*(228), 646–662.
Shepherd, A., Ivins, E., Rignot, E., Smith, B., van den Broeke, M., Velicogna, I., et al. (2020). Mass balance of the Greenland Ice Sheet from 1992 to 2018. *Nature*, *579*(7798), 233–239. https://doi.org/10.1038/s41586-019-1855-2
Sochnev, O., Kornishin, K., Tarasov, P., Salman, A., Glazovsky, A., Lavrentiev, I., et al. (2018). Studies of glaciers in the Russian Arctic for safe marine operations in iceberg waters. *Oil Industry*, *10*(1140), 92–97. https://doi.org/10.24887/0028-2448-2018-10-92-97
Strozzi, T, Kouraev, A., Wiesmann, A., Wegmüller, U., Sharov, A., & Werner, C. (2008). Estimation of Arctic glacier motion with satellite L-band SAR data. *Remote Sensing of Environment*, *112*(3), 636–645.
Strozzi, Tazio, Kääb, A., & Schellenberger, T. (2017). Frontal destabilization of Stonebreen, Edgeøya, Svalbard. *The Cryosphere*, *11*(1), 553–566. https://doi.org/10.5194/tc-11-553-2017
Stuecker, M. F., Bitz, C. M., Armour, K. C., Proistosescu, C., Kang, S. M., Xie, S. P., et al. (2018). Polar amplification dominated by local forcing and feedbacks. *Nature Climate Change*, *8*(12), 1076–1081. https://doi.org/10.1038/s41558-018-0339-y
Sund, M., Lauknes, T. R., & Eiken, T. (2014). Surge dynamics in the Nathorstbreen Glacier system, Svalbard. *The Cryosphere*, *8*(2), 623–638. https://doi.org/10.5194/tc-8-623-2014
Tarasov, P., Kornishin, K., Lavrentiev, I., Mamedov, T., Glazovsky, A., Bagorian, E., et al. (2019). Outlet glaciers as iceberg factories: case study for the Kara Sea. In *Proceedings of the Twenty-ninth (2019) International Ocean and Polar Engineering Conference* (pp. 16–21). Hawaii, USA, June: Honolulu.
Tepes, P., Gourmelen, N., Nienow, P., Tsamados, M., Shepherd, A., & Weissgerber, F. (2021). Changes in elevation and mass of Arctic glaciers and ice caps, 2010–2017. *Remote Sensing of Environment*, *261*(May), 2010–2017. https://doi.org/10.1016/j.rse.2021.112481
Van Wychen, W., Copland, L., Gray, L., Burgess, D., Danielson, B., & Sharp, M. (2012). Spatial and temporal variation of ice motion and ice flux from Devon Ice Cap, Nunavut, Canada. *Journal of Glaciology*, *58*(210), 657–664.
Van Wychen, W., Burgess, D. O., Gray, L., Copland, L., Sharp, M., Dowdeswell, J. A., & Benham, T. J. (2014). Glacier velocities and dynamic ice discharge from the Queen Elizabeth Islands, Nunavut, Canada. *Geophysical Research Letters*, *41*(2), 484–490.
Van Wychen, W., Davis, J., Burgess, D. O., Copland, L., Gray, L., Sharp, M., & Mortimer, C.

(2016). Characterizing interannual variability of glacier dynamics and dynamic discharge (1999-2015) for the ice masses of Ellesmere and Axel Heiberg Islands, Nunavut, Canada. *Journal of Geophysical Research Earth Surface*, *121*(1), 39–63. https://doi.org/10.1002/2015JF003708

Van Wychen, W., Burgess, D., Kochtitzky, W., Nikolic, N., Copland, L., & Gray, L. (2021). RADARSAT-2 derived glacier velocities and dynamic discharge estimates for the Canadian High Arctic: 2015–2020. *Canadian Journal of Remote Sensing, Pp*, 1–23.

Velicogna, I., Mohajerani, Y., Geruo, A., Landerer, F., Mouginot, J., Noel, B., et al. (2020). Continuity of ice sheet mass loss in Greenland and Antarctica from the GRACE and GRACE Follow-On missions. *Geophysical Research Letters*, *47*(8). https://doi.org/10.1029/2020GL087291

Vincent, W. F., Gibson, J. A. E., & Jeffries, M. O. (2001). Ice-shelf collapse, climate change, and habitat loss in the Canadian high Arctic. *Polar Record*, *37*(201), 133–142. https://doi.org/10.1017/S0032247400026954

Webster, R., & Oliver, M. A. (2008). *Geostatistics for Environmental Scientists: Second Edition*. *Geostatistics for Environmental Scientists: Second Edition*. https://doi.org/10.1002/9780470517277

White, A., & Copland, L. (2019). Loss of floating glacier tongues from the Yelverton Bay region, Ellesmere Island, Canada. *Journal of Glaciology*, *65*(251), 376–394. https://doi.org/10.1017/jog.2019.15

Willis, M., Melkonian, A., & Pritchard, M. (2015). Outlet glacier response to the 2012 collapse of the Matusevich Ice Shelf, Severnaya Zemlya, Russian Arctic. *Journal of Geophysical Research: Earth Surface*, *120*(10), 2040–2055. https://doi.org/https://doi.org/10.1002/2015JF003544

Willis, M. J., Zheng, W., Durkin, W. J., Pritchard, M. E., Ramage, J. M., Dowdeswell, J. A., et al. (2018). Massive destabilization of an Arctic ice cap. *Earth and Planetary Science Letters*, *502*, 146–155.

Wood, M., Rignot, E., Fenty, I., Menemenlis, D., Millan, R., Morlighem, M., et al. (2018). Ocean-induced melt triggers glacier retreat in Northwest Greenland. *Geophysical Research Letters*, *45*(16), 8334–8342. https://doi.org/10.1029/2018GL078024

Wood, Michael, Rignot, E., Fenty, I., An, L., Bjørk, A., van den Broeke, M., et al. (2021). Ocean forcing drives glacier retreat in Greenland. *Science Advances*, *7*(1), 1–11. https://doi.org/10.1126/sciadv.aba7282

Wouters, B., Gardner, A. S., & Moholdt, G. (2019). Global glacier mass loss during the GRACE satellite mission (2002-2016). *Frontiers in Earth Science*, *7*(May), 1–11. https://doi.org/10.3389/feart.2019.00096

Zemp, M, Huss, M., Thibert, E., Eckert, N., McNabb, R., Huber, J., et al. (2019). Global glacier mass changes and their contributions to sea-level rise from 1961 to 2016. *Nature*, *568*(7752), 382–386.

Zemp, M., Frey, H., Gärtner-Roer, I., Nussbaumer, S. U., Hoelzle, M., Paul, F., et al. (2015). Historically unprecedented global glacier decline in the early 21st century. *Journal of Glaciology*, *61*(228), 745–762. https://doi.org/10.3189/2015JoG15J017

Zhang, X., He, J., Zhang, J., Polyakov, I., Gerdes, R., Inoue, J., & Wu, P. (2013). Enhanced poleward moisture transport and amplified northern high-latitude wetting trend. *Nature Climate Change*, *3*(1), 47–51. https://doi.org/10.1038/nclimate1631

Zuo, H., Balmaseda, M. A., de Boisseson, E., Hirahara, S., Chrust, M., & De Rosnay, P. (2017).

A generic ensemble generation scheme for data assimilation and ocean analysis. *ECMWF Tech Memo*. https://doi.org/10.21957/cub7mq0i4

Zuo, H., Balmaseda, M. A., Tietsche, S., Mogensen, K., & Mayer, M. (2019). The ECMWF operational ensemble reanalysis–analysis system for ocean and sea ice: a description of the system and assessment. *Ocean Science*, *15*(3), 779–808. https://doi.org/10.5194/os-15-779-2019